NUMERICAL SIMULATION OF OIL SPILLS IN COASTAL AREAS USING SHALLOW WATER EQUATIONS IN GENERALISED COORDINATES

Guillaume Novelli

Dipòsit Legal: T-1797-2011

DOCTORAL THESIS

Guillaume Novelli

NUMERICAL SIMULATION OF OIL SPILLS IN COASTAL AREAS USING SHALLOW WATER EQUATIONS IN GENERALISED COORDINATES

Department of Mechanical Engineering

UNIVERSITAT ROVIRA I VIRGILI

Guillaume Novelli

NUMERICAL SIMULATION OF OIL SPILLS IN COASTAL AREAS USING SHALLOW WATER EQUATIONS IN GENERALISED COORDINATES

DOCTORAL THESIS

Supervised by

Dr. Ildefonso Cuesta and Dr. Francesc Xavier Grau

Department of Mechanical Engineering

UNIVERSITAT ROVIRA I VIRGILI

Tarragona
2011

Departament d'Enginyeria Mecànica
Escola Tècnica Superior d'Enginyeria Química
Universitat Rovira i Virgili
Av. Països Catalans, 26
43007 Tarragona
Tel. 977 55 96 02
Fax 977 55 96 91

Dr F.X. Grau Vidal and Dr. Ildefonso Cuesta Romeo, respectively Professor and Associate Professor in the Mechanical Engineering Department of Universita Rovira i Virgili,

CERTIFY :

That the present study, entitled :

"NUMERICAL SIMULATION OF OIL SPILLS IN COASTAL AREAS USING SHALLOW WATER EQUATIONS IN GENERALISED COORDINATES",

presented by Guillaume Novelli for the award of the degree of Doctor, has been carried out under our supervision at the Department of Mechanical Engineering of this university and that, in our opinion, it is fully adequate in scope and quality as a dissertation for the degree of Doctor of Philosophy.

Tarragona, 15 July 2011

Dr. F.X. Grau Vidal

Dr. Ildefonso Cuesta Romeo

Pour Sibel,
pour mes parents,
et pour mes grand-parents

Contents

Abstract

The pollution generated by accidental marine oil spills can cause persistent ecological disasters and lead to serious social and economical damages. Numerical simulations are a valuable tool to make proper decisions in emergency situation or to plan response actions beforehand. In the early 1990's, members of the University Rovira i Virgili developed in this sense SIMOIL, a computational model capable of predicting the evaporation and spreading of massive oil spills in coastal areas. Among the rest of numerical models available, SIMOIL was characterised by two original features:

- the application of a Eulerian model of the oil slick thickness dynamics, instead of the most commonly used Lagrangian method of tracking separated oil parcels,
- the advection-diffusion problem is discretized over a boundary-fitted coordinates system. This method allows to capture in details the movement and accumulation of oil along arbitrary shaped coastlines. The adaptability of this approach contrasts with the restriction to simpler regions derived from the use of Cartesian coordinates system in other models.

However, the use of SIMOIL was limited to regions where currents were already known or could be determined by the potential flow approximation. The main objective of this work is to solve this issue by implementing a numerical model able to predict coastal currents in generalised coordinates to increase the accuracy and the range of applications of SIMOIL.

Specifically, a new coastal current modelling, based on the resolution of the shallow water equations in generalised coordinates, has been developed and validated to improve both accuracy and applicability of SIMOIL. To establish the model of coastal flow, the primitive ocean equations were integrated vertically over the depth.

Then, the shallow water equations were formulated in function of the variables vorticity and stream function, under the rigid-lid approximation. Consequently, the pressure was eliminated from the equations and the number of equations to be solved was reduced from six to two. Finally, a complete system of equations was obtained and expressed in a generalised system of coordinates. The model was specially designed to describe coastal oceanic flows over topography accounting for Coriolis force, eddy viscosity, seabed friction and to couple with SIMOIL in domain with complex boundaries.

The Thompson numerical method has been used to map physical domains with curvilinear boundaries onto simpler computational domain where the system of partial differential equations can be readily approximated by the method of finite differences. The Akima bi-variate interpolation FORTRAN routine is employed to interpolate over generalised meshes the sparse bathymetry measurements available. The complete space discretization of the system of shallow water equations is second-order accurate using centred finite differences scheme. The discretization of the convection term of the equation governing oil thickness dynamics has been upgraded from first-order upwind to second-order upwind scheme. The diffusion terms are all approximated with centred finite differences scheme. The time integration of the vorticity equation was made using the implicit second-order accurate Crank-Nicolson scheme. The resulting large system of partial differential equations was solved by successive over relaxation. The oil thickness equation is solved using the explicit fourth-order accurate Runge-Kutta method. Moreover, Open MP parallel programming techniques have been applied to speed-up the solvers and to reduce the additional computational cost of induced by the calculations of sea currents. Besides that, investigators recently demonstrated that the evaporation of oil at sea surface is not totally regulated by the oil/air boundary-layer, as most of the current models assumed, among them SIMOIL. As a result, the equations describing the evolution of the physical properties of the oil have been rewritten accordingly.

Special attention was given to the verification of the code. First, well documented flows inside lid-driven cavities of three different geometries have been simulated numerically. Velocity profiles through the cavities were used to compare with numerical and experimental velocity measurements and shown good agreement with the literature. Two more benchmark simulations were performed to check the open boundary conditions: the backward-facing step and the laminar plane wall jet. In both cases the model provided results in excellent agreement with other au-

thors. To complete the validation of the shallow coastal ocean model, the interaction of a vortex with topography is studied at oceanic scale. In this configuration a cyclonic vortex is released in the vicinity of a steep slope. The vortex is forced to move northwestward until it is deviated southwestward by the topographic β-effect created by the slope. As the vortex is moving southwestward, a meandering current heading North is created above the slope. The numerical model allowed to observe and reproduce well these phenomena as described in other experimental and numerical studies.

Lastly, the new complete version of SIMOIL, coupling the shallow water model and the oil slick model, has been applied to the study of two accidental oil spills. The first case is a hypothetical massive leakage from the Repsol floating dock in the vicinity of the port of Tarragona under typical autumn wind conditions. A comparison is made between the previous version of SIMOIL, when currents were calculated from a potential flow approximation, and the version developed in this work, where the currents are calculated according to the shallow water theory. The main result, as expected, is that this new version is more appropriate to simulate coastal oil spills under moderate wind intensities (force 4 or less on Beaufort scale), because an accurate estimation of the coastal currents is necessary to determine the trajectory of the oil slick. The second case treats the major oil spill ever occurred in the Mediterranean: the 2006 Lebanon war oil spill. Nearly 20,000 tons of heavy fuel oil were released into the sea after the bombing of Jiyeh power plant located on the Lebanon coast at 30 km to the south of Beirut. The Mediterranean Operational Oceanography Network was requested to provide operational support to the authorities by monitoring the oil displacements by satellite observations and setting up oil spill simulations. Simulations were also run with the previous potential flow version of SIMOIL. The results demonstrated that the new version, based on the shallow water equations, is capable of producing accurate predictions for more than a few days with such complex coastline. The code developed in this work successfully and accurately reproduced the observed trajectory and landings of the oil slick up to 10 days after the beginning of the spill. The coastal currents and recirculations were predicted with great resolution, allowing the forecasting of oil slicks movements, oil accumulation on beaches and evaporation to coincide with the observational data collected for the pollution assessment and the coordination of response actions.

As a conclusion, the code developped in this work results to be a fundamental improvement of SIMOIL. It has been validated to predict time and space evolution of oil spills. It can be considered a suitable and valuable assessment tool for contingency planning of oil spills in coastal areas.

Resumen

La contaminación generada por derrames accidentales de hidrocarburos en el mar puede causar desastres ecológicos duraderos y daños socio-económicos. Las simulaciones numéricas son una herramienta valiosa para tomar decisiones adecuadas en situaciones de emergencia o para planificar de antemano las operaciones de rescate y protección. En la década de los 90, miembros de la Universidad Rovira i Virgili desarrollaron SIMOIL, un modelo computacional capaz de predecir la evaporación y la difusión de vertidos masivos de petróleo en zonas costeras. Entre todos los modelos numéricos existentes, SIMOIL destaca por dos características:

- el uso de un modelo Euleriano de la dinámica del grosor de la mancha de crudo, en lugar del método Lagrangiano más utilizado que consiste en seguir la trayectoria de grupos de partículas de crudo independientes,
- el problema de advección-difusión se discretiza en un sistema de coordenadas generalizadas. Este método permite capturar detalles en el movimiento y la acumulación de las manchas de petróleo a lo largo de costas cuya forma es arbitraria. La adaptabilidad de este enfoque contrasta con la restricción a regiones de geometrías más simples, cuando se utiliza sistemas de coordenadas cartesianas.

Sin embargo, el uso de SIMOIL se limitaba a regiones donde las corrientes ya se conocían o se podían determinar por aproximación de flujo potencial. El principal objetivo de este trabajo es resolver este problema mediante la implementación de un modelo numérico capaz de prever las corrientes costeras en coordenadas curvilíneas para aumentar la precisión y el rango de aplicaciones de SIMOIL.

En concreto, se ha desarrollado y validado una nueva modelización de las corrientes costeras, basada en la resolución de las ecuaciones de aguas someras en coordenadas curvilíneas, para mejorar la precisión y la aplicabilidad de SIMOIL. Por una parte, para establecer el modelo de flujo en la costa, las ecuaciones pri-

mitivas fueron integradas verticalmente sobre la profundidad. Posteriormente, las ecuaciones de aguas someras se expresaron en función de las variables derivadas vorticidad y función de corriente, bajo la aproximación de pared rígida. Así, la presión fue eliminada de las ecuaciones y el número de ecuaciones a resolver se redujo de seis a dos. Por último, se obtuvo un sistema completo de ecuaciones formuladas en un sistema de coordenadas curvilíneas. El modelo fue diseñado especialmente para describir los flujos oceánicos costeros teniendo particularmente en cuenta la variabilidad de la batimetría, la fuerza de Coriolis, la viscosidad turbulenta o la fricción creada por el fondo marino, así como el acoplamiento con SIMOIL en dominios definidos por fronteras complejas. Por otra parte, las ecuaciones que describen la evaporación de la mancha de crudo en SIMOIL han sido mejoradas. A partir de resultados recientes se implementó un modelo de evaporación, basado en mediciones de propiedades de destilación del crudo, más relevante que el modelo de Mackay usado anteriormente.

Para construir mallas generalizadas que se adaptan a la forma irregular de las costas se usa el método numérico de Thompson. El sistema de ecuaciones diferenciales que gobierna el flujo oceánico costero se discretiza en el dominio computacional así generado mediante el método de diferencias finitas. Las mediciones de la batimetría costera, muchas veces escasas, se interpolan en cada punto de la malla usando la rutina de interpolación bivariada de Akima. De esta forma se consigue una discretización espacial de las ecuaciones de aguas someras de segundo orden en la totalidad del dominio de cálculo. Para la ecuación correspondiente a la evolución espacio-temporal del grosor de la mancha de crudo, también se ha incrementado el orden de la discretización de los términos convectivos usando un esquema upwind de segundo orden en lugar del primer orden previamente implementado. Los términos difusivos siguen aproximados al segundo orden con un esquema de diferencias finitas centradas. Para la integración temporal de la ecuación de vorticidad se utiliza el esquema de Crank-Nicolson, de segundo orden e implícito. El complejo sistema de ecuaciones resultante se resuelve mediante un método iterativo de sobrerelajación sucesiva. La evolución temporal de la mancha se resuelve explícitamente con un método de Runge-Kutta de cuarto orden. Desde el punto de vista de la programación, se ha desarrollado todo el código en lenguaje FORTRAN, usando directivas de cálculo en paralelo Open MP para ordenadores multiprocesador de memoria compartida para acelerar la resolución de los sistemas de ecuaciones. El código resultante ha sido cuidadosamente verificado. Primero simulando casos

bien documentados de flujos en cavidades bidimensionales de tres tipos de geometría. Los perfiles de velocidades obtenidos con el código son los mismos que los resultados numéricos y experimentales que se encuentran en la bibliografía. Así se demostró la correcta implementación del código y de las ecuaciones en coordenadas generalizadas. A continuación, se simularon dos flujos en canales para comprobar la correcta aplicación de condiciones de contorno abiertas: el flujo sobre un escalón descendiente y el chorro laminar a lo largo de una pared. En ambos casos, el modelo desarrollado aquí proporcionó resultados excelentes en concordancia con las demás investigaciones tanto experimentales como numéricas. Para completar la validación del modelo de océano costero, se estudió la influencia de la batimetría sobre la trayectoria de un remolino ciclónico a escala oceánica. En las simulaciones numéricas se pudo reproducir con precisión el efecto topográfico β descrito en la literatura tanto numérica como experimental. En el hemisferio norte, se trata de la desviación hacia el suroeste de la trayectoria del remolino ciclónico, inducida por la combinación de la fuerza de Coriolis y la presencia de una pendiente fuerte en la zona oeste de la cuenca oceánica. Este fenómeno se acompaña de la creación de una corriente que oscila de un lado a otro de la pendiente.

Por último, la nueva versión completa de SIMOIL, integrando el modelo de ecuaciones de aguas someras y el modelo de mancha de crudo, se aplicó al estudio de dos vertidos de crudo en el mar. El primer caso es una hipotética fuga masiva de crudo originada en la monoboya de descarga de Repsol, situada cerca del puerto de Tarragona, con condiciones meteorológicas típicas del otoño en esta región. Se comparan la versión anterior de SIMOIL, con corrientes calculadas a partir de la aproximación de flujo potencial, y la versión desarrollada en este trabajo, cuyo campo dinámico está calculado de acuerdo con la teoría de aguas someras. El resultado principal, como era de esperar, es que esta nueva versión es más apropiada para simular los vertidos de petróleo en la costa cuando la intensidad de los vientos es moderada (fuerza 4, o inferior, en la escala de Beaufort). Esto se debe a que, para determinar con detalle la trayectoria de la mancha de petróleo, es necesario determinar precisamente las corrientes costeras. El segundo caso es el del mayor vertido de fueloil que se haya producido en el mar Mediterráneo hasta la fecha: la marea negra consecuencia de la guerra del Líbano durante el verano del 2006. El vertido se produjo cuando unas 20000 toneladas de fueloil pesado se vertieron en el mar después del bombardeo de la central térmica de Jiyeh, situada en la costa de Líbano 30 kilómetros al sur de Beirut. La red mediterránea de oceano-

grafía operacional (MOON) fue encargada de proporcionar apoyo operacional a la autoridades siguiendo el desplazamiento de la mancha mediante observaciones por satélite y simulaciones numéricas de transporte de crudo en el mar con el código MEDSLIK-CYCOFOS. Ambas simulaciones y observaciones se compararon con simulaciones ejecutadas con la anterior versión de SIMOIL y con la nueva versión del programa. Los resultados demuestran que la nueva versión es capaz de producir predicciones precisas a más de 3 días en una costa tan compleja. El código desarrollado en este trabajo logró reproducir la trayectoria observada de la mancha de petróleo así como su acumulación en la costa hasta 10 días después del bombardeo. Las corrientes costeras y las zonas de recirculación asociadas fueron descritas con la máxima resolución, permitiendo que la predicción de la trayectoria, del aterrizaje y de la evaporación del fueloil coincidiera con las observaciones recolectadas durante los hechos.

A modo de conclusión, el código desarrollado en este trabajo resulta ser una mejora fundamental de SIMOIL. Se ha validado para predecir la evolución temporal y espacial de los vertidos masivos de petróleo en el mar. Se puede considerar como una herramienta valiosa y adecuada para el asesoramiento y la planificación de acciones correctivas en caso de vertidos de petróleo cercanos al litoral.

Acknowledgements

This work has been carried out at ECOMMFIT group in the Mechanical Engineering Department of University Rovira i Virgili of Tarragona under the supervision of Prof. Francesc Xavier Grau and Dr. Ildefonso Cuesta.

It is my pleasure to acknowledge my supervisors Prof. Francesc Xavier Grau and Dr. Ildefonso Cuesta for giving me the opportunity to work on this topic as well as for their guidance and comments.

None of this work would have been possible without the valuable contributions of Dr. Àlexandre Fabregat all along this project. I am also very grateful to Dr. Gabriel Usera for the meaningful discussions we had about fluid mechanics and for sharing his knowledge about the art of parallel programming and compiling. Helpful discussions and comments on a draft of this report by Dr. Francisco Táboas are gratefully acknowledged.

I am also very grateful to ITOPF information officer Deborah Ansell, the UNEP publication service, Dr. Zavala-Sansón, Dr. Coppini and Dr. Cuesta for gracefully giving me the permission to use and publish their data and pictures in this dissertation.

I had the chance to assist some professors in teaching graduate and undergraduate students at ETSEQ. I would like to warmly thank Robert Gilabert, Manuel Granado, Clara Salueña, Youssef Stiriba, and Anton Vernet for their kindness, availability and the support they provided me with to carry on this task in parallel with the research activity.

I have to thank also the administrative staff at the Mechanical and Chemical Engineering Departments. I specially appreciate the help I received from Núria Juanpere Mitjana and Samuel Garcia Mega.

I enjoyed all these years being a member of ECOMMFIT group. I would like to thank specially the rest of PhD students with who we shared something more than an office space and an odd taste for differential equations: Àlex, Elkin, Gabriel,

Manuel, Pedro (;-), Obai, Roland, Salvatore, Silvana (T) and Sylvana (V).

Above all, I am deeply grateful to my parents, Anne-Marie and Philippe, who always feed me with their love and trust, not to speak about economical support. I would like to express my deepest gratitude to Sibel Özgen for accompanying me throughout this journey, in the good days and the not so good ones. You inspire and motivate me everyday.

Finally, I would like to acknowledge the members of the jury Prof. Josep Anton Ferré, Dr. Jordi Pallarès, Dr. Àngel Jiménez, Dra. Immaculada Iglesias and Dr. Josep Ramon González, and everyone who contributed to this work directly or indirectly.

List of Tables

List of Figures

Nomenclature

Roman Symbols

a ..... Earth equatorial radius($a = 6,378,137m$)
a^+, a^-, b^+, b^- ..... Coefficients for the upwind scheme
A_o ..... Area of oil on the sea surface (m^2)
A_H ..... Horizontal eddy viscosity(m^2/s)
A_V ..... Vertical eddy viscosity(m^2/s)
$\vec{b}$ ..... Buoyancy force (kgm/s^{-2})
c ..... Concentration of pollutant (mol/m^3)
c_s ..... Sound velocity in the ocean($c_s = 1,500m/s$)
C ..... Oil thickness diffusion-like coefficient (s^{-1})
C_D^{bottom} ..... Seabed friction coefficient
C_D^{wind} ..... Wind drag coefficient
$\mathcal{C}$ ..... Friction function
D ..... Diffusive term
D_U ..... Viscous dissipation of momentum term
D_T ..... Thermal diffusion term
D_S ..... Salinity diffusion term
e ..... Earth WGS84 ellipsoid eccentricity ($e = 0.08181919084$)
E ..... Evaporative exposure (m^3/kg)
f ..... Coriolis parameter (s^{-1})
F ..... Fraction of evaporated oil
$\mathcal{F}$ ..... Spatial discretization operator
g ..... Gravity acceleration (m/s^2)
g_{ij} ..... Metric tensor relating generalised to Cartesian system of coordinates
h ..... Oil slick thickness (m)
H ..... Depth (m)
J ..... Jacobian of the transformation from Cartesian to generalised coordinates

k ..... Momentum transfer coefficient between oil and sea water (kg/m^2s)
K ..... Mass transfer coefficient between oil and atmosphere (m/s)
L ..... Length of reference (m)
M ..... Meridional radius of curvature (m)
$\vec{n}$ ..... Vector normal to a surface
N ..... Normal radius of Curvature (m)
P ..... Pressure (Pa)
r ..... Radial distance (m)
R ..... Radius of reference(m)
$Re = \frac{UL}{\nu}$ ..... Reynolds number
$Ro = \frac{U}{fL}$ ..... Rossby number
$\mathcal{R}$ ..... Residual function
S ..... Salinity (mol/m^3)
t ..... Time (s)
$\vec{t}$ ..... Vector tangent to a surface
T ..... Temperature (K)
$\vec{U}$ ..... Velocity vector in Cartesian coordinates (m/s)
U_{avg} ..... Average velocity (m/s)
U_{max} ..... Maximum velocity (m/s)
$\vec{v}$ ..... Horizontal velocity vector (m/s)
$\vec{U_h}$ ..... Depth integrated velocity vector (m/s)
(O,x,y,z) ..... Cartesian system of coordinates (m)

Greek Symbols

α, β, γ ..... Geometric coefficients of the metric tensor
β_S ..... Haline contraction of sea water ($\beta_S = 10^{-3} psu^{-1}$)
β_T ..... Thermal expansion of sea water ($\beta_T = 2 \times 10^{-4} K^{-1}$)
δ ..... Boundary layer thickness (m)
Δ ..... Increment
(O,ε,η,z) ..... Generalised system of coordinates
θ ..... Angle ($radian$)
$\vec{\nabla}()$ ..... Vector operator gradient of a scalar
$\vec{\nabla} \cdot \vec{()}$ ..... Divergence of a vector field
$\vec{\nabla} \times \vec{()}$ ..... Curl of a vector field
κ_Φ ..... Eddy diffusivity of tracer Φ

λ ..... Longitude (^oE)
μ ..... Similarity variable ($\mu = \frac{y}{\delta}$)
ν ..... Kinematic viscosity (m^2/s)
ρ ..... Density (kg/m^3)
Σ ..... Sum
τ ..... Stress (Pa)
φ ..... Latitude (^oN)
Φ ..... Scalar
ψ ..... Stream function (m^3/s)
ω ..... Vorticity ($/s$)
Ω ..... Earth rotation rate ($\Omega = 7.3 \times 10^{-5} s^{-1}$)

Subscripts/Superscripts

$()_0$ ..... Refered to quantity of reference
$()_a$ ..... Refered to air
$()_o$ ..... Refered to oil
$()_w$ ..... Refered to sea water
$()_\psi$ ..... Refered to stream function
$()_\omega$ ..... Refered to vorticity
$()_h$ ..... Refered to depth averaged quantity
$()_{ij}$ ..... Refered to covariant ij component
$()^{ij}$ ..... Refered to contravariant ij component
$()^{(k)}$ ..... Refered to previous iteration
$()^{(k+1)}$ ..... Refered to current iteration
$()_n$ ..... Normal direction
$()^n$ ..... Refered to previous time step
$()^{n+1}$ ..... Refered to current time step
$()^*$ ..... Intermediate quantity

Chapter 1

Introduction

1.1 Motivation

Major oil spills caused by oil tanker accidents attract periodically the attention of media, spreading abroad pictures of oil-coated birds and damaged landscapes. So today, the public, policy makers, oil companies and tanker owners, expect the best achievable response to oil spills: it has to be scientifically based and the result of a process of contingency planning and extensive training at all levels.
As pointed out in the preface of the last report of the U.S. National Academies on the subject of oil spills [1], planning and decision making in oil spill response requires a good understanding of:

- the physical and chemical evolution of the properties of oil,
- the local environmental conditions,
- the ecological sensitivity of the coastal area,
- the effectiveness of response methods and technologies.

Since 40 years, numerical simulations of the transport of the pollution caused by hazardous material in the sea are available. Dynamic oil weathering and oil trajectory models have been developed to predict oil behaviour over time and are being used as a decision-making tool in actual and fictitious spills. In the 1990', members of the ECOMMFIT[1] group, developed a numerical model of oil spills, SIMOIL[2], which was successfully validated for impact assessment and contingency planning.

[1] *Experimentació, Computació i Modelització en Mecànica de Fluids i Turbulència*, Mechanical Engineering Department, Universitat Rovira i Virgili, http://ecommfit.urv.es
[2] http://ecommfit.urv.es/SIMOIL

In the last decade, the improvements in computer power and storage have made possible the integration of many data sources in the simulations, such as weather, wind, current and water temperature, chemical and physical properties of the oil. The development of instrumentation, in fields like bathymetric survey and velocity measurement, yield data that are critical for setting up and test the model. The availability of parallel processing make possible to run linked complex flows with bathymetry and weathering models at a high resolution. Finally, the development of an accurate coastal hydrodynamic model for SIMOIL is the main motivation for the present work.

1.2 Background

1.2.1 Sources of oil in the sea

The expression *"marine oil spills"* refers to accidental releases of oil into the sea. According to the trends in energy usage, oil production and consumption are not likely to decrease much in the future. The threat of oil pollution is increasing accordingly, especially when one considers that nowadays 30% of the crude oil produced worldwide comes from offshore exploitation.
OCEANA, an international organization for the protection of the oceans, reported that in 2003 the global transportation of crude oil moved 1,600-1,800 million tons a year mainly to the European Union and the United States and more than 1,000 million tons of oil was transiting European waters each year [2]. Since 1974, the ITOPF[3] has maintained a database of oil spills from ships, covering all accidental spillage except those resulting from acts of war. According to this database [3] and in average over the last 30 years, around 300 oil tanker accidents occur every year, causing between 240,000 and 960,000 tons of hydrocarbons to be dumped into the oceans.
The 20 major oil spills from ship tankers are listed in table 1.1. The Exxon Valdez, although being the 35^{th}, is included because of its impact on media, and thus, its influence on the maritime industry policy makers.

As can be seen in figure 1.1, the overall amount of petroleum released to the ma-

[3] *International Tanker Owners Pollution Federation* is a not-for-profit organisation of tanker shipowners and pollution insurers, which is providing technical services related to ship-source spill of hazardous material in the marine environment

Position	Ship Name	Year	Location	Spill Size (tons)
1	Atlantic Empress	1979	Off Tobago West Indies	287,000
2	ABT Summer	1991	700 nautical miles off Angola	260,000
3	Castillo de Bellver	1983	Off Saldanha Bay, South Africa	252,000
4	Amoco Cadiz	1978	Off Brittany, France	223,000
5	Haven	1991	Genoa, Italy	144,000
6	Odyssey	1988	700 nautical miles off Nova Scotia, Canada	132,000
7	Torrey Canyon	1967	Scilly Isles, UK	119,000
8	Sea Star	1972	Gulf of Oman	115,000
9	Irenes Serenade	1980	Navarino Bay, Greece	100,000
10	Urquiola	1976	La Coruña, Spain	100,000
11	Hawaiian Patriot	1977	300 nautical miles off Honolulu	95,000
12	Independenta	1979	Bosphorus, Turkey	95,000
13	Jakob Maersk	1975	Oporto, Portugal	88,000
14	Braer	1993	Shetland Islands, UK	85,000
15	Khark 5	1989	120 nautical miles off Atlantic coast of Morocco	80,000
16	Aegean Sea	1992	La Coruña, Spain	74,000
17	Sea Empress	1996	Milford Haven, UK	72,000
18	Katina P.	1992	Off Maputo, Mozambique	72,000
19	Nova	1985	Off Kharg Island, Gulf of Iran	70,000
20	Prestige	2002	Off the Spanish coast	63,000
35	Exxon Valdez	1989	Prince William Sound, Alaska, USA	37,000

Table 1.1: Major oil spills from ships since 1967, Courtesy of ITOPF [3]

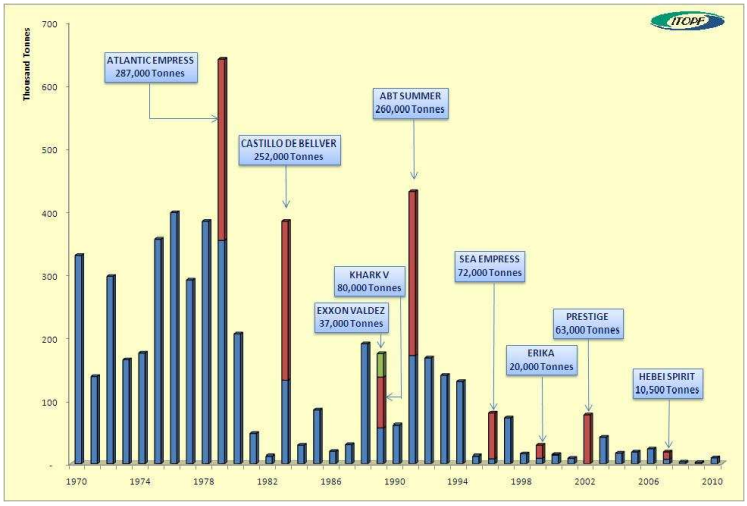

Figure 1.1: Quantities of oil spilled in the sea between 1970 and 2010. Courtesy of ITOPF [3]

rine environment is decreasing with years. This reflects technological advances in marine transportation (double-hulls tankers) and oil and gas production techniques, as well as the implementation of more rigorous regulations for safer transportation procedures. However, releases from extraction (see figure 1.2) and transportation of petroleum represent less than 10 percent of inputs from human activity. As noticed in [1], chronic releases during consumption of petroleum, which include urban runoff, polluted rivers, and discharges from commercial and recreational marine vessels, contribute up to 85 percent of the human load to North American waters. These releases can pose significant risks to the sensitive coastal environment where they most often occur.

1.2.2 Weathering and transport of marine oil spill

Once spilt at sea, oil fate and behaviour are governed by complex, interrelated physicochemical processes generally known as *"weathering process"*. The weathering depends on oil properties, hydrodynamic conditions and environmental conditions. Advection, spreading, evaporation, oxidation, dissolution, dispersion, emulsification, bio-degradation and sedimentation are terms describing the possible evolution of the weathering of an oil spill. Figures 1.3 [4] and 1.4 [5] are schematic representations of the fate of a crude oil spill showing changes in the relative im-

Figure 1.2: Satellite view of a massive oil spill spreading towards Mississippi Delta on April 25^{th} 2010, after an explosion occurred on April 20^{th} 2010, on Deepwater Horizon rig. Image credits : NASA/GSFC, MODIS Rapid Response

portance of weathering processes with time.

The modelling of the oil weathering and the eventual response actions is essential to understand the toxicity and the trajectory of a spill. Many studies addressing this issue have been summed up in recent scientific reviews about environmental pollution [5, 6, 7, 8].

Spreading: It is the result of an increase of the area of the oil slick. Spreading is governed by the balance between gravity and viscous forces. While gravity tends to extend the surface of oil slick and reduce the thickness of the film, friction between water and oil tends to limit the spreading of the slick. Evaporation and emulsification, by increasing oil viscosity, increase friction with time. Fay-type spreading models, based on the gravity-viscosity balance, are used by many algorithms to predict the thickness and the area of the slicks, even if it is widely recognized that spreading is not fully represented by Fay equation [7]. Another transport-and-spreading model, describing much better the slick thickness dynamics, was developed by Benque et al. [9]. This model remained unnoticed in the oil modelling community because of the high computational cost it represented at that time [10]. Later, this model has been adapted to curvilinear coordinates in SIMOIL [11].

Advection: The net transport rate and direction of a spill is the sum of the influ-

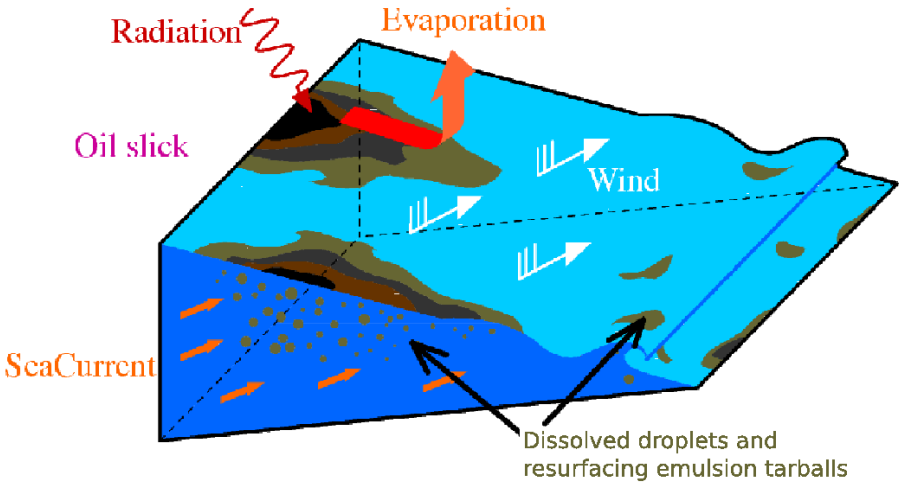

Figure 1.3: Weathering of oil slicks

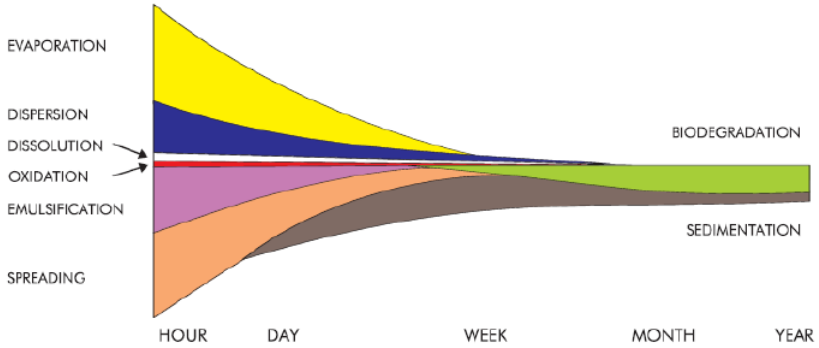

Figure 1.4: The relative importance of weathering processes with time. Courtesy of ITOPF [3]

ences of winds, waves, surface currents and oceanic turbulent diffusion. As most of the oil usually remains in the sea surface, oil moves mainly horizontally forced by wind and sea-current contributions. Advective currents can be computed from current atlases (static approximations), live meteorologic observations, buoys trajectory or hydrodynamic modelling (dynamic approximations).

Evaporation: An oil is composed of many different substances. Oils behaviors at sea are usually classified in 4 groups going from "non-persistent" (in purple in figure 1.5) to "very persistent" oil (in red in figure 1.5), in function of the physical properties of their compounds (waxes, small saturates, aromatics, resins, asphaltenes) such as specific gravity (oil density relative to pure water, often measured in $^{\circ}$API), distillation characteristics, viscosity and pour point. Small saturates and aromatics are the most dispersible components of oils. They are fairly soluble in water, but also evaporate rapidly. The other compounds do not evaporate or disperse easily and use to stabilise in water-in-oil emulsions under certain conditions [12, 13]. Figure 1.5 shows the different behaviour of those groups. Mackay developed in 1980 a simple model of the evaporation based on the elapsed time, the slick area, the wind speed, the vapor pressure and the temperature. This model is still widely used [11] despite its simplicity and the over-estimate of evaporation in the first hours and under-estimation later on [14].

Emulsification: It is the process of mixing water droplets into oil, forming a water-in-oil emulsion. The oil can take up until 80% of water, changing drastically the density of the mixture which volume can expand up to five times the original volume. It increases also dramatically the viscosity [13,15]. Reliable prediction of emulsification and the associated viscosity changes presently relies on empirical observations, since established prediction methods have proved unreliable [7].

Entrainment: Oil can be transported vertically in the water column in the form of oil droplets. It depends primarily on the wind conditions and the water depth as wave breaking especially enhances the process. Another source of vertical entrainment can be Langmuir circulation. It appears when the wind blows strongly ($>$ 3 to 9 m.s^{-1}) over the sea, creating polluted windrows: long oily

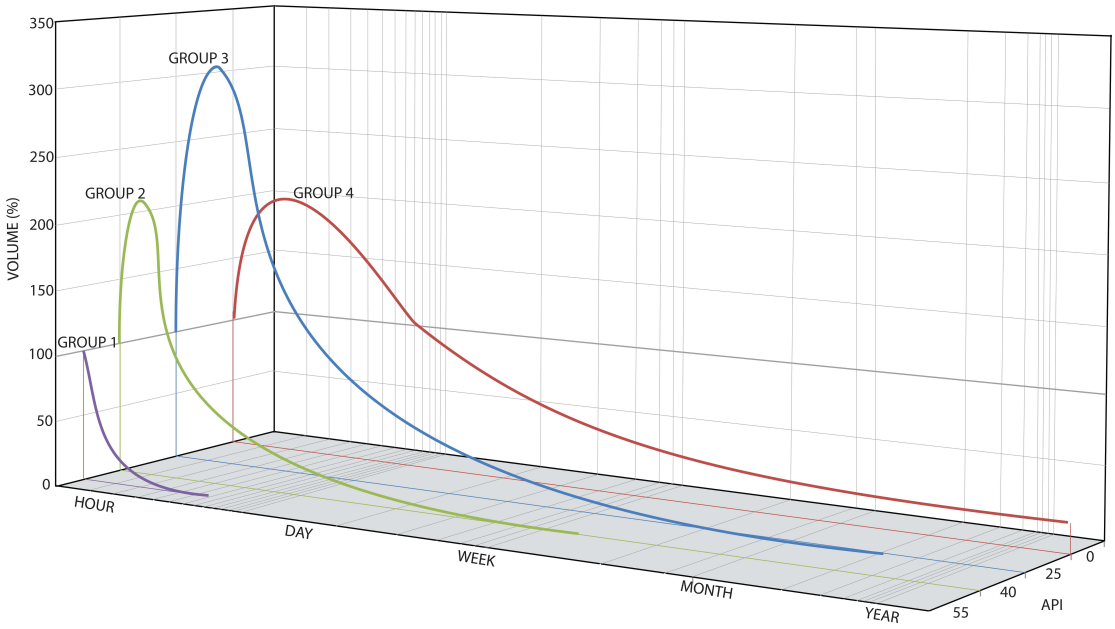

Figure 1.5: Volume of oil remaining on the sea surface in function of oil composition. Courtesy of ITOPF [3]

streaks, parallel to the wind direction, where the oil accumulate. In between those streaks, the oil is entrained deep under the sea-surface. The largest droplets will resurface while smaller ones may remain in the water column to be advected, dissolved or absorbed by biota or to sediment. Entrainment process is not represented in the majority of the models which neglect the vertical movements of oil [5]. A notable exception is the MOSM[4] [16, 10]. Using a model of the balance between breaking wave energy and oil droplets buoyancy, thus the time evolution of the concentration of oil droplets in the water column can be computed.

Dissolution: It depends largely on oil composition and interfacial area. Entrainment of droplets enhance dissolution by increasing interfacial area between the water and the oil droplets. It is a process relatively unimportant in determining mass balance but very important in terms of potential biological impacts.

Sedimentation: Oil-sediment interaction is not well documented. It depends on

[4] *Multiphase Oil Spill Model*

the substract rugosity and its capacity of absorption, as well as on oil viscosity or tide level.

Response Action: Four major response strategies are available to fight against oil spills: chemical treatment, in-situ burning, mechanical recovery, and bio-remediation. Dispersants and emulsion-breakers are used to break the emulsification process and enhance the dispersion rate. Blooms, like in the picture of figure 1.6, are used to confine the spill to be skimmed or adsorbed and then mechanically recovered, or even directly burned at sea [17]. Nutriments (nitrates, phosphates) can be added to the dispersants, to enhance the reproduction of specific bacteria able to metabolise the lighter compounds of petroleum. This is called bio-remediation. The OSCAR[5] model has a module devoted to oil recovery and chemical dispersant application actions, relating environmental factors (such as winds and waves or available daylight) to effectiveness of mechanical cleanup [5, 7].

The complexity of the processes involved in the oil spill problems is very clear. The prediction of the consequences (biological and socio-economic impacts) is a further step beyond the models discussed here.

1.2.3 Consequences of oil spills

As soon as the oil is released into the sea, evaporation in the atmosphere and dispersion in the water column start. The ecological and socio-economic impacts depend on the oil toxicity, time exposure, eco-sensitivity of the region and the response capacity of responsible parties.

Oil-coated seabirds, fishes, marine mammals or even shellfish are known to be affected, but the effects on plankton, at the first trophic level on the oceans food chain, are not totally understood and quantified. Some habitats, such as exposed rocky shorelines, recover quickly from oiling events. Other ecosystems, such as mangroves, salt marshes, sea grasses and coral reefs, and polar habitats, are particularly vulnerable and sensitive to oil spills, and may take years to recover [17].

[5] *Oil Spill Contingency And Response*

Figure 1.6: Oil spill confinement with blooms in Tarragona harbour.
Image credits: 2009-Ildefonso Cuesta

According to "*Oil in the Sea*" report [1], the biological effects of oil spills are usually acute. It means that the spills have short-term effects (from days to years) but with high concentration of petroleum covering up to thousands of square kilometres.

From an economic point of view, a variety of human activities can be affected by the pollution such as fisheries and tourist resorts. These sectors usually suffer from income losses and property damages, and also need time to recover.
In addition, combat strategies also have a cost, economically and ecologically. Chemical dispersants, used to increase the dispersion rate of oil slicks, are highly toxic in shallow water environments and their use is forbidden near the coast [18]. The cost of the removal of oil can vary in a range from 20 to 200 US Dollars per litre [12].

The financial appreciation of the consequences is of great interest as the response has to balance the cost of the possible damages. A recent study of costs as a function of spill size [19] reveals that :

- for very small spill ($\ll 7$ tons) under extreme weather conditions, the option of "leaving for natural cleaning" should be recommended.
- for a range from medium (> 7 tons) to large (> 700 tons) spills up to 2200 tons, the total oil spill costs could be in a range from €1.3 million to €41.3 million.

1.2.4 Challenges for the best response

All the above statements confirmed that oil spills can have a severe impact. The effects of an accidental release depend on many factors such as the oil quantity, its weathering and trajectory, the vulnerability of ecosystems, and the ability to implement the best response actions. When an oil spill occurs the primary concern is the speed and direction of the oil drift relative to the location of sensitive areas. The weathering of the oil is also important because it affects the behaviour of the oil as well as the eventual environmental consequences of the spill.

The success in taking the best response decisions is determined by a series of actions:

1. being able to predict the spreading and trajectory of the spill with time. This requires forecasting and integrating the direction and speed of wind and current in the area of interest;

2. being able to collect in situ information about oil weathering, or to predict changes in oil properties that will affect the cleanup response;
3. being able to assess the threat posed to marine ecosystems and coastal human activities, in areas known to be at risk from spills or chronic releases of petroleum.

1.3 State of the art on oil spill modelling

Numerical modelling can provide support for rapid and informed decision-making. By generating safe and accurate spill scenarios, it is the ideal tool for contingency planning, response training and damages assessment.

1.3.1 Overview of oil spill models

Many numerical models now exist which simulate the movement or the weathering of oil in the sea. The very first simplest models assumed oil remains at the surface as an ellipse shaped slick simply advected by local winds. More sophisticated models now reproduce additionally vertical dispersion of droplets and some of the weathering processes and response actions, through parameters chosen to fit empirical data when/where they exist.
Usually, the transport of contaminants without sources in a fluid flow is described by an *advection-diffusion* equation like equation (1.1), where c is the concentration of the pollutant.

$$\frac{\partial c}{\partial t} + \vec{\nabla} \cdot (c\vec{U}) - \vec{\nabla}(\vec{D} \cdot \vec{\nabla} c) = 0 \tag{1.1}$$

Advection ($\vec{\nabla} \cdot (c\vec{U})$) of the pollutant is produced by the movement resulting from current and wind forcing, while *diffusion* ($\vec{D}$) is caused mainly by the turbulent fluctuations of the fluid flow and molecular diffusion. The diffusion of pollutants uses to be parameterized as a combination of horizontal (longitudinal and transversal) and vertical components, proportional to the shear velocity and the water depth. Despite the fact that most water quality models utilise a Eulerian approach for solution of the *advection-diffusion* equation [20], because of the need to couple transport and chemical kinetic equations to Eulerian hydrodynamic models, oil spill transport models have been an exception to this practice adopting Lagrangian methods. Use

of a Lagrangian approach is easily justifiable for oil droplet separate tracking in the water column : the spill may be represented by a number of droplets. The diffusion can be calculated by horizontal and vertical diffusivity in the water column, modified by the buoyancy of the oil droplets, using a random walk technique, appropriate for Lagrangian Particle Tracking. This is the method employed for example by the trajectory models GNOME, MOTHY, and OSCAR, briefly described in table 1.2.

However, unbroken slicks on the sea surface can be more accurately considered within two continuous layered media, oil and water, both governed by Eulerian Navier-Stokes equations. In [9], Benque et al. show a way to obtain a single non-linear transport-and-spreading equation that predicts the temporal and spatial dynamics of the slick thickness. Recently, this model has been modified and adapted within SIMOIL [11] and MOSM [10].

1.3.2 SIMOIL

SIMOIL is a computational code developed by members of the ECOMMFIT group to simulate the temporal and spatial evolution of large marine oil spills spreading under gravity-viscosity regime. The model has been applied to assess the effects of fictitious accidents along the Costa Daurada of Tarragona and also to assess the environmental impact of several offshore facilities along the Spanish coast.

The differential model of Benque et al. [9] has been modified to improve boundary conditions modelling, especially for accumulation on the shoreline. Only the slick movement is considered. The only changes allowed in the vertical direction being the slick thickness. An important feature is that the code has been developed in generalised coordinates in order to deal with the naturally complex geometry of the coasts. The governing equation for the evolution of the oil thickness h can be obtained by combining the continuity and the momentum conservation equation, which leads to the single equation :

$$\frac{\partial h}{\partial t} + \vec{\nabla} \cdot (h\vec{U}) - C\nabla^2 h^3 = 0 \tag{1.2}$$

The combined actions of currents, tides and winds in the horizontal plane are included in the advection term $\vec{\nabla} \cdot (h\vec{U})$. C is a diffusion-like coefficient (s^{-1}) depending on oil and water densities (respectively ρ_o and ρ_w in kg m^{-3}) and on k, a

Model	**Developer**	**Specification of oil**	**Has been used for**	**Input**	**Hydrodynamic**	**Weathering processes included**	**Output**
GNOME	NOAA	Various types of oil	Oil spill trajectory	Wind, location, spill amount	2D	Weathering factors associated to each type of oil	Trajectory
MOTHY	Cedre and Météo-France	Boiling point cut for evaporation	Oil spill trajectory analysis	2D currents, winds, waves	Météo-France nowcast-forecast data	Evaporation	Trajectory
OSCAR	SINTEF	200 separate components and more than 300 crude oils and petroleum products	Contingency planning, environmental risk analysis, natural resource damage assessment, oil spill training and response, nowcast-forecast operations	oil type, release type, winds, temperatures, coastlines, bathymetry, currents, ecological habitats, shoreline types, sediments types	2D or 3D currents from hydrodynamic models or measurements. Single point or 2D wind data from models or measurements	spreading, advection, entrainment, dissolution, resurfacing, emulsification, evaporation, beaching, oil recovery, dispersants application	Trajectory, relative success of alternate response strategies, linkage to biological and risk analysis models

Table 1.2: Overview of some operational oil spill models

momentum transfer coefficient between both phases (in kg m^{-2} s^{-1}). Then C reads:

$$C = \frac{1}{3}\frac{\rho_o(\rho_o - \rho_w)g}{k\rho_w} \tag{1.3}$$

Evaporation is modelled following Mackay concept of evaporative exposure E (m^3 kg^{-1}). It links ΔF, the fraction of oil evaporated, to the vapor pressure of oil P_0 (atm), the area of oil on the sea surface A_o (m^2), the oil temperature T (°K), and K (m s^{-1}), a mass transfer coefficient between oil and the atmosphere increasing with the wind velocity W (m s^{-1}). Accordingly, it reads:

$$\Delta F = -\Delta E P_0 e^{-12F} \tag{1.4}$$

where

$$\Delta E = KA_o(1-F)\frac{V_m \Delta t}{V_s RT} \tag{1.5}$$

with V_m being the molar volume of oil (in m^3 mol^{-1}) and V_s the instantaneous total volume of the spill (in m^3), t is the time (in seconds), R is the gas constant (in atm m^3 mol^{-1} K^{-1}) and K is defined by :

$$K = 0.0015W^{0.78} \tag{1.6}$$

Therefore, SIMOIL allows the prediction of the trajectory of the slick along shorelines with complex geometry. It is also capable of estimating the percentage of the volume of the spill evaporated, beached and remaining on the sea surface.

1.3.3 Areas of improvement

Highly effective spill response requires oil models to improve on many aspects. Models introduce major simplifications and neglect (with the exception of evaporation) some important processes, such as emulsification, interaction with shorelines and sediments, or biological effects. Often, physical and chemical processes happen at a scale ranging from 10 to 10,000 meters. That is usually at the sub-grid scale for hydrodynamic models, so the number of required parameters increases. These parameters, such as the vertical mixing coefficient, are poorly understood and are

selected, after laboratory observations or field data acquisition, in order to fit known distributions of released tracer. Therefore, models have to be tuned.
The lack of knowledge about oil composition and the lack of high-resolution hydrodynamic data from diverse sources (or the incapacity to integrate them) are probably limitations to the use of these models in real-time prediction of a spill, especially if no in-situ observations are available.
Models are best at extrapolating spill trajectory from one set of sparse observations. They are also useful in examining a possible range of spill scenarios arising from different combinations of the parameters, helping in the preparation to decision making and training to response actions in the field.

1.4 Objectives and Outline

1.4.1 Objectives

In order to improve SIMOIL predictions in terms of accuracy, reliability and flexibility, the present research project was conducted with the following list of objectives:

- To integrate a new hydrodynamic model designed for coastal flows at regional scale in generalised coordinates
- To add interpolation routines to integrate sparse data into the simulation
- To improve the accuracy and speed-up of the simulations through OpenMP parallelization of the code on multi-processors computers

1.4.2 Outline

For the sake of clarity the presentation of the research work is split into two parts.

Part One focuses on the development of a model of coastal oceanic circulation. Chapter 2 is an introduction to ocean dynamics. The main issues for its modelling are discussed, including the hypothesis assumed for the description of Coriolis forces, dissipation and turbulence and shallow water flows at regional scale.

Then, special attention is paid to the concept of generalised coordinates to tackle the problems of typical coast with a complex geometry. Finally, the vorticity and stream function governing equations for coastal flows are derivated from the primitive form of the Navier-Stokes equations.
Chapter 3 is devoted to the numerical methods for solving the algebraic systems of equations resulting from discretization. The finite difference methods are employed to approximate space and time derivatives. The treatments of non-linear terms, boundaries and complex geometries are described. Interpolation techniques are introduced later to obtain parameters values at every location. Briefly, some iterative solution techniques are considered as well as the OpenMP parallelisation procedure.

Part Two is dedicated to the results of numerical simulations.
In Chapter 4, the importance of the verification process of the code is pointed out. The results of several benchmarks cases are shown. To demonstrate the good implementation of the solvers in FORTRAN 90, results of flow simulations are compared with the literature in order to eliminate errors in programming or limitations of the numerical methods. The shallow water model in generalised coordinates is validated against experimental and numerical results of well documented cases of engineering and oceanic flows.
The final stage of the thesis is achieved in Chapter 5 by the study of the coupling of the hydrodynamic model to the upgraded version of the oil spreading and drifting model SIMOIL. The complete forecasting system is then applied to two oil spill accidents: the first one off the coast of Tarragona and the second one along the coast of Lebanon. These numerical simulations are carried out with two objectives: firstly to confirm the validity of the forecasting system developed in this work by comparing to data collected during the accidents, and secondly to show the improvement over the previous version of SIMOIL.
In Chapter 6 the general conclusions of the thesis are drawn. Possible future developments are also adressed at the end of that chapter.

Part I

NUMERICAL MODEL OF COASTAL CIRCULATION

Chapter 2

Modelling of Coastal Ocean Circulation

The subject of this chapter is to set up a hydrodynamic model for flows in coastal areas that will provide sea currents predictions to the oil spill model SIMOIL.
Ocean motions span a wide range of spatial and temporal scales under the influence of body forces, surface stresses and turbulent dissipation. Those general mechanisms of ocean motions are introduced in section 2.1.
The modelling of all the oceanic phenomena is beyond the scope of this work, however it takes only into account the flow features relevant on a regional scale. Section 2.2 details the assumptions associated to the rigid-lid shallow water model and accordingly, leads to the derivation of the governing equations for coastal circulation. Section 2.3 is an introduction to curvilinear coordinates theory. It is an important and original feature of the SIMOIL engine that is extended here to the hydrodynamic model. Then the final expression of the equations of motion is derived for any system of generalised coordinates.

2.1 Main features of ocean dynamics

2.1.1 Space and time scales

Stewart, in [21], recalls important concepts necessary to understand the fundamentals of oceans dynamics, specially the scales and the physics of oceanic flows. Oceans and seas cover 70.8% of the surface of the earth. Oceanic dimensions range

from 1500 km for the minimum width of the Atlantic to more than 13,000 km for the north-south extent of the Atlantic and the width of the Pacific. The mean depth is around 3800 m. The ratio between vertical and horizontal dimensions, or aspect ratio, is small of the order of 10^{-3}. It also means, from mass conservation, that the ratio of typical vertical to horizontal velocity must be of the same order (or less due to the stable density stratification of the ocean's interior). This characteristic will be used later to simplify the equations of motion.
Hence, oceans can be considered as a shallow layer of fluid on the earth surface. Actually several layers are often distinguished in function of their density profile and dynamic specificity, as mentionned by Thorpe in [22]. On the top lies the *mixed layer*, stirred by the surface winds, with a depth on the order of 10 m where vertical pressure gradients are considered equal to zero. Below lies the *seasonal thermocline* where dynamics and mixing are dominated by seasonal temperature convection due to the changes of the overlying atmosphere. Its depth is on the order of 100 m. Below the seasonal thermocline, the mean temperature decreases linearly through the *main thermocline*, also called *pycnocline*, at depth 500–1000 m. This layer is permanently stratified. At greater depth, above the abyssal plains, lies the *abyssal layer*, where mean density continues to increase slowly as temperature decreases. On the bottom lies another mixed layer due to the turbulence generated at sea bed, with almost homogeneous density over the 5–60 m above the sea floor.

Density stratification and sea bed topography strongly separate the flows.

- At one extreme, the *conveyor belt*, the circulation in the oceanic interior driven by thermohaline convection, is slow and steady in the meridional plane evolving over climatic time scales: deep ocean current speed is typically of 1 m/day and water may remain in the abyss 1000 years before returning to the surface.
- Boundary currents are currents flowing parallel to coasts such as the Gulf Stream on the western edge of the Atlantic ocean on figure 2.1(a). Eastern boundary currents are weak while the western ones tend to be fast narrow jets with a periodicity of several months.
- At the other extreme of the time scale range, on the continental shelves, currents are dominated by tides and forced by winds, atmospheric heating and influenced by sea-bed topography, dissipating a lot of energy in the upper boundary layer at a period varying between hours and weeks. Such flows, for

Process	Length Scale	Time Scale	Rossby Number
Dissipative scales	1–2 mm	~ 1 s	$\sim 10^4$
Vertical mixing	1–100 m	minutes	$\sim 10^2$
Surface waves	1–100 m	seconds	$\sim 10 - 10^2$
Internal waves	1–10 km	mins–hrs	$\sim 10^{-1} - 1$
Mesoscale eddies	10–400 km	weeks–months	$\sim 10^{-1}$
Boundary currents	50–100 km	months	$\sim 10^{-1}$
Basin gyres	2000–15,000 km	years	$\sim 10^{-2}$
Ocean tides	100–1000 km	1/2 day, 1 day, ...	$\sim 10^{-4} - 10^{-2}$
Tsunamis	100 km	day	$\sim 10^2$

Table 2.1: Time and spatial scales of various oceanic phenomena. [23]

example those in the bay of Arcachon represented in figure 2.1(b), interact dynamically with the morphology of the coastal zone, transporting sediments and modifying continuously the shoreline and the bottom topography.

Table 2.1 gathers various oceanic phenomena and their scales. It also shows the *Rossby number* associated to those flows. Large-scale flows are the one that are influenced by earth's rotation. One measure of the significance of rotation for a particular motion is the Rossby number Ro. Let L, U and φ be, respectively, a length scale, a horizontal velocity scale and the latitude, characteristic of the motion. $\Omega = 7.3 \times 10^{-5} s^{-1}$ being the earth's rotation, the Coriolis parameter is given by $f = 2\Omega \sin\varphi$, and the Rossby number can be defined as follow:

$$Ro = \frac{U}{fL} \tag{2.1}$$

Consequently, large-scale flows are defined as those with sufficiently large L for Ro to be order one or less. When describing those motions in a rotating coordinates frame, the Coriolis force appears. The next section will show that whenever the Rossby number is small, the Coriolis force is important in the balance of forces.

2.1.2 Driving forces

The processes described earlier are the result of the balance of a few forces, distributed unevenly over the ocean volume: gravity, wind stress over the sea surface, buoyancy –due to difference in density of sea water, and, in a rotating frame

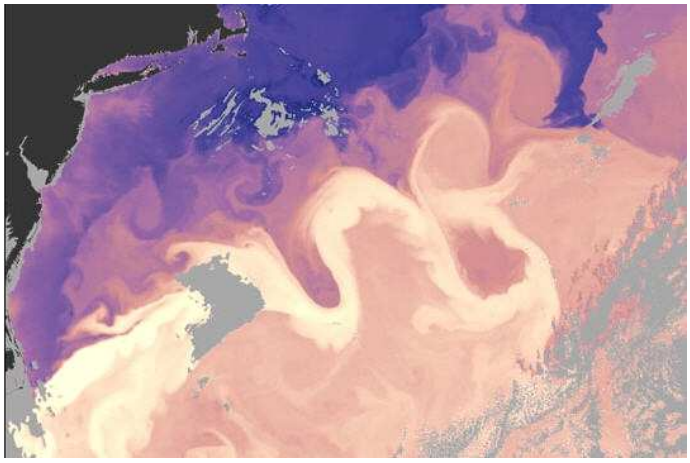

(a) Satellite view of the sea-surface temperature of the Gulf Stream on April 18^{th} 2005 showing cold mesoscale eddies (purple rings) on the south part of the Gulf Stream axis (white meandering current). Dark blue is around 5°C, purple is around 11°C, white is around 23°C. Image credits: NASA, MODIS Ocean Team

(b) Aerial view of Arguin sandbank formed, and transformed daily, by the interaction of tidal and rip boundary currents along the Great Dune of Pyla, at the south channel entrance to Arcachon Bay, Gironde, France. Image credits: G. Novelli

Figure 2.1: Illustration of different types of oceanic flows

of reference, Coriolis force.

Gravity: It is the dominant force giving rise to pressure forces and tides. The weight of the water in the ocean produces pressure, and the varying weight of water in different regions of the ocean produces horizontal pressure gradients. Changes in the gravitational pull exerted by the motion of the sun and moon relative to earth, produce periodic tides, tidal currents, and tidal mixing in the interior of the ocean.

Wind Stress: The stress exerted by the winds, blowing along the sea surface, transfers horizontal momentum to the sea, creating currents in the upper part of the water column. Wind blowing over waves on the sea surface leads to an uneven distribution of pressure over the waves. The pressure distribution transfers energy to the waves, causing them to grow into bigger waves.
In [21] and [22], the wind stress τ_{wind} is calculated from:

$$\tau_{wind} = \rho_a C_D^{wind} W_{10}^2 \tag{2.2}$$

where $\rho_a = 1.3$ kg/m^3 is the density of the air, W_{10} is wind speed at 10 m high, and C_D^{wind} is a drag coefficient depending on the wind speed but also on the wave height. Measurements of C_D^{wind} are based on measurements of turbulence in the marine boundary layer. Generally those measurements are not available and the physically correct calculation of the wind stress is not well known. Modellers often admit that, for moderate breeze (force 4 on Beaufort scale $W_{10} \sim 7.7$ m/s), wind-driven currents response is approximately 3 to 5% of wind velocity 10 meters above the sea.

Buoyancy: Buoyancy is the upward or downward force, $\vec{b}$, acting on a parcel of water (of density ρ) that is more or less dense than the surrounding water (of density ρ_0) at its level. It is defined as:

$$\vec{b} = \vec{g}\frac{\rho_0 - \rho}{\rho_0} \tag{2.3}$$

b is often referred to as the reduced acceleration due to gravity. The variations of density in the ocean are due to three effects : the compression of water by pressure (negligible even at maximum ocean depth), the thermal expansion, if its temperature changes, and the haline contraction if its salinity changes.

According to Vallis [24], these effects are approximated by the linear equation of state:

$$\rho = \rho_0 \left[1 - \beta_T (T - T_0) + \beta_S (S - S_0) + \frac{P}{\rho_0 c_s^2} \right] \tag{2.4}$$

where subscript ($_0$) corresponds to a measure of reference of ocean water, $\beta_T \approx 2 \times 10^{-4} \mathrm{K}^{-1}$, $\beta_S \approx 10^{-3} \mathrm{psu}^{-1}$ and $c_s \approx$1500 m.s^{-1} is the velocity of the sound in the ocean.

The density variations in the ocean are very small ($\sim$ 2%) compared to the mean density, but very important dynamically. For example, cold air blowing over the sea cools surface waters causing them to be more dense than the water beneath. The resulting buoyancy force causes the general circulation between cold pole water sinking and moving southward to resurface at warm equatorial regions. This force leads to oscillatory motions called *internal waves* (see table 2.1) which may travel through the stratified oceanic interior; or to convection and mixing in case of unstable stratification, like in the upper layer of the ocean, exchanging heat, fresh water and momentum with the atmosphere. On the shallow continental shelves, additional turbulent mixing induced by the tidal flow over the seabed may cause the entire water column to have a uniform density.

Coriolis: For large-scale flows ($Ro \ll 1$), taking place on a rotating sphere, it is convenient to introduce a co-rotating coordinates system which kinematically eliminates the rigid planetary rotation. Working in a frame rotating at Ω rotating rate, allows identify the small deviations from earth's rotation of ocean's motions known as currents. Then, the Coriolis force, $2\vec{\Omega} \times \vec{U}$, is the dominant force that arises from motion in the accelerating rotating frame. The study of the dynamics of large-scale oceanic flows must include the Coriolis force to be geophysically relevant.

For example in [25], to show the importance of Coriolis acceleration, van Heijst and Clercx consider a large-scale motion in a Cartesian rotating coordinates system (x,y,z) where x axis is pointing eastern, y northern and z vertically upward. In this system, the planetary rotation vector is decomposed as $\vec{\Omega} = (0, \Omega\cos\varphi, \Omega\sin\varphi)$, and a velocity vector as $\vec{U} = (u,v,w)$. Like in section 2.1.1 it is reasonable to assume that $w \ll u,v$. In this approach, the

components of the Coriolis term become

$$2\vec{\Omega} \times \vec{U} = (-fv, fu, -2\Omega u \cos\varphi) \tag{2.5}$$

where $f = 2\sin\varphi$ is the Coriolis parameter mentioned earlier in section 2.1.1, expressing that the effect of the planet's rotation varies with latitude φ. This gradient in $f(\varphi)$ can be approximated by applying a Taylor expansion around a reference latitude φ_0. The f-plane approximation is obtained by taking only the first term of the expansion : $f = f_0 = 2\sin\varphi_0$. It is valid for flows with limited extent in the north-south direction. By including the next term of the expansion, one obtains the β-plane approximation:

$$f = f_0 + \beta y \tag{2.6}$$

where $\beta = \frac{2\Omega\cos\varphi_0}{R}$, with R the radius of the globe. At mid-latitude ($\varphi_0 = 45°$) $f_0 \approx 10^{-4}\mathrm{s}^{-1}$ and $\beta \approx 2.10^{-11}\mathrm{m}^{-1}\mathrm{s}^{-1}$.
L and U being a length scale and a horizontal velocity scale, respectively, then for general circulation, extending over thousands of kilometers in the north-south direction, nearly steady and very slow, the order of the total acceleration would be

$$\frac{DU}{Dt} = o(1) \Leftrightarrow \frac{\partial U}{\partial t} + U \cdot (\nabla U) = o(1) \tag{2.7}$$

and then for the relative acceleration

$$\frac{\partial U}{\partial t} = O(U \cdot (\nabla U)) \Leftrightarrow \frac{\partial U}{\partial t} = O\left(\frac{U^2}{L}\right) \tag{2.8}$$

while the order of horizontal Coriolis acceleration is estimated as:

$$2\Omega \times U = O(fU) \tag{2.9}$$

finally the ratio of relative to Coriolis acceleration can be estimated by the Rossby number as in eq.(2.1):

$$Ro = \frac{U}{fL}$$

It is now apparent that Coriolis acceleration becomes dominant for large-scale flows. Further, in the absence of forcing and of dissipation, those flows are called *geostrophic*, i.e. governed only by the balance between Coriolis acceleration and horizontal pressure gradients (see for example [21, 23, 26]).

Major long-lived oceanic currents, gyres and mesoscale eddies all depend strongly on wind stress, thermohaline stratification and planetary rotation. But, if throughout the interior of oceans flow is almost frictionless, on the contrary, at the shallow coastal boundaries, viscosity becomes important in mixing and dissipation processes.

2.1.3 Dissipative forces

Although friction appears to be weak compared to Coriolis acceleration and pressure gradient, it plays a significant role within the ocean's boundary layers that separate the interior flow from the atmosphere on top, the seabed at bottom and the shoreline. Within these layers, the velocity changes rapidly from values typical of the interior to match the velocity of the other side of the boundary: zero at a solid boundary, or tens of centimeter per second at the sea surface for wind-driven circulation.

Molecular viscosity: Ultimately, momentum is transfered by the collision of molecules between them and their random motions. Molecular viscosity, or dynamic viscosity $\mu = \rho\nu$, is the macroscopic representation of this process. For example, for a flow in the (x,z) plane along x axis, $\rho\nu$ is defined as the ratio of the stress τ_{xz} tangential to the boundary and the shear velocity $U(z)$ at the boundary, as follows:

$$\tau_{xz} = \rho\nu\frac{\partial U}{\partial z} \tag{2.10}$$

This frictional force is responsible of the dissipation of kinetic energy i.e. the transformation of the kinetic energy into heat. But the length scales of ocean motions are too great for molecular viscosity to be significant: as mentioned in table 2.1, the dissipative scale driven by random molecular motions is on the order of millimeters.

Turbulence: Turbulence is described as rotational, energetic, eddying motions generating large gradients of velocity (or heat or concentration of solute) at small scales (1mm–1cm), promoting and enhancing dramatically viscous dissipation (or diffusion) process. The result is the dispersion of momentum, heat and solute, at rates far higher than those of molecular process alone.
Given the characteristic velocity gradient ($\sim 10^{-1} ms^{-1}$) through ocean's average depth ($\sim 4km$) and kinematic viscosity ($\nu \approx 10^{-6} m^2 s^{-1}$), the typical ocean's Reynolds number defined as:

$$Re = \frac{UL}{\nu} \tag{2.11}$$

can be estimated to be at least on the order of $10^8 - -10^9$. Hence the natural state of ocean is turbulent and it is expected to exhibit a wide range of turbulent scales. Breaking of surface and internal waves, buoyancy plumes resulting from surface cooling or haline diffusion due to evaporation, surface and bottom shear flows, are examples of motions leading to turbulent mixing within the various layers of the ocean.
By considering large-scale flows as a superposition of an averaged (spatially or temporally) component and a fluctuating turbulent contribution, it is possible to derivate a formulation of virtual turbulent stresses : the *Reynolds stresses*. By analogy with kinematic molecular viscosity in equation (2.10), an *eddy viscosity* (or eddy diffusivity for diffusion of heat or solute) A_z can be defined as follows:

$$\tau_{xz} = \rho A_z \frac{\partial U}{\partial z} \tag{2.12}$$

Values for the eddy viscosities (A_x A_y A_z) can be roughly estimated from direct measurements in the oceanic boundary layers, but, as properties of the flow, they may vary a lot spatially and temporally. In general, due to the stable density stratification of the water column, vertical mixing needs much more energy than horizontal mixing. In [21] are reported calculations and direct measurements of vertical eddy viscosity showing values ranging from $\sim 10^{-5}$ to $\sim 10^{-3}$ $m^2 s^{-1}$, while horizontal eddy viscosity values are on order of 10 to 100 $m^2 s^{-1}$.

Bottom stress: Bottom stress (τ_{bottom}) arises from seabed topography and bottom boundary layer effects. It is usually parameterized using a drag coefficient,

C_D^{bottom}, like in equation(2.2) for wind stress:

$$\tau_{bottom} = \rho_0 C_D^{bottom} U_h^2 \tag{2.13}$$

where ρ_0 is the depth averaged density of seawater, U_h represents the speed of the flow at a specified distance from the seabed (commonly 1 m), or the depth-averaged current in the shallow seas of the continental shelf. The value of C_D^{bottom} is about 2.5×10^{-3} [22] and can be expressed as a function of an empirical roughness parameter, such as Chezy's or Manning's coefficients.

The world of physical oceanography is very wide and not all of its aspects could have been covered here. For the modelling purpose of the present work, a limited, but significant, number of issues were presented.

2.2 Mathematical modelling

2.2.1 Ocean primitive equations

Based on Navier-Stokes equations, the fundamental equations for oceanic flows are in the form of a coupled set of partial differential equations that represent the conservation of momentum in a viscous fluid on the rotating earth. Together with mass conservation (the continuity equation), heat and salt conservation laws, they form a closed system of equations for oceanic dynamics. As the density variations are very small within the ocean, those equations are usually subject to the Boussinesq approximation and assume the incompressibility of the flow, which excludes sound and shock waves propagation of the study, as well as the hydrostatic approximation, which implies that vertical pressure gradients are due only to density. Boussinesq approximation consists in neglecting the effect of density differences on momentum, except in the term multiplying the gravitational acceleration $\vec{g}$ in order to account for buoyancy effects.
In vectorial form, the *ocean primitive equations* described by Bryan in [27], are

given by:

$$\vec{\nabla}\cdot\vec{U} = 0 \tag{2.14}$$

$$\frac{\partial\vec{U}}{\partial t}+\left[\vec{U}\cdot\vec{\nabla}\right]\vec{U} = -\frac{\vec{\nabla}P}{\rho}+\vec{b}-2\vec{\Omega}\times\vec{U}+\vec{D_U}+\vec{F} \tag{2.15}$$

$$\frac{\partial T}{\partial t}+\left[\vec{U}\cdot\vec{\nabla}\right]T = D_T+F_T \tag{2.16}$$

$$\frac{\partial S}{\partial t}+\left[\vec{U}\cdot\vec{\nabla}\right]S = D_S+F_S \tag{2.17}$$

$$\rho = \rho_0\left[1-\beta_T(T-T_0)+\beta_S(S-S_0)\right] \tag{2.18}$$

$$\frac{\partial P}{\partial z} = -\rho g \tag{2.19}$$

where $\vec{U}$ is the three-dimensional velocity vector that can be decomposed as a horizontal velocity vector $\vec{v}$ and a vertical component w such as $\vec{U}=(\vec{v},w)$, P is the pressure, $\vec{b}$ is the buoyancy defined in equation (2.3) with $g=9.81ms^{-2}$, $\Omega=7.3\times10^{-5}s^{-1}$ is the earth's angular velocity defined earlier. $\vec{D_U}$ (respectively D_T and D_S) stands for the viscous dissipation term (respectively diffusion for temperature and salinity). The assumption made, for the exchange of horizontal momentum (respectively temperature and salinity) from the sub-grid scale to the grid scale, is a Laplacian friction ($A_H\nabla^2U$) using an eddy viscosity (respectively diffusivity) parameter A_H (respectively κ_T and κ_S) with a magnitude much larger than the molecular values. $\vec{F}$ (F_T and F_S) represents any additional forcing term (e.g. wind forcing, heat fluxes, precipitation or evaporation). T is the temperature, S is the salinity, ρ is the density of sea water, $\rho_0=1035kgm^{-3}$ is the depth averaged value of ocean density (or Boussinesq density).

Equation (2.14) expresses the continuity for an incompressible fluid, equation (2.15) is the momentum balance equation, equations (2.16) and (2.17) are the equations for potential temperature T and salinity S as active tracers as they are coupled to equation (2.15) through equation (2.18) under the Boussinesq approximation. Equation (2.18) is an expression for the equation of state giving $\rho=\rho(\rho_0,T,S)$ and used for the calculation of the pressure P with the hydrostatic equation (2.19).

2.2.2 Limitations of ocean modelling

CFD[1] techniques are now widely used to simulate engineering and environmental fluid flows by numerically solving these equations [20, 21, 23, 28]. However, compared to industrial applications, the use of CFD for ocean modelling is a challenging task considering the large scales involved and the inherent uncertainties associated to the representation of turbulence and usually, the poor knowledge of boundary conditions. It is then important for an ocean modeller to understand what phenomena are being represented or resolved in the model and what scales are being parameterized, and more importantly are being imperfectly represented. Here are listed the principal issues related to the resolution of coastal ocean models.

Turbulence modelling: Different CFD techniques can be used to solve numerically the various possible forms of the Navier-Stokes equations.

The most fundamental solution method, which consists in resolving all the turbulence until the viscous scales of the flow, is referred to as the *Direct Numerical Simulation (DNS)*. In practice, at the high Reynolds number and typical spatial scales involved, DNS of oceanic flows remains computationally unfeasible.

Large Eddy Simulation (LES) is a technique that filters spatially Navier-Stokes equations. The large eddies are resolved while the sub-grid scale (scale of motions smaller than the grid resolution) is parameterized. LES is a relatively new field in coastal ocean modelling and its use is limited to domain scales less than about 2 km in length per 30 m in depth [29].

A common approach to model turbulent flows is to use the *Reynolds Averaged Navier–Stokes (RANS)* equations that represent the random character of turbulence with a statistical method. This has the advantage that a relatively coarse computational grid may be employed. However, large-scale complex unsteady oceanic flows are still difficult to solve and the RANS equations are often simplified by local equilibrium assumptions, parameterized using eddy coefficients in order to reduce the dimensions of the problem. [20, 29].

Regional scale and open boundary conditions: Ocean circulation above continental shelves is of special interest for oil spill trajectory predictions. Continental shelves are shallow regions, typically $\sim$ 200 m deep per $\sim$ 100 km

[1] Computational Fluid Dynamics

width, wide open to the ocean, and strongly tied dynamically to the basin, to the variations of the atmospheric conditions and to astronomical tides. In regional modelling, to solve the system of equations (2.15)–(2.19), it is necessary to prescribe artificial boundary conditions (flux of various quantities such as momentum, heat and passive tracers) along the open lateral boundaries of the domain. This is a difficult problem that modellers have been trying to solve in the last 30 years [30, 31]. A suitable open boundary condition is the one that, through the boundary, can evacuate the information coming from inside the domain, integer information from outside the domain, and make the model solution compatible with it. Different approaches can be used, for example convective boundary conditions, to avoid the reflection of information propagating outward the domain or to force the model with external data (from coarser models predictions or observations). Often these approaches consist in simplified equations that may propagate errors in the model solution. The simplest way to damp these errors is then to locate the open boundary as far as possible (depending on the computational resources and the model resolution) from the area of interest.

Initialization and forcing: Operational models, used to predict contaminant transport for example, require extensive observational data for initialization, forcing at boundaries, and parameterization of subgrid-scale phenomena. Unfortunately the sets of measurements of bathymetry, currents velocity, temperature, salinity, and turbulence are sparse (with the notable exception of abundant surface data remotely collected by satellite), and can contain significant and poorly known errors. This aspect directly affects the quality of the predictions as the introduced uncertainties may be compensating, interacting and non-linear. Consequently, there may be many combinations of models and parameters that fit the available data equally well [20].

It suggests that special care is required to represent complex coastal flows on regional scale with CFD. A successful simulation relies on the understanding of the simplifications introduced in the model, the quality of the grid, the numerical techniques implemented to solve the governing equations and the quality of the data used to parameterize and validate the model.

2.2.3 Derivation of the hydrodynamic model

The intended application of the model for the transport of surface oil spill above continental margins, and the computational pre- and post-processing capabilities available, account for the choice of a particular simplified representation of the hydrodynamics of coastal sea currents.
The model is derived from the vertical integration of the ocean primitive equations (2.15)–(2.19) under the rigid-lid approximation. The rigid-lid streamfunction-vorticity method is then employed to eliminate the pressure from the equations and enforce the non-divergence of the velocity field. Therefore the system of equations describing the flow is considerably simplified, containing only 2 equations to be solved instead of 6 in the primitive formulation, making consequently the numerical solution of the problem faster and more efficient.

2.2.3.1 Depth-averaged Navier-Stokes equations

It is assumed that the coastal ocean can be approximated as a shallow, vertically homogeneous, rotating fluid layer of density ρ_0 flowing over topography: the Coriolis acceleration can be important, the aspect ratio of the motion is small and the density stratification is absent. The shallow water equations governing such a flow are obtained by integrating over the depth the primitive ocean equations (2.15)–(2.17) under the assumption of incompressibility and constant density. The integration takes place from the bed , $z = H$, to the free surface, $z = \eta$, defined in figure 2.2, and all the parameters are expressed in terms of depth-averaged values.
Here, the depth-averaged velocity $\vec{U_h} = (U_h, V_h)$ is defined by:

$$U_h = \frac{1}{h}\int_H^\eta u\partial z \quad ; \quad V_h = \frac{1}{h}\int_H^\eta v\partial z \tag{2.20}$$

The momentum equation (2.15) can be easily integrated over the depth to give:

$$\frac{\partial \vec{U_h}}{\partial t} + \left[\vec{U_h}\cdot\vec{\nabla}\right]\vec{U_h} = -h\frac{\vec{\nabla}P}{\rho_0} - 2\vec{\Omega}\times\vec{U_h} + \vec{D}_U^h + \vec{F_h} \tag{2.21}$$

$D_U^h = \int_H^\eta A_H\nabla^2 U\partial z$ represents the depth averaged dissipation of horizontal momentum at sub-grid scales. $\vec{F_h}$ are surface forcing terms resulting from the integration

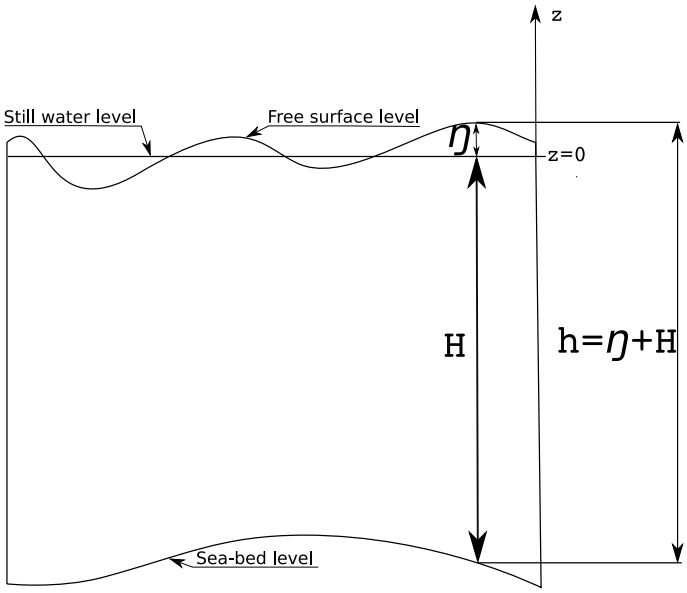

Figure 2.2: Sketch of a shallow layer of fluid with a free surface. The height η is the deviation from a resting ocean state, and $H < 0$ is the vertical position of the layer bottom.

of the frictional shear stress at the bottom and surface of the water column:

$$\vec{F}_h = \frac{(\vec{\tau}_{wind} - \vec{\tau}_{bottom})}{\rho_0 h} = \frac{\Delta\vec{\tau}}{\rho_0 h} \tag{2.22}$$

.

The buoyancy disappeared from the equation as ρ_0 is constant and uniform. For the same reason temperature and salinity are not coupled dynamically to momentum and are transported by the flow like any passive tracer ϕ as in the following equation:

$$\frac{\partial \phi}{\partial t} + \left[\vec{U}_h \cdot \vec{\nabla}\right] \phi = D^h_\phi + F_\phi \tag{2.23}$$

The vertical integration of the continuity equation (2.14) and the non orthogonal flux condition at the bottom yield to:

$$\frac{\partial h}{\partial t} + \vec{\nabla} \cdot \left(h\vec{U}_h\right) = 0 \tag{2.24}$$

The shallow water equations are (2.21) and (2.24).

2.2.3.2 Rigid-lid approximation

The key assumption with the rigid-lid approximation is that the ocean surface height η is fixed

$$\eta \equiv 0 \quad ; \quad h = H \tag{2.25}$$

This assumption eliminates the gravity waves associated to vertical displacements of the full water column.
A related assumption is to set the vertical velocity w at the surface to zero,

$$w(z=0) = 0 \tag{2.26}$$

In such way, the free surface effects are neglected ($\frac{\partial h}{\partial t} = 0$), and the depth-integrated continuity equation under the rigid lid assumption renders:

$$\vec{\nabla} \cdot \left(H\vec{U}_h \right) = 0 \tag{2.27}$$

It should be noted that these last two assumptions also implies that the upper boundary is effectively closed to surface water flux. This choice, as it limits strongly the ocean-atmosphere interactions, would not be satisfactory for large scale oceanic modelling as it eliminates some fundamental motions of the circulation, as mentionned by many authors [21, 22, 27].

2.2.3.3 Vorticity and streamfunction formulation

The depth integrated flow HU_h is non divergent, thus it is possible to derivate $\vec{U}_h$ from a volume transport streamfunction $\vec{\psi}$:

$$\vec{U}_h = \frac{1}{H}\vec{\nabla} \times \vec{\psi} \tag{2.28}$$

Therefore the difference between two isolines of the streamfunction ψ can be interpreted as the vertically integrated volume transport between those lines.

As pointed out by Grau in [32,33], to eliminate the pressure from the momentum equation (2.21), it is sufficient to derive the time evolution of vorticity. For two-dimensional domains, the Helmholtz transformation defines the vorticity $\vec{\omega}$ as:

$$\vec{\omega} = \vec{\nabla} \times \vec{U}_h \quad \text{and} \quad \vec{\nabla} \cdot \vec{\omega} = 0 \tag{2.29}$$

It should be noted that $\vec{\omega} = (0,0,\omega_z)$ and $\vec{\psi} = (0,0,\psi_z)$ have only one vertical component and can be treated as scalar (ω and ψ) from now on. Introducing equation (2.28) into equation (2.29) yields to a Poisson-like equation for the streamfunction:

$$\omega = -\frac{1}{h}\nabla^2\psi + \frac{1}{h^2}\vec{\nabla}h \cdot \vec{\nabla}\psi \tag{2.30}$$

Now, taking the curl of the depth-integrated momentum equation (2.21) and applying the definition of vorticity of equation (2.29), after some algebraic developments and rearrangements, the equation for the transport of vorticity is obtained:

$$\frac{\partial \omega}{\partial t} + \vec{U}_h \cdot \vec{\nabla}(\omega + 2\Omega) = \frac{\omega + 2\Omega}{h}\left(\vec{U}_h \cdot \vec{\nabla}h\right) + D^h_\omega + \left(\vec{\nabla} \times \vec{F}_h\right) \cdot \vec{k} \tag{2.31}$$

This is the vorticity equation for an incompressible fluid over topography in rotating coordinates. $(\omega + 2\Omega)$ is called the *absolute vorticity*, a combination of relative vorticity ω and planetary vorticity 2Ω. The second term on the left side represents the convection of the absolute vorticity by the relative depth-averaged horizontal velocity $\vec{U}_h$. The pressure term disappeared from the right side because the curl of a gradient ($\nabla \times \nabla P$) equals zero. $\frac{\omega+2\Omega}{h}$ is called *potential vorticity*. D^h_ω represents the depth-averaged production, diffusion or dissipation of vorticity at small scales ($D^h_\omega = \int_H^0 A_H \nabla^2 \omega$). The last term of the right side of equation (2.31), the curl of the depth integrated surface minus bottom stresses $\left(\vec{\nabla} \times \vec{F}_h\right) \cdot \vec{k}$, represents the vorticity production or dissipation due to friction of the water column with the upper and lower boundaries. It can be noticed that, in the absence of dissipation, the equation can be simplified and rearranged as:

$$\frac{D}{Dt}\left(\frac{\omega + 2\Omega}{h}\right) = 0 \tag{2.32}$$

which expresses the conservation of potential vorticity, an important notion in geophysical fluid dynamics as it explains how large-scale atmospheric and oceanic flows acquire (or lose) vorticity when their latitude and/or depth change.

In summary, this rigid-lid streamfunction-vorticity model allows for the description of shallow turbulent rotating flows, as long as gravity waves and buoyancy are not dominant motions. With this model of only two equations, and applying the appropriate boundary conditions, the vorticity field can be obtained from equation (2.31), and then the corresponding streamfunction can be calculated from equation

(2.30). Once the flow field (ω, ψ) has been totally solved, the velocities can be recovered analytically from the streamfunction with equation (2.28).

2.2.3.4 Initial conditions

The initialization of the model only requires values of the velocity field. The vorticity can be calculated by equation (2.29) and then the streamfunction can be found by solving the Poisson equation (2.30). The velocity field can be initialized at zero (for most of the validation tests), or from interpolation between known velocities (or velocity profiles) at certain locations.

2.2.3.5 Boundary conditions

The regional model of coastal ocean is bounded by complex coastlines and the rest of the ocean at its lateral sides, bottom topography at its base and air-sea interface at its top.

Bottom and top boundaries are defined by the surfaces $z = H$ and $z = \eta = 0$. Through these boundaries the ocean can exchange heat, fresh water, salt and momentum. However on time scales of a few days these fluxes are so weak that they can be neglected. This approximation is reflected in the constant density hypothesis and the rigid-lid approximation. Only the frictional processes are parameterized (see the wind and bottom stresses formulations in equations (2.2) and (2.13)).

Along the coastline it is assumed that:

1. there is no flow normal to any solid boundary, wich means no flow through the shoreline. It implies that:

$$\vec{n} \cdot \vec{U_h} = 0 \Leftrightarrow \vec{n} \cdot \vec{z} \times \vec{\nabla}\psi = 0 \Leftrightarrow \vec{t} \cdot \vec{\nabla}\psi = 0 \tag{2.33}$$

   where $\vec{n}$ is a unit vector orthogonal to the boundary and $\vec{t}$ is tangential. This constraint says that the streamfunction is constant along the coastline.
2. There is no flow parallel to a solid boundary, which means no slip at the shoreline. The no-slip vorticity boundary condition is derived from vorticity definition equation (2.29) in function of the velocity $\vec{U_h}$.

The treatment of the open lateral boundaries has to be taken carefully. Several methods are implemented in the model that allow information to enter or leave the domain without contaminating the solution in the area of interest:

Inflow condition: whenever velocity profiles or flow rates are available they are assigned at the entrance of the domain.

Entrainment condition: when there is no indication about the flow crossing a boundary, the entrainment condition defined Kanna and Das in [34] is used. It states that normal velocity gradient is zero:

$$\vec{n} \cdot \vec{\nabla} U_h = 0 \tag{2.34}$$

Outflow condition: in the downstream direction several outlet boundary conditions have been tested depending on the flow configuration.

- It is sometimes possible to assume that the domain is periodic. For example when the main flow remains at the same latitude (zonal flow) and when the topography of the bed is similar at the entrance and at the exit of the domain, then one can assume the periodicity of the flow:

$$\vec{U}_h^{in} = \vec{U}_h^{out} \quad \text{and} \quad \omega^{in} = \omega^{out} \tag{2.35}$$

- Another simple condition is to assume that streamwise gradients of $\vec{U}_h$ and ω are zero:

$$\vec{n} \cdot \vec{\nabla} U_h = 0 \quad \text{and} \quad \vec{n} \cdot \vec{\nabla} \omega = 0 \tag{2.36}$$

- For unsteady problems, the best suited boundary condition for moving structures out of the computational domain was the convective boundary condition defined by Grau [35] and successfully applied more recently in [36, 37] :

$$\frac{\partial \omega}{\partial t} + U_h^n \nabla^n(\omega) = 0 \tag{2.37}$$

where $U_h^n = \vec{U}_h \cdot \vec{n}$ and $\nabla^n = \vec{\nabla} \cdot \vec{n}$.

To compute the flow field in a coastal region of the oceans, the system of vectorial equations formed by equations (2.21), (2.30) and the boundary conditions, has to be projected and discretized on a system of coordinates. A boundary-fitted coordinates system has the advantage to conform to the naturally complex shape of natural coastlines and leads to a simple formulation of the boundary condition equations.

2.3 Generalised coordinates framework

The choice of *generalised* (or *curvilinear*, or *boundary-fitted*) coordinates is natural in this context because at the origin of this project, the oil slick transport model had already been projected and discretized on this system of coordinates [11, 38]. The generalised coordinates system are often used to calculate flows in complex geometries. Since the grid lines follow the boundaries, the boundary conditions formulations are simplified. The grid can also be adapted to the flow, following the streamlines to enhance the accuracy. A generalised mesh allows to control the grid spacing in the domain in order to concentrate points in the regions of interest and have an efficient and accurate computation of the flow.
The projection on a curvilinear coordinates system also have several drawbacks. For instance, the differential operators in generalised coordinates are much more complex and the transformed equations contain more terms thereby increasing the difficulty of programming and the computational costs.

2.3.1 Curvilinear coordinates system

The basic idea of boundary conforming curvilinear system is to have some coordinate line coincident with each boundary segment. The other curvilinear coordinate will vary monotonically along the orthogonal boundary line. The use of coordinate line intersection to define the grid points allows to define a fixed computational Cartesian grid (see figure 2.3) where the system of partial differential equations (2.21) and (2.30) has been transformed so that the curvilinear coordinates replace the Cartesian coordinates as the independent variables. In this section, the relationships between the physical (x,y,z) and the computational (ε,η,z) coordinates are established.
It is assumed that there is a unique, single-valued, functional relationship between

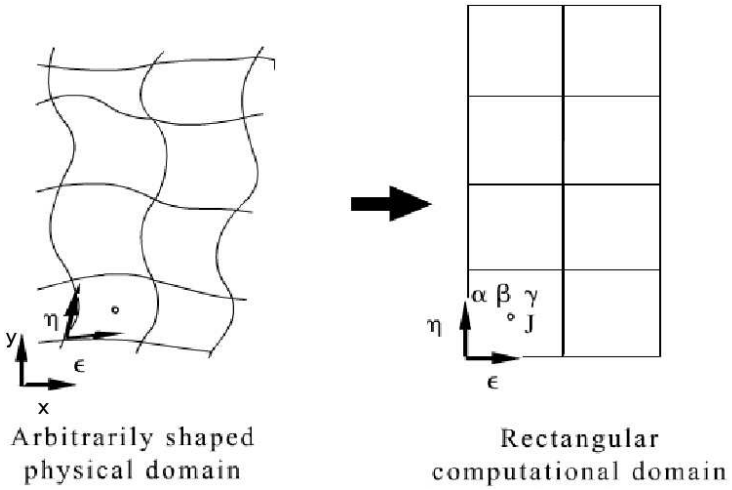

Figure 2.3: Conforming coordinates transformation

the generalised coordinates and the physical coordinates, in which case each grid line is a line of constant coordinate ε_j (with $j = 1,2,3$ and $\varepsilon_1 = \varepsilon$, $\varepsilon_2 = \eta$, $\varepsilon_3 = z$): $T : \varepsilon_j = \varepsilon_j(x,y,z)$. The elements of the transformation matrix are defined by:

$$T_j^i = \frac{\partial x_i}{\partial \varepsilon_j} \tag{2.38}$$

This transformation is valid only if the Jacobian J of the transformation verifies:

$$J = det\left(\frac{\partial x_i}{\partial \varepsilon_j}\right) \neq 0 \tag{2.39}$$

It is then convenient to define the metric tensor g_{ij}, which relates the increment in distances in the Cartesian coordinates (x,y,z) in the physical space, to the changes in distance in the generalised coordinates (ε,η,z) in the computational space (figure 2.3):

$$g_{ij} = \frac{\partial x_k}{\partial \varepsilon_i}\frac{\partial x_k}{\partial \varepsilon_j} \tag{2.40}$$

The metric tensor covariant components α, γ, β and J can be defined as:

$$\alpha = g_{22} = \left(\frac{\partial x}{\partial \eta}\right)^2 + \left(\frac{\partial y}{\partial \eta}\right)^2 \tag{2.41}$$

$$\gamma = g_{11} = \left(\frac{\partial x}{\partial \varepsilon}\right)^2 + \left(\frac{\partial y}{\partial \varepsilon}\right)^2 \tag{2.42}$$

$$\beta = g_{12} = g_{21} = \frac{\partial x}{\partial \varepsilon}\frac{\partial x}{\partial \eta} + \frac{\partial y}{\partial \varepsilon}\frac{\partial y}{\partial \eta} \tag{2.43}$$

$$J = \left(\alpha\gamma - \beta^2\right)^{\frac{1}{2}} = \frac{\partial x}{\partial \varepsilon}\frac{\partial y}{\partial \eta} - \frac{\partial x}{\partial \eta}\frac{\partial y}{\partial \varepsilon} \tag{2.44}$$

For tensor manipulations, the contravariant formulation of the metric tensor components gives:

$$g^{11} = \frac{\alpha}{J^2} \tag{2.45}$$

$$g^{22} = \frac{\gamma}{J^2} \tag{2.46}$$

$$g^{12} = g^{21} = -\frac{\beta}{J^2} \tag{2.47}$$

The transport equations exhibit several differential operators like the curl of a vector ($\vec{\nabla} \times \vec{A}$), the divergence of a vector ($div\vec{A}$) and the Laplacian of a scalar ($\nabla^2 f$) which expressions are given here:

$$\vec{\nabla} \times \vec{A} = \frac{E^{ijk}}{J}(g_{kp}A^p)_{,j} = \frac{E^{ijk}}{J}A_{k,j} \tag{2.48}$$

$$\vec{\nabla} \cdot \vec{A} = A^i_{,i} = \frac{1}{J}\frac{\partial (JA^i)}{\partial \varepsilon_i} \tag{2.49}$$

$$\nabla^2 f = \frac{1}{J}\frac{\partial}{\partial \varepsilon_j}\left(Jg^{ij}\frac{\partial f}{\partial \varepsilon_i}\right) \tag{2.50}$$

where E^{ijk} is the permutation symbol and a third order contravariant tensor, taking on the values ± 1 according as ijk is an even or odd permutation of 123 and is zero if any of i, j and k are equal, following the tensorial notation of Aris [39]. More details about the covariant differentiation of tensors and index notations can be found in [32, 33, 37, 39].

2.3.2 Governing equations in generalised coordinates

It is assumed that a boundary-fitted coordinates system (ε, η, z) has been defined. The governing equations (2.21) and (2.30) can be expressed in generalised coordinates using the differential operators described by equations (2.38)–(2.50).

Velocity

Cartesian coordinates all have physical dimensions of length but in general this cannot be expected of curvilinear coordinates. For non-orthogonal coordinates, the definition of the physical components is not simple. It is easier to formulate the equation for the transport of vorticity in function of the contravariant $(U_h^\varepsilon, U_h^\eta)$ components of the velocity. These components are related to the cartesian physical components (U_h^x, U_h^y) by the following equations:

$$U_h^\varepsilon = \frac{\frac{\partial y}{\partial \eta}}{J} U_h^x + \frac{-\frac{\partial x}{\partial \eta}}{J} U_h^y \tag{2.51}$$

$$U_h^\eta = \frac{-\frac{\partial y}{\partial \varepsilon}}{J} U_h^x + \frac{\frac{\partial x}{\partial \varepsilon}}{J} U_h^y \tag{2.52}$$

$$U_h^x = \frac{\partial x}{\partial \varepsilon} U_h^\varepsilon + \frac{\partial x}{\partial \eta} U_h^\eta \tag{2.53}$$

$$U_h^y = \frac{\partial y}{\partial \varepsilon} U_h^\varepsilon + \frac{\partial y}{\partial \eta} U_h^\eta \tag{2.54}$$

These equations allow to switch from real velocities to computational velocities (and vice-versa) to initialize the calculations when a real velocity field is known or inversely to recover the real velocities at the end of a calculation.
Sometimes it is the stream function field that is known and the velocities can be calculated applying equations (2.28) and (2.48):

$$U_h^\varepsilon = \frac{1}{JH} \frac{\partial \psi}{\partial \eta} \quad \text{and} \quad U_h^\eta = -\frac{1}{JH} \frac{\partial \psi}{\partial \varepsilon} \tag{2.55}$$

Continuity

With all the terms arranged on the left hand side, the continuity equation (2.30) expressed in generalised coordinates reads:

$$h\omega + \left[\frac{\alpha}{J^2} \frac{\partial^2 \psi}{\partial \varepsilon^2} + \frac{\gamma}{J^2} \frac{\partial^2 \psi}{\partial \eta^2} - \frac{2\beta}{J^2} \frac{\partial^2 \psi}{\partial \varepsilon \partial \eta} + C \frac{\partial \psi}{\partial \varepsilon} + D \frac{\partial \psi}{\partial \eta} \right] = 0 \tag{2.56}$$

where the auxiliary functions C and D are defined by:

$$C = \left(A - \frac{\alpha}{hJ^2}\frac{\partial h}{\partial \varepsilon} + \frac{\beta}{hJ^2}\frac{\partial h}{\partial \eta} \right) \tag{2.57}$$

$$D = \left(B - \frac{\gamma}{hJ^2}\frac{\partial h}{\partial \eta} + \frac{\beta}{hJ^2}\frac{\partial h}{\partial \varepsilon} \right) \tag{2.58}$$

and functions A and B are defined by:

$$A = \frac{1}{J}\left[\frac{\partial}{\partial \varepsilon}\left(\frac{\alpha}{J}\right) - \frac{\partial}{\partial \eta}\left(\frac{\beta}{J}\right) \right] \tag{2.59}$$

$$B = \frac{1}{J}\left[\frac{\partial}{\partial \eta}\left(\frac{\gamma}{J}\right) - \frac{\partial}{\partial \varepsilon}\left(\frac{\beta}{J}\right) \right] \tag{2.60}$$

Transport of Vorticity

To simplify the expression, only the seabed friction terms is considered in this expression of the equation for the transport of vorticity in generalised coordinates:

$$\begin{aligned} \frac{\partial \omega}{\partial t} = & -U_h^{\varepsilon}\frac{\partial(\omega + 2\Omega)}{\partial \varepsilon} - U_h^{\eta}\frac{\partial(\omega + 2\Omega)}{\partial \eta} \\ & + \frac{\omega + 2\Omega}{h}\left(U_h^{\varepsilon}\frac{\partial h}{\partial \varepsilon} + U_h^{\eta}\frac{\partial h}{\partial \eta} \right) \\ & + \nu_H \left[\frac{\alpha}{J^2}\frac{\partial^2 \omega}{\partial \varepsilon^2} + \frac{\gamma}{J^2}\frac{\partial^2 \omega}{\partial \eta^2} - \frac{2\beta}{J^2}\frac{\partial^2 \omega}{\partial \varepsilon \partial \eta} + A\frac{\partial \omega}{\partial \varepsilon} + B\frac{\partial \omega}{\partial \eta} \right] \\ & - \frac{C_D^{bottom}}{J}\left[\frac{\partial}{\partial \varepsilon}\left(\beta\frac{|U_h|}{h}U_h^{\varepsilon} + \alpha\frac{|U_h|}{h}U_h^{\eta} \right) - \frac{\partial}{\partial \eta}\left(\gamma\frac{|U_h|}{h}U_h^{\varepsilon} + \beta\frac{|U_h|}{h}U_h^{\eta} \right) \right] \end{aligned} \tag{2.61}$$

where

$$|U_h| = (g_{ij}U^i U^j)^{1/2} = \left[U_h^{\varepsilon}(\gamma U_h^{\varepsilon} + \beta U_h^{\eta}) + U_h^{\eta}(\beta U_h^{\varepsilon} + \alpha U_h^{\eta}) \right]^{1/2} \tag{2.62}$$

Equations (2.56) and (2.61), along with the appropriate initial and boundary conditions, form a closed system of equations describing shallow turbulent and rotating coastal oceanic flows. Although this streamfunction-vorticity formulation is complex in generalised coordinates, it is specially adapted to the requirements of complex geometry systems and oceanic flows features.

Chapter 3

Numerical Methods

A transformation of the continuous physical space into a discrete computational domain is necessary to solve the discrete system of differential equations established previously. This chapter describes the numerical methods used in the numerical simulations of coastal oceanic flows.
Section 3.1 explains the generation of the curvilinear mesh and the procedure used to interpolate the bathymetry over the grid.
The governing equations for the coastal flow, along with the initial and boundary conditions, are discretized by means of a Finite Differences Method (FDM) of second order accuracy in space and in time. The numerical scheme to solve the governing equation of the oil slick movement is upgraded from second to fourth order in time and from first to second order in space. The spatial discretizations, the time advancement schemes and the solvers are presented in section 3.2.
Finally, in section 3.3, the solvers have been implemented following the Open MP specifications to allow running the code on shared-memory computers, and consequently speed up the resolution of the equations.

3.1 Computational domain

As seen in chapter 2, coastal ocean flows and spreading of oil slicks can be described by partial differential equations. The numerical solution of such equations requires the discretization of the field into a collection of points or cells. The differential equations are approximated by a set of algebraic equations and this system of algebraic equations is then solved on a computer. As pointed out by Ferziger and

Peric [28], the accuracy of numerical solutions is directly dependent on the quality of discretizations and interpolations used.

3.1.1 Curvilinear grid generation

The basic idea is to generate a curvilinear coordinate system that covers the domain of the marine area with coordinate lines coincident with the boundaries. For this purpose, a module of SIMOIL is used. Basically, it is a FORTRAN routine based on a numerical procedure from Thompson et al. [40] which consists in:

1. Specification of the coordinates of the boundaries of the domain for the generalised grid generation.

2. Numerical solution of the Poisson equations for the stream function Ψ and velocity potential Φ corresponding to a potential (inviscid and irrotational) flow passing through the domain:

$$\nabla^2\Psi = P \tag{3.1}$$

$$\nabla^2\Phi = Q \tag{3.2}$$

   P and Q are functions controlling the space in between, and the orientation of the isolines of Ψ and Φ. This system of equations is discretized by means of finite differences with a central scheme of second order accuracy and solved by the successive over relaxation (SOR) methodology.

3. Calculation of the geometric coefficients $(\alpha, \beta, \gamma, J, A, B)$ at each point of the new grid.

4. Iterative procedure until a near-orthogonal grid is obtained.

The streamlines and lines of constant potential constitute a truly orthogonal coordinate system. This process allows to distribute the coordinate lines smoothly, achieving near-orthogonality specially close to the boundaries, and to concentrate lines in regions of strong gradients. The application of boundary conditions is easy: conditions involving normal derivatives can be represented by one-side differences expressions along the line emerging from the boundary. The accuracy deteriorates if the departure from orthogonality is too large. In such a case, it is convenient

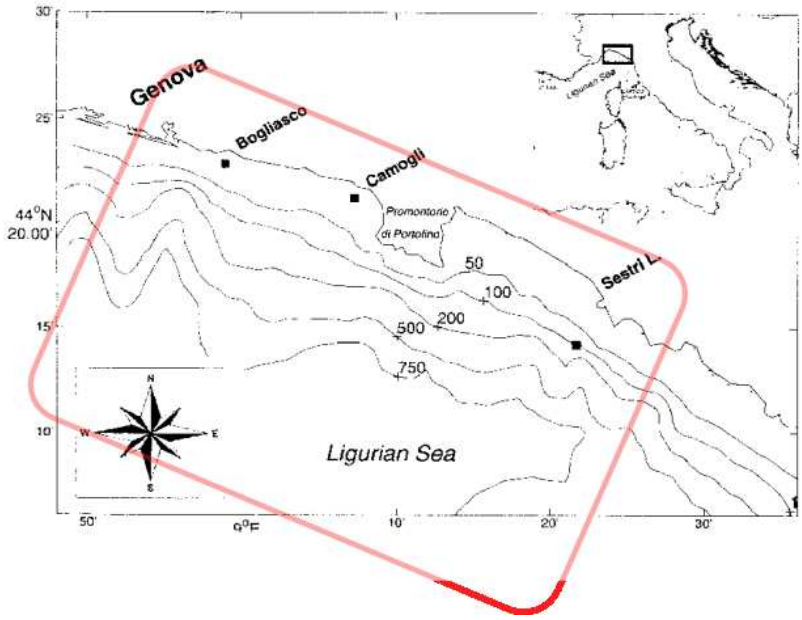

Figure 3.1: Marine chart with latitude and isobath of Portofino area

to cut the domain in several sub-domains, then to generate separately the coordinate system of each sub-region, and finally to patch them together to form a complete system. An illustration can be seen in figures 3.1 and 3.2 for the study of the Promontorio di Portofino area. The computed grid is generated by the intersections of the lines of the boundary-fitted coordinate system.

3.1.2 Interpolation of bathymetry

Bathymetry stands for the measurement of the spatial variability of the bottom of oceans, seas and lakes. Several techniques can be used to draw bathymetric charts, representing the seafloor relief or depth contours. Ships equipped with multibeam echosounders and Global Positioning System (GPS) allow collecting the sounding and locations measurements which are later processed to produce a depths map of the area. Aerial Laser scanning surveys (LIDAR/LADAR) can be conducted by airplane. Satellites are also used to measure bathymetry. They can detect subtle variations in sea level caused by undersea mountains or trenches.

In this work, the computational domain is generated from a digitalized marine map. The latitude, the four boundaries and several isobaths (contour lines of equal

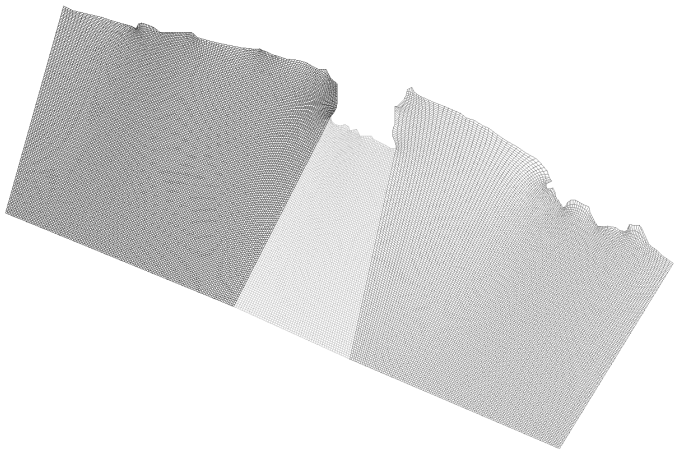

Figure 3.2: Generalised mesh of Portofino area made of 3 adjacent sub-domains

depths) are extracted from the map. The isobaths are collected as a set of data points (X,Y) associated to depth data values (Z). Once the curvilinear mesh has been generated, it is possible to construct a smooth interpolation function Z(X,Y) which agrees with the given data and can be evaluated at every points of the grid. This is done using a bivariate data interpolation library developed by Akima [41,42].

An illustration of the generation of a computational domain can be seen in the figures 3.1, 3.2 and 3.3. The first picture shows the nautical chart in the area of Promontorio di Portofino, close to Genova, Italy. The domain is defined by a red rectangle, and a dozen of representative points per isobaths are selected. In figure 3.2 the domain has been divided into three subdomains, each of them meshed independently with coincident boundary points. The last figure 3.3 shows the final curvilinear grid and its isobaths, superimposed over a three dimensional representation of the bathymetry of the computational domain.

3.2 Discretization of the governing equations

According to Lin and Chandler-Wide [43], the two types of numerical model that are most used in solving the two dimensional depth-integrated shallow water equations are the finite differences method (FDM) and the finite elements method (FEM). In the case of FDM, rectangular finite difference grids are the most widely used for the transport of contaminant. However, with such grids, curved boundaries

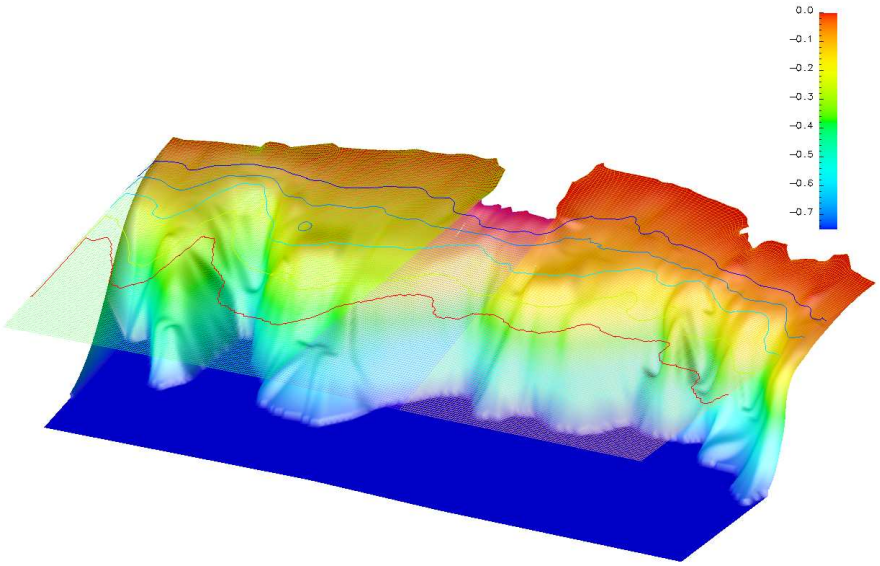

Figure 3.3: 3-D representation of the interpolated bathymetry in the area of Portofino. (The depth is expressed in km)

are replaced by a staircase of grid points. Then it is necessary to choose between a high density of points on the boundary or a poor resolution of boundary flows. Boundary fitted coordinates systems tackle this issue allowing the use of FDM with an accurate resolution even for irregular geometries.

3.2.1 Evaluation of spatial derivatives

The partial differential equations (2.56) and (2.61) are solved in the uniform orthogonal computational space using second-order centred-difference approximations. Finite difference approximations of the partial derivatives appearing in the partial differential equations are developed by writing Taylor series for the dependent variable at several neighboring points using grid point (i, j) as the base point, and combining these Taylor series to solve for the desired partial derivatives. A function $\Phi(\varepsilon, \eta)$ at grid point (i, j) is denoted by

$$\Phi(\varepsilon_i, \eta_j) = \Phi_{i,j} \tag{3.3}$$

and his derivatives are denoted by

$$\frac{\partial \Phi(\varepsilon_i,\eta_j)}{\partial \varepsilon} = \left.\frac{\partial \Phi}{\partial \varepsilon}\right|_{i,j} \quad \text{and} \quad \frac{\partial^2 \Phi(\varepsilon_i,\eta_j)}{\partial \varepsilon^2} = \left.\frac{\partial^2 \Phi}{\partial \varepsilon^2}\right|_{i,j} \tag{3.4}$$

Centred space finite difference approximations are shown below for several derivatives:

First spatial derivative

$$\left.\frac{\partial \Phi}{\partial \varepsilon}\right|_{i,j} = \frac{\Phi_{i+1,j} - \Phi_{i-1,j}}{2\Delta\varepsilon} + o(\Delta\varepsilon^2) \tag{3.5}$$

Second spatial derivative

$$\left.\frac{\partial^2 \Phi}{\partial \varepsilon^2}\right|_{i,j} = \frac{\Phi_{i+1,j} - 2\Phi_{i,j} + \Phi_{i-1,j}}{2\Delta\varepsilon^2} + o(\Delta\varepsilon^2) \tag{3.6}$$

Mixed derivative

$$\left.\frac{\partial^2 \Phi}{\partial \varepsilon \partial \eta}\right|_{i,j} = \frac{\Phi_{i+1,j+1} - \Phi_{i+1,j-1} - \Phi_{i-1,j+1} + \Phi_{i-1,j-1}}{4\Delta\varepsilon\Delta\eta} + o(\Delta\varepsilon^2, \Delta\eta^2) \tag{3.7}$$

On the boundaries, one-sided difference second order accurate formula are used:

On the lower boundary (where $\eta = 1, \forall\varepsilon$) for the first derivative

$$\left.\frac{\partial \Phi}{\partial \eta}\right|_{i,j=1} = \frac{-3\Phi_{i,j} + 4\Phi_{i,j+1} - \Phi_{i,j+2}}{2\Delta\eta} + o(\Delta\eta^2) \tag{3.8}$$

And the second derivative reads

$$\left.\frac{\partial^2 \Phi}{\partial \eta^2}\right|_{i,j=1} = \frac{2\Phi_{i,j} - 5\Phi_{i,j+1} + 4\Phi_{i,j+2} - \Phi_{i,j+3}}{\Delta\eta^2} + o(\Delta\eta^2) \tag{3.9}$$

The partial differential equations (2.56) and (2.61) are solved in the uniform orthogonal computational space using second-order centred-difference approximations.

3.2.2 Discretization of the hydrodynamic equations

3.2.2.1 Spatial discretization of the Poisson equation

Considering the Poisson equation (2.56), the second-order finite difference approximation at grid point (i, j) yields

$$\begin{aligned}(\omega h)_{i,j} \quad & + \left(\frac{\alpha}{J^2}\right)_{i,j} \frac{\psi_{i+1,j} - 2\psi_{i,j} + \psi_{i-1,j}}{\Delta\varepsilon^2} \\ & + \left(\frac{\gamma}{J^2}\right)_{i,j} \frac{\psi_{i,j+1} - 2\psi_{i,j} + \psi_{i,j-1}}{\Delta\eta^2} \\ & - \left(\frac{2\beta}{J^2}\right)_{i,j} \frac{\psi_{i+1,j+1} - \psi_{i+1,j-1} - \psi_{i-1,j+1} + \psi_{i-1,j-1}}{4\Delta\varepsilon\Delta\eta} \\ & + C_{i,j} \frac{\psi_{i+1,j} - \psi_{i-1,j}}{2\Delta\varepsilon} \\ & + D_{i,j} \frac{\psi_{i,j+1} - \psi_{i,j-1}}{2\Delta\eta} = 0\end{aligned} \tag{3.10}$$

with

$$C_{i,j} = \left(A_{i,j} - \left(\frac{\alpha}{hJ^2}\right)_{i,j} \frac{h_{i+1,j} - h_{i-1,j}}{2\Delta\varepsilon} + \left(\frac{\beta}{hJ^2}\right)_{i,j} \frac{h_{i,j+1} - h_{i,j-1}}{2\Delta\eta}\right) \tag{3.11}$$

$$D_{i,j} = \left(B_{i,j} - \left(\frac{\gamma}{hJ^2}\right)_{i,j} \frac{h_{i,j+1} - h_{i,j-1}}{2\Delta\eta} + \left(\frac{\beta}{hJ^2}\right)_{i,j} \frac{h_{i+1,j} - h_{i-1,j}}{2\Delta\varepsilon}\right) \tag{3.12}$$

and

$$A_{i,j} = \frac{1}{J_{i,j}} \left[\frac{\left(\frac{\alpha}{J}\right)_{i+1,j} - \left(\frac{\alpha}{J}\right)_{i-1,j}}{2\Delta\varepsilon} - \frac{\left(\frac{\beta}{J}\right)_{i,j+1} - \left(\frac{\beta}{J}\right)_{i,j-1}}{2\Delta\eta}\right] \tag{3.13}$$

$$B_{i,j} = \frac{1}{J_{i,j}} \left[\frac{\left(\frac{\gamma}{J}\right)_{i,j+1} - \left(\frac{\gamma}{J}\right)_{i,j-1}}{2\Delta\eta} - \frac{\left(\frac{\beta}{J}\right)_{i+1,j} - \left(\frac{\beta}{J}\right)_{i-1,j}}{2\Delta\varepsilon}\right] \tag{3.14}$$

3.2.2.2 Discretization of the vorticity equation

The equation (2.61) of transport of vorticity can be rewritten as:

$$\frac{\partial\omega}{\partial t} = \mathcal{F}(\omega) + \mathcal{C}(U_h) \tag{3.15}$$

where $\mathcal{F}$ is a spatial discretization operator that incorporates all of the right hand side terms of equation (2.61) but the friction $\mathcal{C}$. $\mathcal{C}$ and $\mathcal{F}$ are defined as:

$$\mathcal{F} = -U_h^{\varepsilon}\frac{\partial(\omega+2\Omega)}{\partial\varepsilon} - U_h^{\eta}\frac{\partial(\omega+2\Omega)}{\partial\eta} + \frac{\omega+2\Omega}{h}\left(U_h^{\varepsilon}\frac{\partial h}{\partial\varepsilon} + U_h^{\eta}\frac{\partial h}{\partial\eta}\right) + \nu_H\left[\frac{\alpha}{J^2}\frac{\partial^2\omega}{\partial\varepsilon^2} + \frac{\gamma}{J^2}\frac{\partial^2\omega}{\partial\eta^2} - \frac{2\beta}{J^2}\frac{\partial^2\omega}{\partial\varepsilon\partial\eta} + A\frac{\partial\omega}{\partial\varepsilon} + B\frac{\partial\omega}{\partial\eta}\right] \tag{3.16}$$

$$\mathcal{C}(U_h) = -\frac{C_D^{bottom}}{J}\left[\frac{\partial}{\partial\varepsilon}\left(\beta\frac{|U_h|}{h}U_h^{\varepsilon} + \alpha\frac{|U_h|}{h}U_h^{\eta}\right) - \frac{\partial}{\partial\eta}\left(\gamma\frac{|U_h|}{h}U_h^{\varepsilon} + \beta\frac{|U_h|}{h}U_h^{\eta}\right)\right] \tag{3.17}$$

Many authors describe the various temporal schemes that can be used to integrate transport equations (forward Euler, backward Euler, Crank-Nicolson, A.D.I. [1], Adams-Bashforth) [44, 45]. Among them, the choice of Crank-Nicolson scheme is adopted because the finite difference approximation of the time derivative is of second order and it is an implicit and stable method. This choice can be computationally expensive in two-dimensional domains, but the parallelization of the algorithm is expected to compensate this drawback.

The time evolution is divided into a set of discrete time steps, each of size Δt. The solution algorithm marches forward in time, computing a solution at each time step. Temporal discretization involves the integration of every term in the differential equations over the time step Δt. Then the Crank-Nicolson temporal scheme can be shortly described by:

$$\frac{\omega_{i,j}^{n+1} - \omega_{i,j}^{n}}{\Delta t} = \frac{1}{2}\left(\mathcal{F}_{i,j}^{n+1} + \mathcal{F}_{i,j}^{n}\right) + \mathcal{C}_{i,j}^{n} + o(\Delta t^2, \Delta\varepsilon^2, \Delta\eta^2) \tag{3.18}$$

where ω^n refers to the value of vorticity at time t, and ω^{n+1} at time $t+\Delta t$, and where $\mathcal{F}^n$ refers to $\mathcal{F}(\omega^n)$.

Using an intermediate vorticity $\omega_{i,j}^{*}$, one can write similarly:

$$\frac{\omega_{i,j}^{*} - \omega_{i,j}^{n}}{\Delta t} = \frac{1}{2}\left(\mathcal{F}_{i,j}^{*} + \mathcal{F}_{i,j}^{n}\right) + \mathcal{C}_{i,j}^{n} + o(\Delta t^2, \Delta\varepsilon^2, \Delta\eta^2) \tag{3.19}$$

[1] *Alternating Direction Implicit*

3.2.2.3 Solvers and convergence criteria

Finite difference equations (3.10) and (3.18) have been obtained by replacing the exact partial derivatives of the partial differential equations by finite difference approximations of second-order accuracy. The solution of the partial differential equation is obtained by solving the finite difference equations at every point of the domain and at every time step. Iterative methods are known to be the simpliest, and easiest to apply, for solving such large system of equations.
In this particular case a successive over relaxation (SOR) method was implemented to solve the streamfunction in Poisson equation (3.10). For each simulation the optimal over relaxation factor λ_ψ was found by trial and error ($1 \leq \lambda_\psi < 2$) accelerating the resolution up to 10x. The SOR method, applied to the finite difference approximation of the Poisson equation (3.10), is written in the following way:

$$\psi_{ij}^{(k+1)} = \lambda_\psi \mathcal{R}_\psi{}_{ij}^{(k+1)} + (1-\lambda_\psi)\psi_{i,j}^{(k)} \tag{3.20}$$

where the superscript (k) denotes the previous iteration number and $(k+1)$ the current iteration number. $\mathcal{R}_\psi{}^{(k+1)}$ is usually called the residual function. It is function of the current values (at $k+1$) of $(\psi_{i-1,j}, \psi_{i-1,j-1}, \psi_{i,j-1}, \psi_{i+1,j-1})$ and the previous iteration (k) values of $(\psi_{i+1,j}, \psi_{i+1,j+1}, \psi_{i,j+1}, \psi_{i-1,j+1})$. This way, the most recent values of every ψ_{ij} are used in all the calculations.

The Gauss-Seidel method, which is a limiting case of the SOR method when the over-relaxation factor $\lambda_\omega = 1$, is employed to solve the transport of vorticity equation (3.18). In this case the residual is expressed in function of $(\Delta t, \omega^n, \mathcal{C}^n, \omega^*)$ and λ_ω is also function of Δt.

The iterative procedures approach the exact solution as the number of iterations increases. As a measure of the convergence, three error parameters were monitored. Erturk and Dursun in [46] solved very similar equations with the same SOR method, and so the same error parameters are used here:
As in the limit the residual of the equations would be zero, the first error parameter $ERR1$ is simply defined as the maximum absolute residual of the finite differences equations. The convergence is considered achieved when the magnitude of $ERR1$ is less than 10^{-9} to ensure the accuracy of the solution.
The second monitored error parameter $ERR2$ is the maximum absolute difference

in the streamfunction, and in vorticity, between two iterations. It is given by:

$$ERR2_{\psi} = \max\left(abs\left(\psi_{(i,j)}^{(k+1)} - \psi_{(i,j)}^{(k)}\right)\right) \tag{3.21}$$

$$ERR2_{\omega} = \max\left(abs\left(\omega_{(i,j)}^{(k+1)} - \omega_{(i,j)}^{(k)}\right)\right) \tag{3.22}$$

$ERR2$ gives an indication of the significant digit of the variable changing between two iterations.
The third error parameter $ERR3$ corresponds to $ERR2$ but normalized by the value of the variable at the previous iteration:

$$ERR3_{\psi} = \max\left(abs\left(\frac{\psi_{(i,j)}^{(k+1)} - \psi_{(i,j)}^{(k)}}{\psi_{(i,j)}^{(k)}}\right)\right) \tag{3.23}$$

$$ERR3_{\omega} = \max\left(abs\left(\frac{\omega_{(i,j)}^{(k+1)} - \omega_{(i,j)}^{(k)}}{\omega_{(i,j)}^{(k)}}\right)\right) \tag{3.24}$$

It represents the maximum percent change in streamfunction and vorticity at each iteration.

Concerning the degree to which the solution of the coupled equations (2.56) and (2.61) has reached the steady state of the flow, three more similar parameters are monitored: $ERR4_{steady}, ERR5_{steady}, ERR6_{steady}$.

$$ERR4_{steady} = \max\left(abs\left(\omega_{(i,j)}^{n+1} - \omega_{(i,j)}^{n}\right)\right) \tag{3.25}$$

$$ERR5_{steady} = \max\left(abs\left(\frac{\omega_{(i,j)}^{n} - \omega_{(i,j)}^{n}}{\omega_{(i,j)}^{n}}\right)\right) \tag{3.26}$$

$$ERR6_{steady} = \frac{\sum_{n_i,n_j} abs\left(\omega_{(i,j)}^{n+1} - \omega_{(i,j)}^{n}\right)}{n_i n_j} \tag{3.27}$$

$ERR4_{steady}$ is an indication of the significant digit of the maximum vorticity value changing between two time steps. Tipically, the steady state is attained when $ERR4_{steady} < 10^{-6}$. $ERR5_{steady}$ is like $ERR4_{steady}$ normalized by the value of the vorticity at the previous time step. It represents the maximum percent change in vorticity between two time steps. $ERR6_{steady}$ is like $ERR4_{steady}$ averaged over the whole domain.

3.2.3 Solving the equation for oil slick drifting and spreading

The computer code SIMOIL, which models the temporal and spatial evolution of large marine oil spills spreading under gravity-viscosity regime, is based on the equation (1.2) governing the evolution of the oil thickness h recalled here:

$$\frac{\partial h}{\partial t} + \vec{\nabla} \cdot (h\vec{U}) - C\nabla^2 h^3 = 0 \tag{3.28}$$

Where $\vec{U} = \vec{U_h} + 0.03\vec{W}$ is the sum of the contribution of the depth averaged currents and the wind velocity, and C is a diffusion-like coefficient (see its definition in equation (1.3)).
In generalised coordinates equation (3.28) reads:

$$\frac{\partial h}{\partial t} + \frac{1}{J}\left(\frac{\partial JhU^{\varepsilon}}{\partial \varepsilon} + \frac{\partial JhU^{\eta}}{\partial \eta}\right) = C\left[\frac{\alpha}{J^2}\frac{\partial^2 h^3}{\partial \varepsilon^2} + \frac{\gamma}{J^2}\frac{\partial^2 h^3}{\partial \eta^2} - \frac{2\beta}{J^2}\frac{\partial^2 h^3}{\partial \varepsilon \partial \eta} + A\frac{\partial h^3}{\partial \varepsilon} + B\frac{\partial h^3}{\partial \eta}\right] \tag{3.29}$$

with functions A and B defined by:

$$A = \frac{1}{J}\left[\frac{\partial}{\partial \varepsilon}\left(\frac{\alpha}{J}\right) - \frac{\partial}{\partial \eta}\left(\frac{\beta}{J}\right)\right] \tag{3.30}$$

$$B = \frac{1}{J}\left[\frac{\partial}{\partial \eta}\left(\frac{\gamma}{J}\right) - \frac{\partial}{\partial \varepsilon}\left(\frac{\beta}{J}\right)\right] \tag{3.31}$$

3.2.3.1 Convective and diffusive-like terms

For simplicity, the equation (3.28) can be written:

$$\frac{\partial h}{\partial t} = f(t, h(t)) = -convec(t, h(t)) + diff(t, h(t)) \tag{3.32}$$

The dicretization of the convective terms is upgraded since the previous version of SIMOIL described in [11], from a first order accurate upwind scheme to a second order upwind scheme (except near the boundary where the first order upwind scheme is maintained).

Defining

$$P_\varepsilon = JhU^\varepsilon \quad ; \quad P_\eta = JhU^\eta \tag{3.33}$$

$$\begin{array}{rrrrrr} \text{if} & P_\varepsilon \geq 0 & \text{then} & a^+ = 1 & \text{and} & a^- = 0 \\ & \text{if not} & \text{then} & a^+ = 0 & \text{and} & a^- = 1 \\ & & & & & \text{and} \\ \text{if} & P_\eta \geq 0 & \text{then} & b^+ = 1 & \text{and} & b^- = 0 \\ & \text{if not} & \text{then} & b^+ = 0 & \text{and} & b^- = 1 \end{array}$$

Then the convective terms of equation (3.29), denoted as $convec(i,j)$ is discretized as:

$$\begin{aligned} convec(i,j) = \frac{1}{2\Delta J}[&a^+(3P_\varepsilon(i,j) - 4P_\varepsilon(i-1,j) + P_\varepsilon(i-2,j)) + \\ &a^-(-P_\varepsilon(i+2,j) + 4P_\varepsilon(i+1,j) - 3P_\varepsilon(i,j)) + \\ &b^+(3P_\eta(i,j) - 4P_\eta(i,j-1) + P_\eta(i,j-2)) + \\ &b^-(-P_\eta(i,j+2) + 4P_\eta(i,j+1) - 3P_\eta(i,j))] \end{aligned} \tag{3.34}$$

The diffusive-like term is discretized by means of second order centred differences as in the previous version of the code. Denoted $diff(i,j)$, it reads:

$$\begin{aligned} diff(i,j) = C(\quad & \left(\frac{\alpha}{J^2}\right)_{i,j} \frac{h^3_{i+1,j} - 2h^3_{i,j} + h^3_{i-1,j}}{\Delta\varepsilon^2} \\ & + \left(\frac{\gamma}{J^2}\right)_{i,j} \frac{h^3_{i,j+1} - 2h^3_{i,j} + h^3_{i,j-1}}{\Delta\eta^2} \\ & - \left(\frac{2\beta}{J^2}\right)_{i,j} \frac{h^3_{i+1,j+1} - h^3_{i+1,j-1} - h^3_{i-1,j+1} + h^3_{i-1,j-1}}{4\Delta\varepsilon\Delta\eta} \\ & + A_{i,j} \frac{h^3_{i+1,j} - h^3_{i-1,j}}{2\Delta\varepsilon} \\ & + B_{i,j} \frac{h^3_{i,j+1} - h^3_{i,j-1}}{2\Delta\eta}) \end{aligned} \tag{3.35}$$

3.2.3.2 Time advancement

To solve the initial value problem posed equation (3.28), a classical fourth order explicit Runge-Kutta method is used. Though it is an explicit method requiring small time steps, it is interesting because it is very accurate, stable and easy to implement.
The time integration is made of four consecutive intermediate steps denoted with $(^*)$ to end up with the new value of thickness h^{n+1} one time step later:

$$h^*_{n+1/2} = h^n + \frac{\Delta t}{2} f(t_n, h^n), \tag{3.36}$$

$$h^{**}_{n+1/2} = h^n + \frac{\Delta t}{2} f(t_{n+1/2}, h^*_{n+1/2}), \tag{3.37}$$

$$h^*_{n+1} = h^n + \Delta t\, f(t_{n+1/2}, h^{**}_{n+1/2}), \tag{3.38}$$

$$h^{n+1} = h^n + \frac{\Delta t}{6}[f(t_n, h^n) + 2f(t_{n+1/2}, h^*_{n+1/2}) + 2f(t_{n+1/2}, h^{**}_{n+1/2}) + f(t_{n+1}, h^*_{n+1})] \tag{3.39}$$

3.3 Parallel computing

The centred finite differences schemes and the iterative procedures require a high number of cells and calculations to ensure the accuracy and the stability of the solution of the equations. This makes this code demanding in CPU usage. Parallel computing is a solution that, by splitting the computational work between several processors working simultaneously, allows to complete a task faster than computing the same task sequentially. There are roughly two categories of parallel computers depending on how the CPU access the memory:

- *Shared memory computers* are made of at least two processors connected to one another through the same memory module. The shared memory is used to exchange information between processors.

- *Distributed memory computers* are made of at least two processors, each one with is own private memory. To exchange information, processors have to pass messages to one another through a communication network.

Open MP directives are used to implement parallel programming to solve the hydrodynamic equations in shared memory computers. Only the part of the code

corresponding to iterative solvers mentioned earlier have been parallelized by splitting the computational domain into two sub-domains with approximately the same number of nodes. Then the work load is shared almost equally (in the optimal configuration) between two processors allowing to speed up the resolution of the equations. The speed up factor can vary strongly depending on the computer system used, on the choice of compiler, and of course, on the complexity of the flow to solve (as it may be difficult to achieve a good load balance).

Part II

RESULTS OF NUMERICAL SIMULATIONS

The code developed and used in this work to solve numerically the equations (2.56) and (2.61) governing shallow turbulent and rotating coastal oceanic flows, is written in FORTRAN 90. The reliability of the computation results lays on a continuous and iterative process of verification and validation of the solutions against experimental and numerical studies published in the literature. In practice, the code veracity and validity stand on the accumulation of proofs that it works properly.

Verification assessment determines if the programming and mathematics are correct by comparing simulation with accurate numerical and experimental results. Validation assessment determines if the model can represent physical phenomena comparing simulation with observations and validated models.

In chapter 4, the numerical techniques are verified by comparing the code solutions with several reference authors of computational physics, fluid mechanics and numerical methods, in classical two-dimensional flow problems. By adding gradual complexity to the flow, those cases allow to check the correct implementation of the solvers, to detect programming errors, and to validate the model in simple configurations. Then the shallow ocean model is tested against a referenced case where bathymetry, Coriolis effect, eddy viscosity and seabed friction have a significant impact on the hydrodynamics. All these simulations are presented to show that the model and the code are suitable for coastal flow studies.

Finally, in chapter 5, the code is applied to simulate two physical cases:

1. a hypothetical oil spill in the area of Tarragona harbour. This configuration allows to validate the results with the previous version of SIMOIL by Cuesta et al. [11] ;

2. a recent oil spill occurred during the 2006 Lebanon war. The hydrodynamic model is coupled to the upgraded oil slick model SIMOIL to perform hindcast simulation of this major Mediterranean oil spill. The system is validated against observations and reference simulations of the Mediterranean Operational Ocean Network. The potential flow version of SIMOIL is also run in order to evaluate the improvement accomplished developing this generalised shallow water model.

Test-cases and methods are summed up in table 3.1.

	Cartesian Mesh	Orthogonal Non-Regular Mesh	Non-Orthogonal Regular Mesh	Wall Boundary Conditions	Open Boundary Conditions	Integration over Depth	Coriolis Force	Seabed Friction	Serial Code	Parallel Code	Coupled Oil Transport
Square Cavity	✓			✓					✓	✓	
Arc Shaped Cavity		✓		✓					✓	✓	
Skewed Cavity			✓	✓					✓	✓	
Backward Facing Step	✓	✓	✓	✓	✓				✓	✓	
Plane Wall Jet	✓			✓	✓				✓	✓	
Interaction Vortex Steep Slope	✓			✓		✓	✓		✓	✓	
Salou			✓	✓	✓	✓	✓	✓	✓	✓	✓
Lebanon War 2006			✓	✓	✓	✓	✓	✓	✓	✓	✓

Table 3.1: Table of test-cases, methods and model runs used during the verification and validation process.

Chapter 4

Verification of the Code on Benchmark Cases

4.1 Enclosed flows : lid-driven cavities

4.1.1 Interest and description of cavity flows studies

The laminar incompressible flow in driven cavities is a very classical and standard problem to test numerical methods in CFD literature. This study refers to numerical and experimental works published by Ghia et al. [47], Fuchs et al. [48] and Erturk et al. [46]. Each article focuses on a different cavity shape and a range of Reynolds number is evaluated. Every flow field is characterized by streamlines patterns and velocity profiles along lines passing through the center of the cavities.

The three simple, and easy to program, geometries introduced here and sketched in figure 4.1, provide an ideal benchmark to evaluate the correct implementation of the code and to verify the accuracy of the numerical techniques. In each case the top boundary is moving at a constant pace entraining the fluid by viscosity. As a result, a main vortex forms in the center of the domain. Secondary counter rotating vortices may form at the lowest corners, which intensity and position vary in function of the Reynolds number defined by the velocity of the leading wall. As can be seen in figure 4.1, for the square cavity problem a natural cartesian grid is used to mesh the domain. This mesh is regular and orthogonal. For the polar cavity, a boundary conforming, orthogonal and non-regular grid is used. Finally, for the skewed cavity, also a boundary-fitted, regular but in this case non-orthogonal grid is tested. These

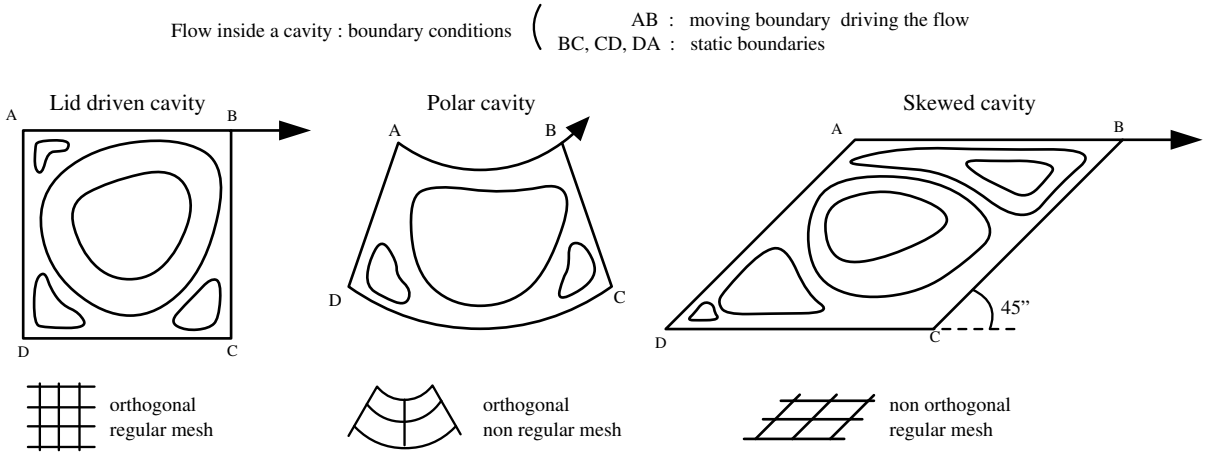

Figure 4.1: Schematic view of the 3 cavities

different mesh configurations allow us to ensure that the generalised equations, the geometry coefficients and the wall boundary conditions are correctly resolved and evaluated by the code.

4.1.2 Numerical results and discussion

4.1.2.1 The square cavity

The objective is to verify the quality of the numerical solution of the code in cartesian coordinates. This test allows also to verify the consistency of the wall boundary conditions described previously in 2.2.3.5. Simulations have been realized for Re=100, 1000 and 3200, over 2 different meshes (129x129 nodes and 257x257 nodes), although only the results at Re=3200 for the thinner mesh (257x257) are presented.

The study is realized on a square cavity of side size equal to 1 meter. Wall boundary conditions (no flow through and along the wall) are applied at the boundaries of the cavity. The top wall (AB in figure 4.1) is in constant motion at velocity 1 ms^{-1}. The kinematic fluid viscosity is choosed such as the Reynolds number based on the leading velocity and the side size of the cavity is equal to 3200.

Coriolis coefficient 2Ω is set to 0, as well as the seabed friction coefficient C_D^{bottom}. The depth dependency is eliminated by setting a uniform and constant depth h equal to 1. The grid resolution with 257x257 nodes is found to be adequate to resolve the boundary layer at Re=3200.

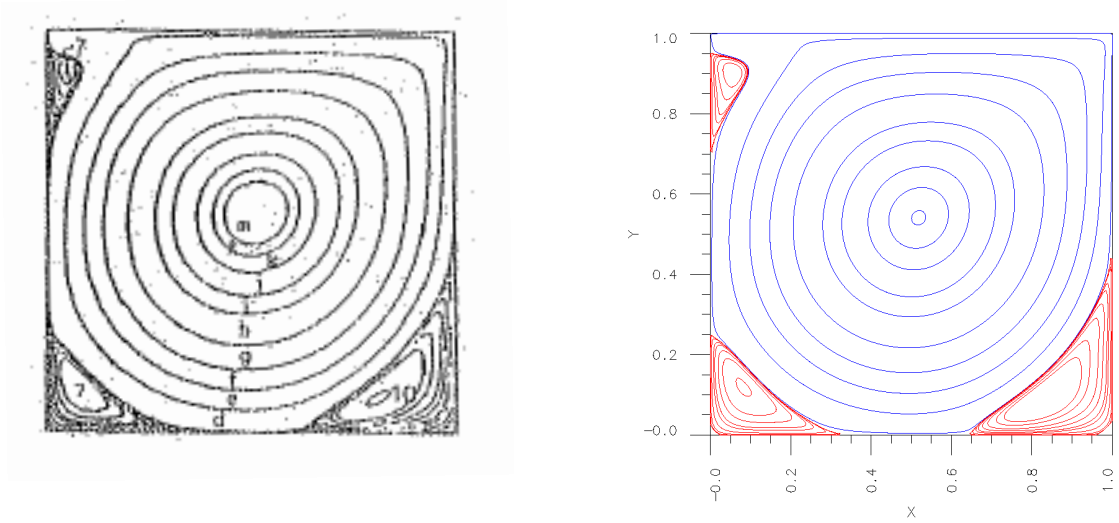

(a) Ghia Re=3200 Cartesian grid 129x129 [47] (b) Present work Re=3200 Cartesian grid 257x257

Figure 4.2: Streamline pattern for vortices in the square cavity at Re=3200

Streamline contours for the cavity flow at $Re = 3200$ are shown in figure 4.2. The negative values of ψ, in blue, are taken in the range $[-0.1175, -10^{-4}]$. They show how the primary vortex occupies the main part of the cavity. The positive values of ψ, in red, are taken in the range $[10^{-8}, 3.10^{-3}]$. They show the ubication of 3 secondary eddies in the lowest corners and near the upper left corner.

Figures 4.3 and 4.4 show the velocity profiles computed by Ghia [47](•) and by the present code (—) for $U(y)$ (horizontal component of the velocity) along a vertical line passing through the center of the cavity at $x = 0.5$, and for $V(x)$ (vertical component of the velocity) along a horizontal line passing through the center of the cavity at $y = 0.5$.

Both solutions agree very well, indicating that the present code solves adequately the square cavity flow, up to Re=3200, on a cartesian mesh fine enough to resolve the boundary layer. No accuracy is lost in the computation of the Helmholtz variables, the geometry coefficients or in the approximation of the boundary conditions that would make the solution unstable or wrong.

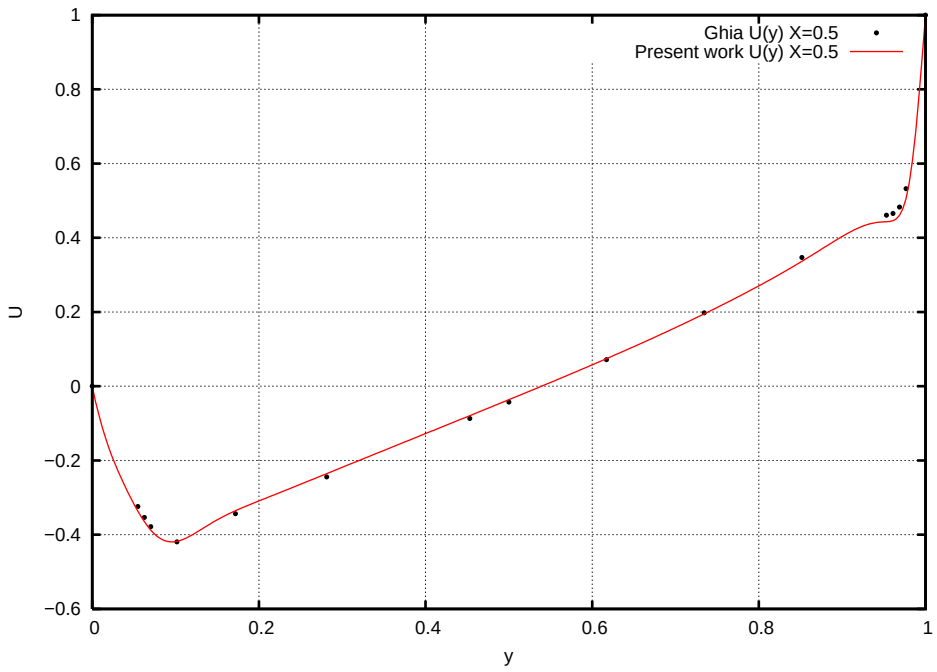

Figure 4.3: Comparison of $U(y)$ velocity along a vertical line through the center of the cavity at x=0.5

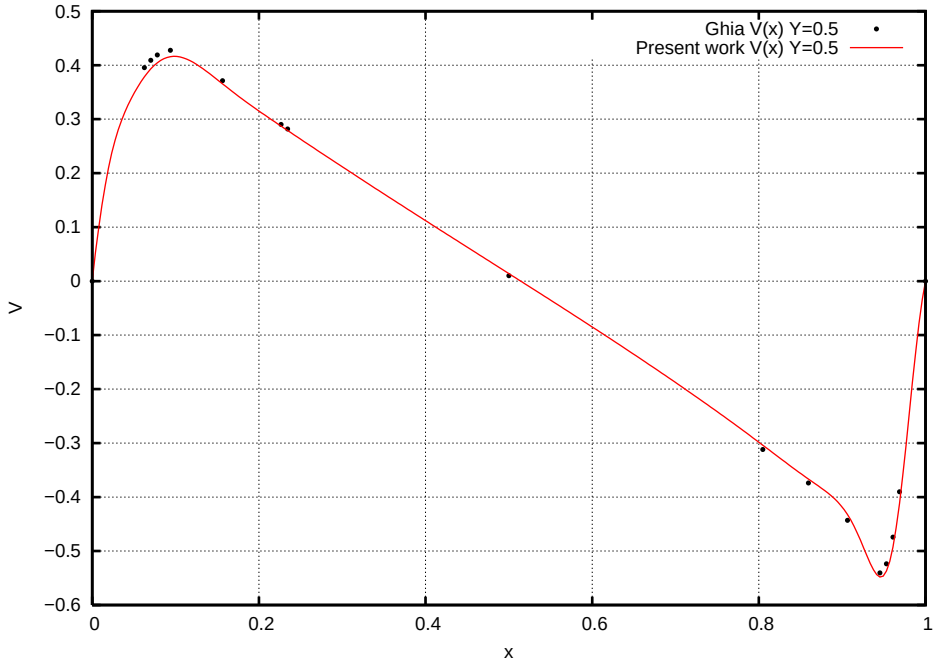

Figure 4.4: Comparison of $V(x)$ velocity along a horizontal line through the center of the cavity at y=0.5

4.1.2.2 The polar cavity

The objective of this benchmark case is to verify the quality of the numerical solution of the code in generalised coordinates that are orthogonal but non regular. This test also checks the consistency of the wall boundary conditions described previously in 2.2.3.5. Simulations have been realized for Re=60 and 350 over different meshes (81x81 nodes and 129x129 nodes), although only the results at Re=350 for the thinner mesh (129x129) are presented.

The study is realized on a cylindrical cavity characterized by an opening angle of 1 radian, a rotating inner radius $R_1 = 0.0475m$ and a fixed outer radius $R_2 = 0.095m$ like in Fuchs and Tillmark [48] experiments. Wall boundary conditions (no flow through and along the wall) are applied at the boundaries of the cavity. The top wall (inner radius AB in figure 4.1) is in motion at constant angular velocity $U_\theta = 1ms^{-1}$. The kinematic fluid viscosity is again choosed such as the Reynolds number based on the angular velocity and the inner radius of the cavity is equal to 350.

Coriolis coefficient 2Ω is set to 0, as well as the seabed friction coefficient C_D^{bottom}. The depth dependency is eliminated by setting a uniform and constant depth h equal to 1. The grid resolution with 129x129 nodes is found to be adequate to resolve the boundary layer at Re=350.

Streamline contours for the cavity flow at $Re = 350$ are shown in figure 4.5(a). The mesh appears as a grey canvas. The negative values of ψ, in blue, are taken in the range $[-10^{-6}, -10^{-3}]$. They show how the primary vortex occupies the main part of the cavity. The positive values of ψ, in red, are taken in the range $[10^{-8}, 3.10^{-3}]$. They show the ubication of 2 secondary eddies in the lowest corners. The experiments by Fuchs and Tillmark provided both qualitative and quantitative results. They visualized the flow field by seeding heavily the fluid with Al_2O_3 and illuminating laterally the cavity with a laser sheet. Figure 4.5(b) shows a picture taken of this flow for Re=350. The numerically computed streamlines for Re=350 shown in figure 4.5(a) are in very good agreement with this qualitative information.

Fuchs and Tillmark also measured, by using laser Doppler anemometry, the velocity components at some sections of the cylindrical cavity and compared them to computed solutions. They found a very good agreement between the results and attributed small differences to three-dimensional effects in the apparatus. The present code is verified by comparing these results to the computed angular and ra-

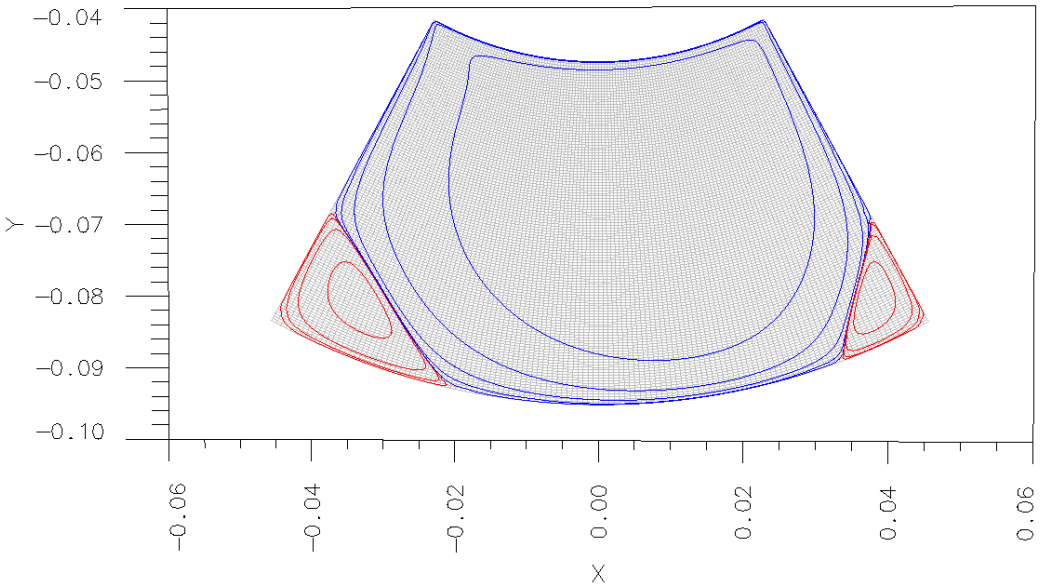

(a) Present work Re=350 Polar grid 129x129

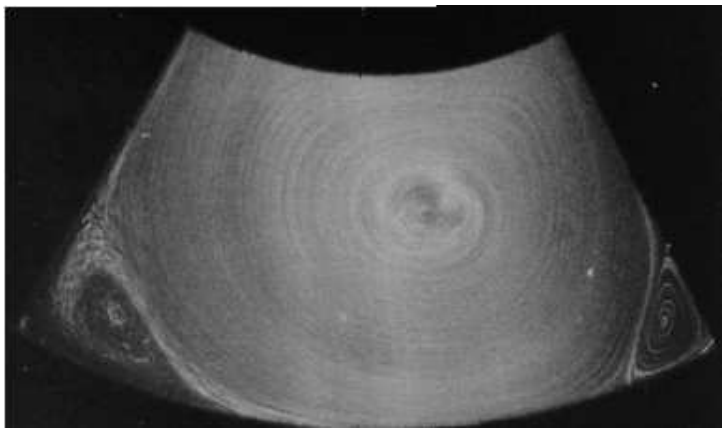

(b) Experimental visualization of the flow in the polar cavity at Re=350 [48]

Figure 4.5: Streamline pattern for vortices in the polar cavity at Re=350

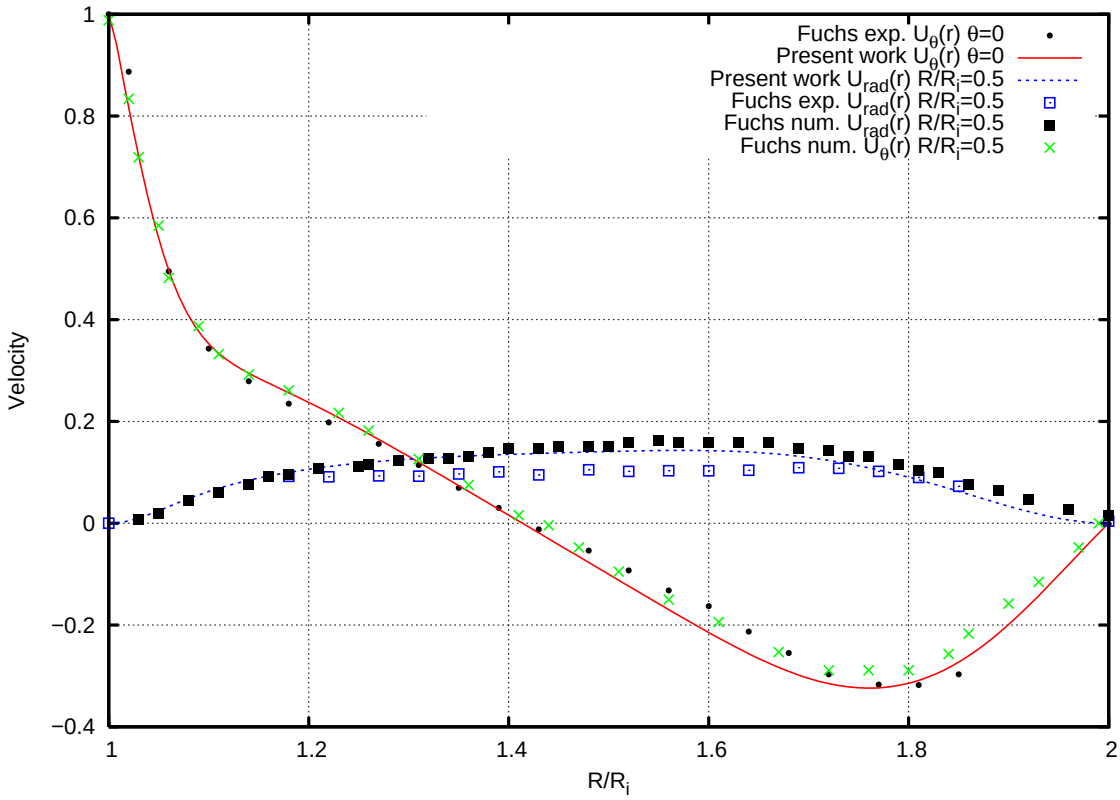

Figure 4.6: Velocity profiles in the polar cavity at Re=350

dial ($U_\theta(r), U_{rad}(r)$) velocity profiles at Re=350 along a radial line passing through the center of the cavity. All these results are compiled in the figure 4.6, the present results being very close to both experimental and computational values from the literature.

4.1.2.3 The skewed cavity

In this case, the objective is to verify the quality of the numerical solution of the code in non-orthogonal, but regular, skewed coordinates. This test also checks the consistency of the wall boundary conditions described previously in 2.2.3.5. Simulations have been realized for a skew angle of 45°, at Re=100 and 1000, over a mesh made of 129x129 nodes. Although only results at Re=1000 are presented here compared to Erturk and Dursun [46] high resolution benchmark which was computed on a 512x512 nodes mesh.

The study is realized on a 45° skewed cavity of side size equal to 1 meter illustrated previously in figure 4.1. Wall boundary conditions (no flow through and along the wall) are applied at the boundaries of the cavity. The top wall is in constant motion at velocity 1 ms^{-1}. The kinematic fluid viscosity is calculated such as the Reynolds number based on the leading velocity and the side size of the cavity is equal to 100 and 1000 respectively.

Coriolis coefficient 2Ω is set to 0, as well as the seabed friction coefficient C_D^{bottom}. The depth dependency is eliminated by setting a uniform and constant depth h equal to 1.

Streamline contours computed in the present study for the 45° skewed cavity flow at $Re = 1000$ are shown in figure 4.7(a). The negative values of ψ, in blue, are taken in the range $[-10^{-3}, -10^{-10}]$. The positive values of ψ, in red, are taken in the range $[10^{-10}, 10^{-3}]$. The streamline patterns found by Erturk and Dursun in [46] for the same flow are given in figure 4.7(b). There is a very good agreement between both solutions : in this geometry the primary vortex is confined at the upper part of the cavity. A secundary vortex occupies the main part of the cavity and at least 3 alternating counter-rotating vortices can be identified between the geometrical center of the cavity and the lower left corner.

In their article [46], Erturk and Dursun solve the skewed cavity flow with a variety of skew angles ranging between 15° and 165° for Re=100 and Re=1000, on a very fine generalised grid. They provide for future researchers detailed tabulated results of velocity profiles along lines passing through the center of the cavity (see the dot lines in figure 4.7(b)). Figures 4.8 and 4.9 compare velocity profiles obtained with the present code against the results tabulated in [46] : the agreement is very good. The reason is probably that both physical model and numerical methods are very similar, and that the 129x129 nodes mesh resolution is fine enough to resolve

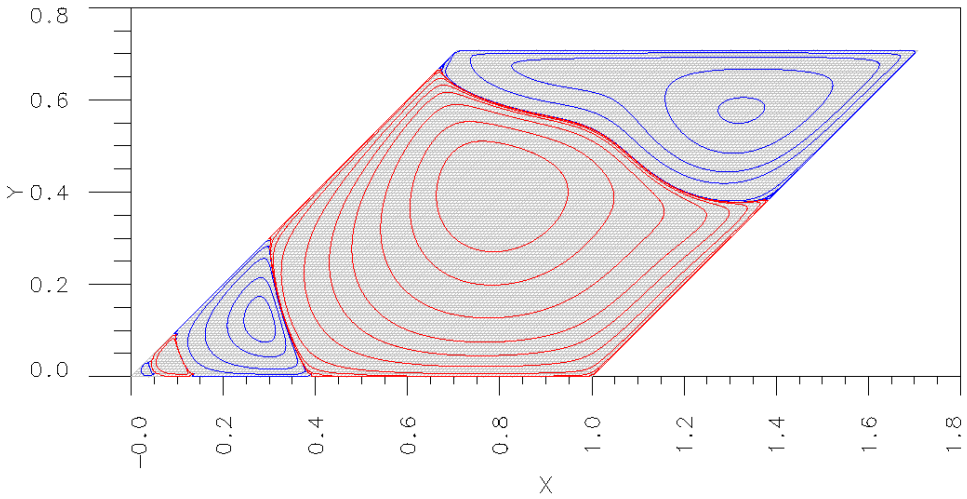

(a) Present work Re=1000 45º skewed grid 129x129

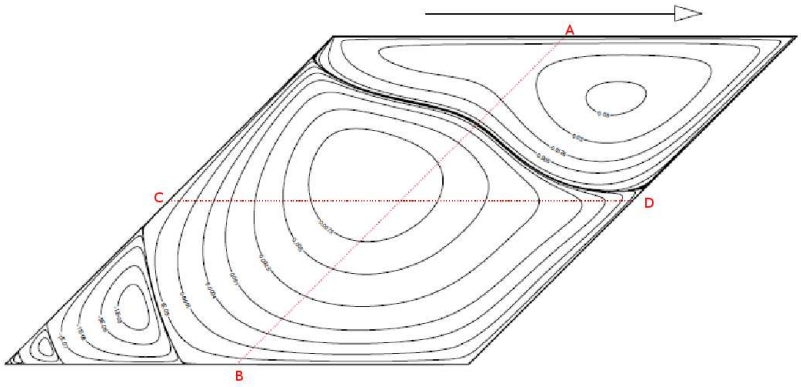

(b) Erturk Re=1000 45º skewed grid 512x512 [46]

Figure 4.7: Streamline pattern for vortices in the 45º skewed cavity at Re=1000

the flow adequately at Re=1000.

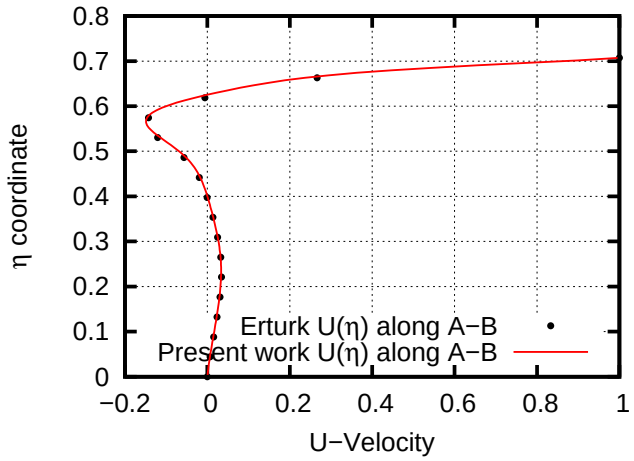

Figure 4.8: Skewed driven cavity at Re=1000, skewness=45º. Comparison of $U(\eta)$ velocity profiles through the center of the cavity along AB.

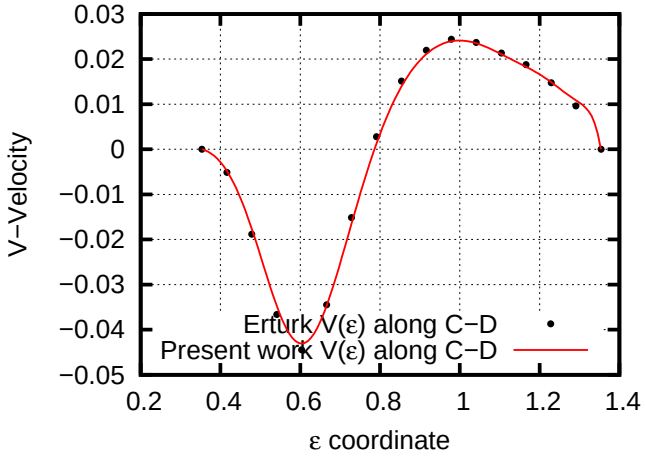

Figure 4.9: Skewed driven cavity at Re=1000, skewness=45º. Comparison of $U(\varepsilon)$ velocity profiles through the center of the cavity along CD.

In this last section the code has been tested against some of the available benchmark problems with cartesian, non-orthogonal and non-regular grids in order to verify the correct implementation and computation of the geometric coefficients associated to equations written in generalised coordinates. The comparison with the literature has been satisfactory.

4.2 Open flows

With the exception of lakes and land-locked seas, numerical simulations of coastal flows always involve at least one boundary condition limiting to the open sea. Across such a non-physical and artificial boundary, complex time-dependent inflow and outflow can occur, which makes it difficult to find a universal method to treat that open boundary. So in practice, if possible, one chooses the location of the artificial boundary in such a way that the physics are simplified. Then several solutions can be implemented, which need to be adapted to each particular case, knowing that a unique, best boundary condition cannot be determined in advance.

The purpose of this section is to verify and validate the methods and the model of open boundary conditions described in 2.2.3.5 that are:

- Forced inflow velocity profile
- Outflow boundary condition
- Entrainment boundary condition

To achieve this goal, the solutions of the laminar flow over a backward facing step and the forced laminar plane wall jet, are computed and compared to numerical and experimental studies in the literature.

4.2.1 Backward facing step

4.2.1.1 Interest and description

The flow over a backward facing step (BFS) is a standard benchmark problem in CFD. The most important charateristics are the sudden expansion and the consequent separation and reattachment of the flow. It has many practical engineering applications, both in internal flow systems like diffusers, combustors and opening channels, and in external flows like flows around airfoils and buildings.

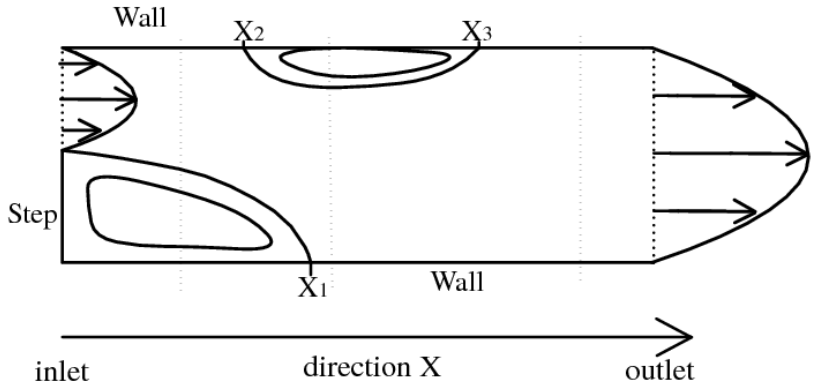

Figure 4.10: Schematic view of the flow over a backward-facing step

A large amount of studies can be found on the topic, both experimental and numerical works, for many configurations : from laminar two-dimensional flow, to turbulent three-dimensional flow, with a wide range expansion ratio, analysed by many different methods. A complete survey of the previous works can be found in Le's dissertation [36] and the more recent Kanna's note [49]. This study refers particularly to the works conducted by Kanna [49] and Borthwick [50] with similar numerical methods, Armaly et al [51] experimental study of the effect of Reynolds number on the reattachment length as reported in Barton's study [52] on the influence of the length of the entrance channel, and also Gartling [53] numerical work on outflow boundary conditions.

A sketch of the BFS flow can be seen in figure 4.10. It consists of a plane channel with a step. At the inlet, a steady parabolic flow is set. It encounters a sudden expansion that causes the flow to separate at the step wall and a recirculation zone appears behind the opening. In a laminar flow, the reattachement length (X_1) increases continuously with Reynolds number and a secondary vortex (measured by X_2 and X_3) may appear at higher Reynolds number at the top wall of the channel.

The objective of this test is to validate the forcing of inlet velocity profile, and the kind of outflow boundary conditions which allows the flow variables to leave the computational domain without perturbing the upstream flow.

4.2.1.2 Results and discussion

The geometry and inlet conditions considered here are the same than Kanna and Gartling [49, 53]. The outlet condition is the same than Kanna. The channel width is $H = 1$, so the step height $h = 0.5$. The channel length is $40h = 20$. The Reynolds number is defined as $Re = \frac{U_{avg}H}{\nu}$. The inlet velocity profile is specified as a parallel flow with a parabolic horizontal component given by $U(y) = 24y(y/2)$ for $0 \leq y \leq 0.5$. This produces a maximum inflow velocity $U_{max} = 1.5$ and an average inflow velocity $U_{avg} = 1$. After a grid independence study at Re=800 (101x11 nodes,201x21 nodes, 201x41 nodes), a cartesian grid (201x21) is found to be suitable for the calculations.oce

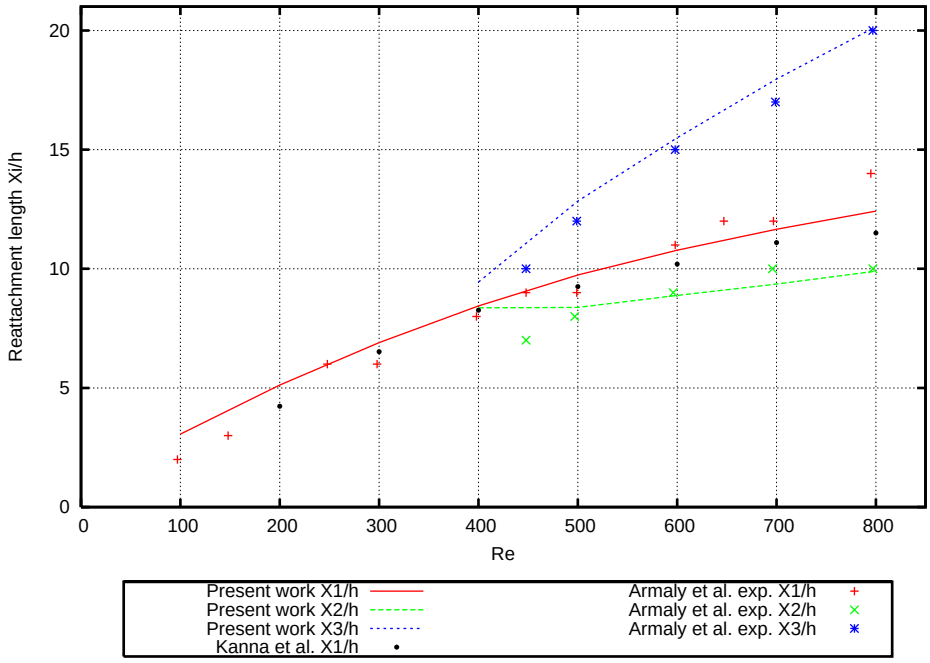

Figure 4.11: Reattachment and separation length with Reynolds number

The simulations are done for Re ranging from 100 to 800. The reattachment length $X1$ is defined by a change of sign of the vorticity on the bottom wall. The upper separation location and size are measured by $X2$ and $X3$. The variation of the reattachment length with Re is given in figure 4.11. The present work agrees well with both the numerical results provided by Kanna and Armaly's experimental results rescaled by Barton [51, 52]. As expected, the reattachment length X_1 increases with Re, but non linearly as the flow is delayed by viscous effects because of the

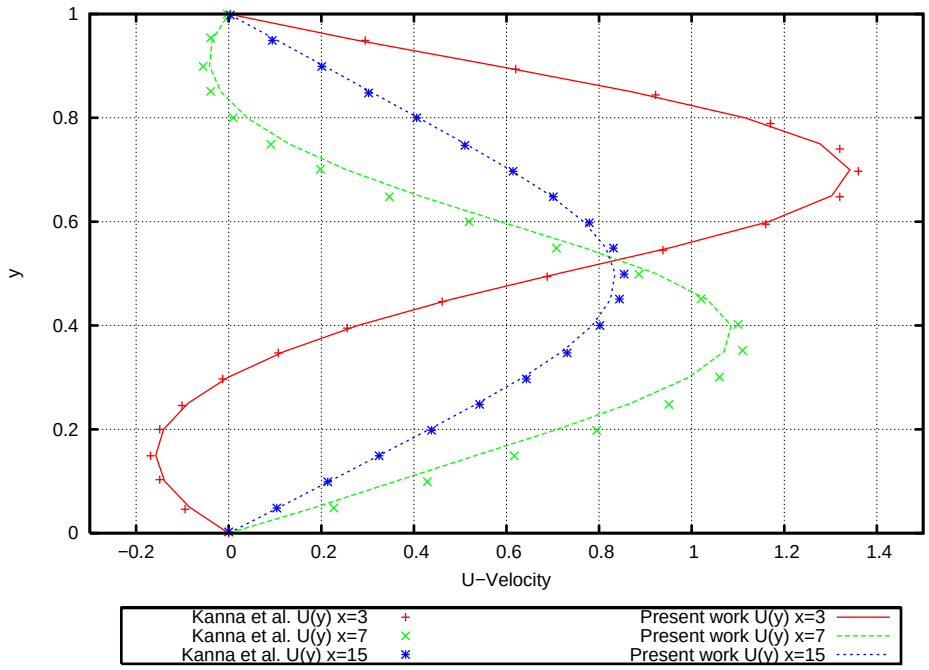

Figure 4.12: Horizontal velocity profiles downstream the step at Re=800 at x=3, x=7 and x=15

upper wall at low Re ($Re \leq 400$), and even more delayed at higher Re because of the upper recirculation region. At low Re, the reattachment length predicted by the computation is higher than the one measured by Armaly. This result is consistent with Barton's observations [52] : at low Re, at the channel entrance, the real flow is influenced by the expansion and the size of the step-side recirculation is significatively smaller than the one computed with a perfect parabolic flow forced over the step. At high Re, there is also a discrepancy between experimental and numerical results that was not solved refining the computational mesh. This deviation can be explained by the three-dimensional experimental effects observed by Armaly for $Re > 400$ which makes difficult the comparison with two-dimensional simulations. In the figure, the variation of X_2 and X_3 with Re shows that the upper recirculation bubble grows and moves downstream as Re increases. This observation was reported previously by Le [36]. Further comparisons are made difficult because of the absence of tabulated values: numerical results pictured here and produced by the other authors have been carefuly extracted from the publications.

At Re=800, horizontal velocity profiles are extracted at 3 downstream locations in $X = 3$, $X = 7$ and $X = 15$. This work results show good agreement when com-

pared with Kanna in figure 4.12. The small differences in the velocity profiles are due to the difference in the reattachment length, lower for Kanna ($X_1/h = 12.42$ in this study and Kanna found $X_1/h = 11.81$) and so the maximum velocity appears to be higher at $X = 3$ and $X = 7$. Further from the separation flows, at $X = 15$, the profiles are getting much closer.

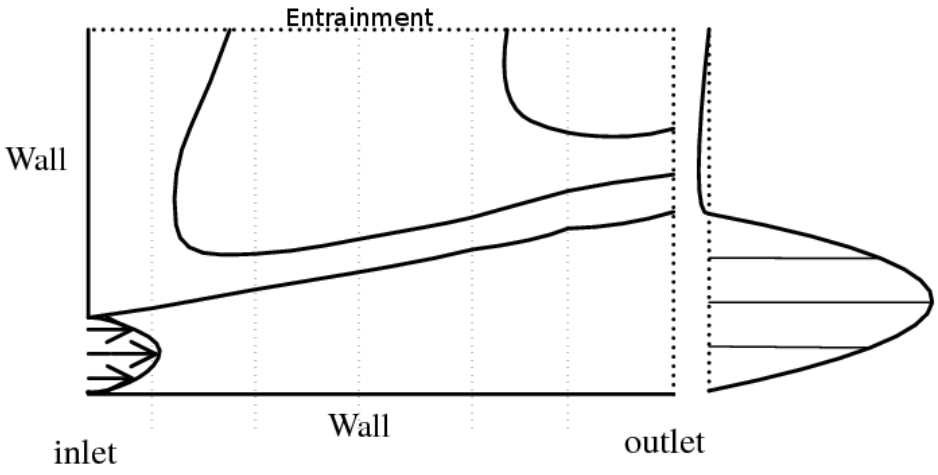

Figure 4.13: Schematic view of the plane wall jet geometry, including the boundary conditions and the velocity profile close to the entrance.

4.2.2 Plane wall jet

4.2.2.1 Interest and description

A wall jet is a thin jet of fluid blown tangentially along a surface. It has important applications in heat and mass transfers for the engineering design of evaporation and cooling technologies, but it also shows a strong similarity with coastal currents where the flow field can be roughly divided into two areas : the inner near-wall region, characterised by the velocity profile of a viscous boundary layer over a flat plate, and the outer free stream region, where after reaching an inflection point, the velocity profile is similar to a free shear layer. The laminar plane wall jet (PWJ) configuration and the typical velocity profile close to the entrance are illustrated in figure 4.13.

How to model the open boundary conditions in the free stream region and at the outlet is challenging for numerical modellers. Kanna and Das [34] reviewed some of the latest studies on the PWJ problem and found a suitable combination of entrainment and exit boundary conditions which has been implemented in this work. The objective of this section is to validate the application of these boundary conditions in this code, by comparing velocity profiles at different downstream locations with the numerical results of Kanna and the experimental results of Quintana et al. [34, 54].

4.2.2.2 Results and discussion

The numerical experiments are carried out at $Re = 300$, with a steady parabolic jet (of width $h = 0.05$) entering the domain from the lower left corner and blowing over a horizontal wall. The dimension of the domain are identical with the experiment described by Kanna in [34]: 30 x h in streamwise direction X and 20 x h normal direction Y. The upper boundary is set as entrainment boundary condition defined in equation (2.2.3.5) and is bounded by a wall at left and an open boundary at the downstream exit of the domain. The calculations are made over a cartesian grid made of 181 x 121 nodes to guarantee enough accuracy all over the domain.

Once the steady state is achieved, the streamlines pattern obtained (figure 4.14(b)) are compared qualitatively with the reference solution (figure 4.14(a)) computed by Kanna in [34]. The two regions of the flow appear clearly. The main flow expands from the lower left corner until it occupies half of the domain at the downstream boundary. Entrainment occurs in the upper part of the domain: the ambient fluid is sucked in inside the domain at the upper boundary and carried away downstream by the main flow. The present code represents well those features.

For a more quantitative analysis of the data, the boundary layer thickness δ is defined as the normal distance where horizontal velocity U is equal to half of the maximum velocity U_m. Then, the similarity variable μ is defined as y/δ. Finally, the similarity profiles at different downstream locations shown in figure 4.15 allow to compare the present work with Kanna numerical results and Quintana experimental measurements [34, 54]. A good agreement is noticed with the benchmark results.

In figure 4.15(a), at $X = 3h$, the similarity profile shows a small negative region. Further downstream, in figures 4.15(b), 4.15(c), 4.15(d), the jet is expanded and the negative region disappears. A slight deviation can be observed from the reference results that could be explained mainly by a difference in the grid resolution.

4.3 Conclusion

A protocol of verification of the code has been established consisting in running a serie of benchmark simulations.

The first part of this methodology concerns laminar two-dimensional flows and focuses on the verification of the solver and the boundary conditions of the generalised coordinates vorticity-streamfunction formulation of the Navier-Stokes equa-

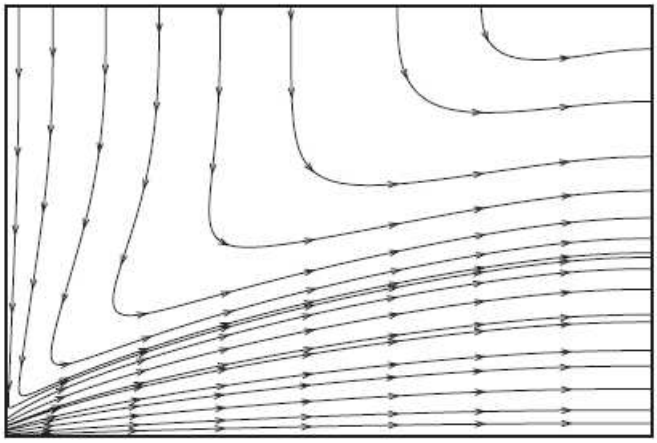

(a) Kanna, clustered grid 81x81 [34]

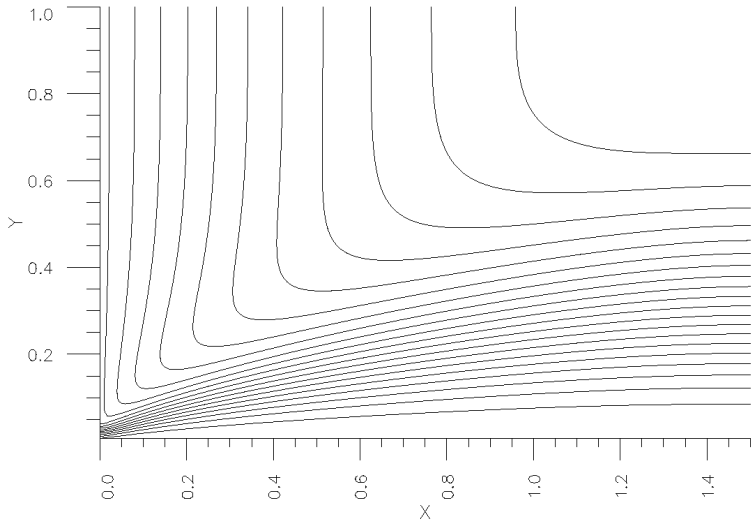

(b) Present work, cartesian grid 181x121

Figure 4.14: Streamline pattern for the laminar plane wall jet at $Re = 300$

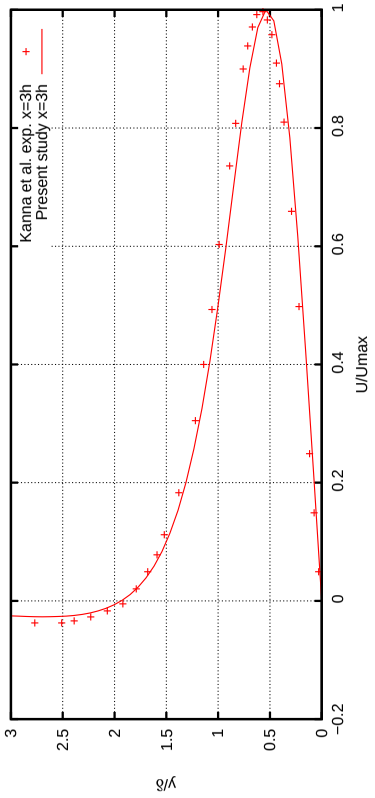

(a) X=3h

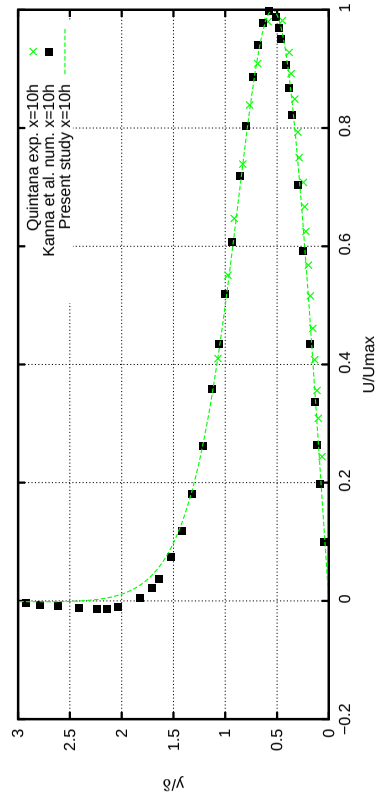

(b) X=10h

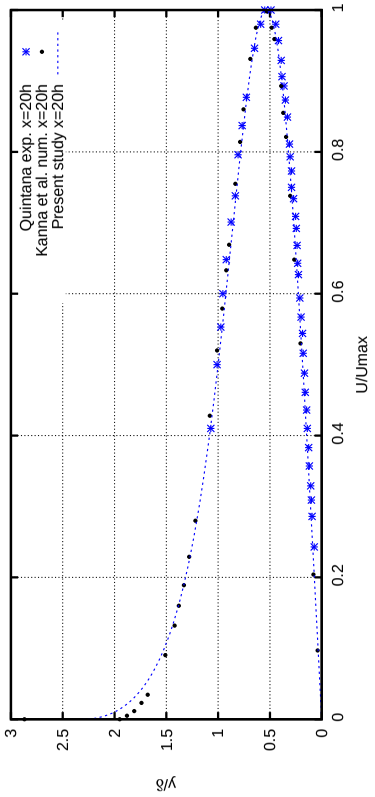

(c) X=20h

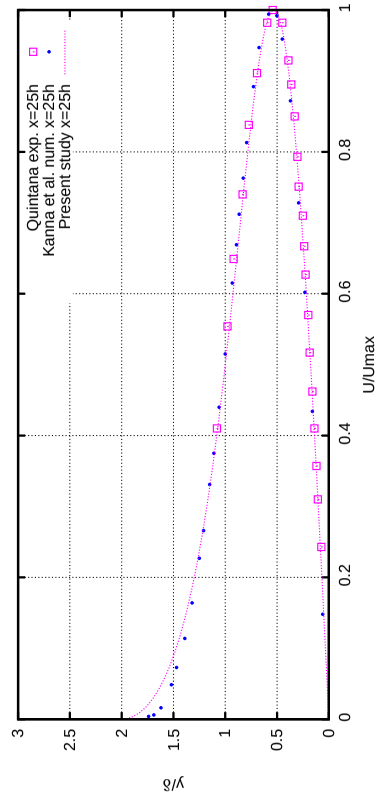

(d) X=25h

Figure 4.15: Comparison of similarity profiles at different downstream locations

tions.

The second part of the protocol concerns the validation of the shallow coastal ocean model which is the subject of the next section of this chapter. It validates the ability of the model to reproduce accurately observed and measured oceanic phenomena involving interaction of currents with bathymetry and varying environmental parameters.

At every stage of the development of the computer code, the process has been completeded successfully in order to ensure the quality, accuracy and reliability of the numerical predictions.

Coastal oceanic currents are deeply influenced by changes of bathymetry, planetary rotational effects and seabed friction (cf. chapter 2). Since the numerical methods and the model of boundary conditions have been verified and validated for the case of purely two-dimensional flows, it is now possible to carry out the validation of the model for depth-integrated rotating flows.

A case study by Zavala Sansón and van Heijst [55], presenting qualitative and quantitative observations and analysis of such flow has been selected in order to compare with the solution of the present model. This case deals with the interaction of a vortex with coastal topography. It reveals the basic mechanism involved in the generation of meandering currents after a cyclonic vortex passes over a western slope. A phenomenon very similar to the meandering of the Gulf Stream that can be observed off the south-east coast of the USA. Zavala Sansón and van Heijst experiments were performed in a rectangular rotating tank with a topographic β-plane allowing to reproduce the variation of planetary vorticity with latitude, and the consequent vortex motion was visualized using colored dye and laser velocimetry (see figure 4.16). Later, a numerical simulation was done but this time with oceanic parameters, to show that numerical and experimental results were consistent with real ocean observations. This last configuration is the one choosed for comparison of the present code predictions. In order to perform the comparison, a modules for transport of particles has also been developed.

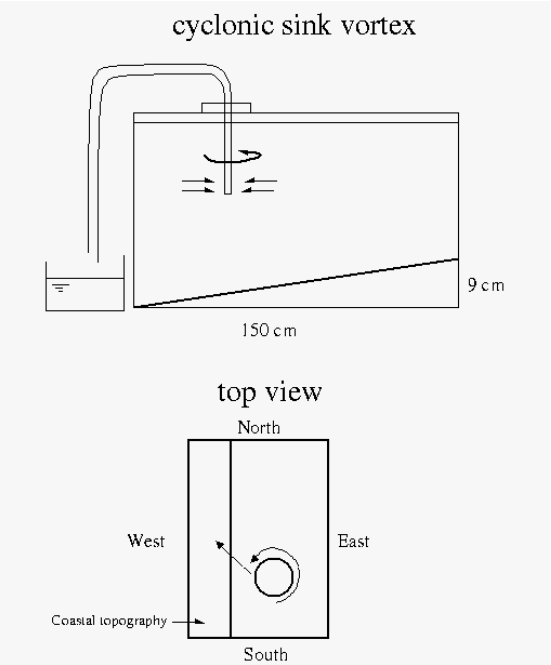

Figure 4.16: Scheme of the set up of the interaction of a vortex with bathymetry of Zavala-Sansón experiment in [55]

4.4 Interaction of a vortex with bathymetry

4.4.1 Interest and description

The aim of this numerical simulation is to demonstrate that the code developed here can reproduce the phenomena observed by Zavala Sansón and van Heijst both in the experiment and in the numerical model, described in [55].

To study this flow in the laboratory, Zavala Sansón and van Heijst used a rotating rectangular tank equiped with a topographic β-plane. The β-plane is simulated using a uniform weak linear slope at the bottom of the tank, over its length, which is dynamically equivalent to the variation of the Coriolis parameter in the β-plane approximation: finally north and south of the domain corresponds with the shallow and deep parts of the tank. To simulate a strong western topography, an additional bottom slope is fixed along the west side of the tank bottom. The tank is filled with fresh water and set at a constant rotation rate during 30 minutes previous to the experiment to ensure the fluid has reached a state of solid body rotation. The vortices are produced by syphoning a fixed amount of water through a thin perforated tube

during a certain period of time. To visualize the flow, fluorescent dye was seeded in the vortices and then recorded with a corotating camera located above the tank. Figure 4.17 shows several pictures of the trajectory of a cyclonic vortex over a western topography in the laboratory experimentent made by Zavala Sansón.
This is a way to reproduce, observe and measure, at a laboratory scale, the dynamic field induced by the variations with latitude of the Coriolis coefficient ($f = f_0 + \beta y$), which is called the β effect. Besides, the dynamics of large scale oceanic flow is driven by the conservation of potential vorticity (see chapter 2) which is function of the local Coriolis coefficient and the local depth. So changes in the topography can induce specific ocean dynamics in the same way the variation of the Coriolis coefficient does, and this is called "*the topographic* β *effect*". The scales of the topographic β value and the strong topography in the laboratory experiments have been chosen so they compare well with real continental slopes, and therefore a similar flow can be expected during the numerical simulation with oceanic parameters.

The real oceanic parameters used here are the same than the one used by Zavala Sansón and van Heijst: a rectangular domain of 1000 km in the direction East-West (x) and 1500 km in the direction North-South (y), meshed with a cartesian grid of 261x391 nodes. At the western wall the depth is 3000 m, and it increases linearly up to 5000m at $x = 333$ km. The horizontal kinematic eddy viscosity (ν_h) is chosen as 100 $m^2 s^{-1}$. The Coriolis parameter is given by $f_0 = 5.7\text{x}10^{-5} s^{-1}$ and $\beta = 2\text{x}10^{-11}$ (m s)$^{-1}$. Only the case where a cyclonic vortex encounters a steep western slope will be shown here. The initial vortex parameters are defined by its maximum vorticity ω_0=4 x 10^{-5} s^{-1}, its radius $R = 50$km, and the vorticity radial distribution approximated by $\omega(r)$ such as:

$$\omega(r) = \omega_0 \exp\left(\frac{-r^2}{R^2}\right) \tag{4.1}$$

Here r is the radial distance to the center of the vortex of coordinates ($x_0 = 500$,$y_0 =$ 750km). The bottom friction is not considered in the simulation of Zavala Sansón and van Heijst.

4.4.2 Results and discussion

The laboratory experiment made by Zavala Sansón and van Heijst shows that a cylonic vortex moves in the northwest direction on a β-plane. Then, the western

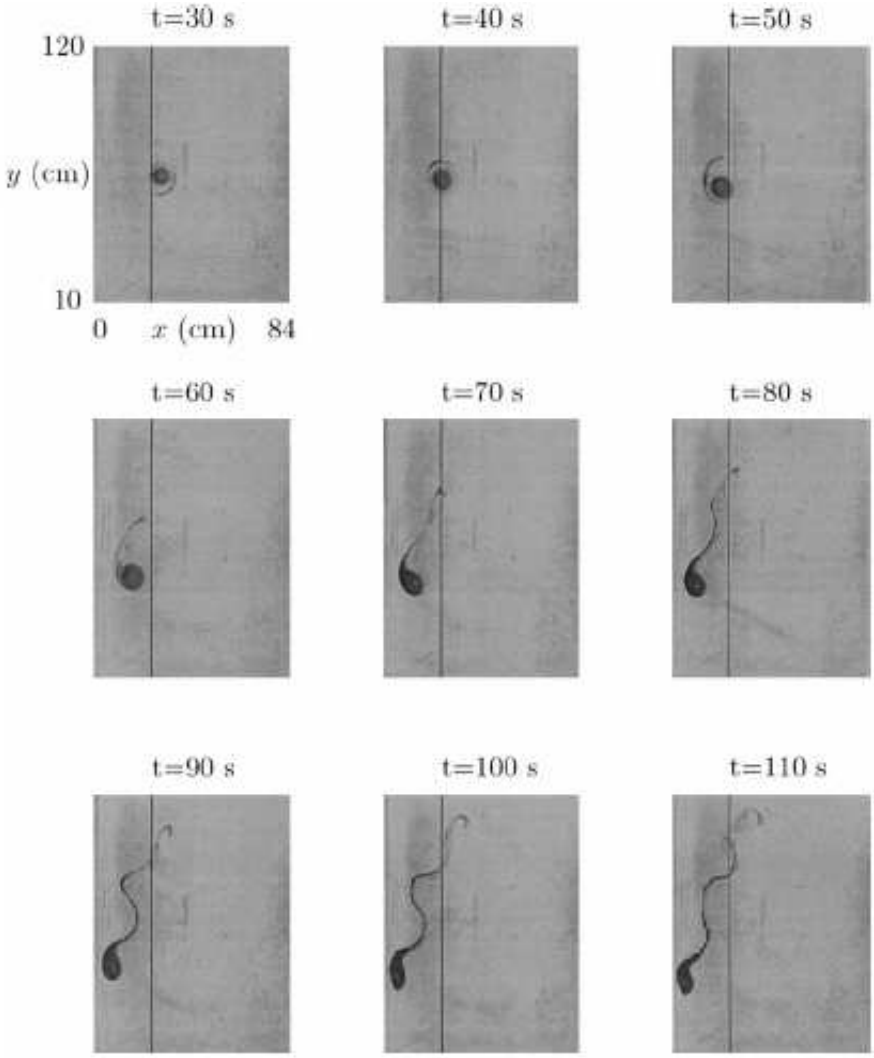

Figure 4.17: Zavala Sansón and van Heijst experiment: Top view photographs showing the evolution of the vortex–topography interaction. The vortex is visualized with dark dye. The western coastal slope starts from the vertical line at x = 23 cm. [55] Courtesy of Dr Zavala-Sansón

coastal slope induces a strong β effect that deviates the vortex southwestward (figure 4.17, for t<60s). Moreover, as the vortex moves uphill on the slope, a strong northeastward current is created, that meanders along the topography (figure 4.17, for t>60s). As the colored vortex indicates, the meandering current is formed with fluid from the vortex.

Both numerical simulations, in [55] and in the present work, reproduce very well these observations as shown in figures 4.18 and 4.19. When passive tracers are distributed randomly over the initial cyclonic vortex patch, with oceanic parameters, the mechanisms governing the vortex motion and the northeastward meandering current look to be well captured by the numerical models: the propagation is driven mainly by the conservation of potential vorticity. A strong change in depth induces a strong change in the relative vorticity and the advection of the vortex leads to the formation of the northeastward current. The meandering of this current is better explained looking at the vorticity field, as in the experiment only the initial vortex is visible but not the surrounding dynamic field.

The vorticity plots shown in the figures 4.20 and 4.21 give a better insight of the interaction of the initial vortex with the bathymetry. As can be seen, there is an intense vortex activity located over the slope where many cyclonic and anticyclonic cells are created. Both simulations show very similar prediction until up to 50 days. The northwestward advection of the initial cyclone is very clear in the first 15 days. Then the topographic β effect becomes locally stronger than the planetary β effect, and the cyclon heads to the southwest direction before decaying. As the cyclonic vortex migrates westward, the ambient fluid is entrained by the vortex upon the slope. To conserve the potential vorticity this fluid parcel starts to flow clockwise, like anticyclones (day 10 to day 25). This anticyclone at his time, entrains another fluid parcel to turn clockwise up the slope, and as this process is repeated it creates the northeastward current meandering in between the cyclonic and anticyclonic structures.

As a conclusion, the conservation of potential vorticity and the topographic β effect are the basic mechanisms governing the motion of oceanic meso-scale cyclones over western coastal topography. This case study proved that the model developed in this work is capable of predicting real oceanic flow phenomena strongly dependent to changes in depth and in latitude.

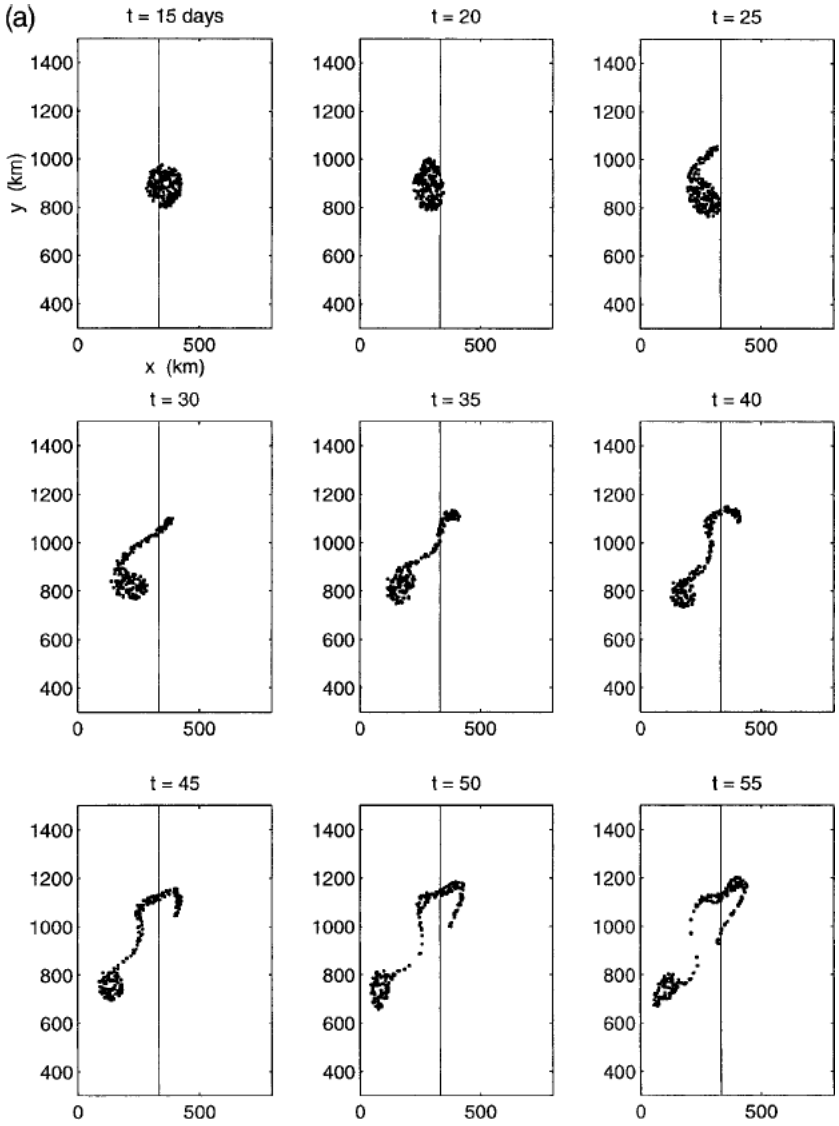

Figure 4.18: Tracer evolution from an oceanic cyclonic vortex-topography interaction as computed in [55]. Courtesy of Dr Zavala-Sansón

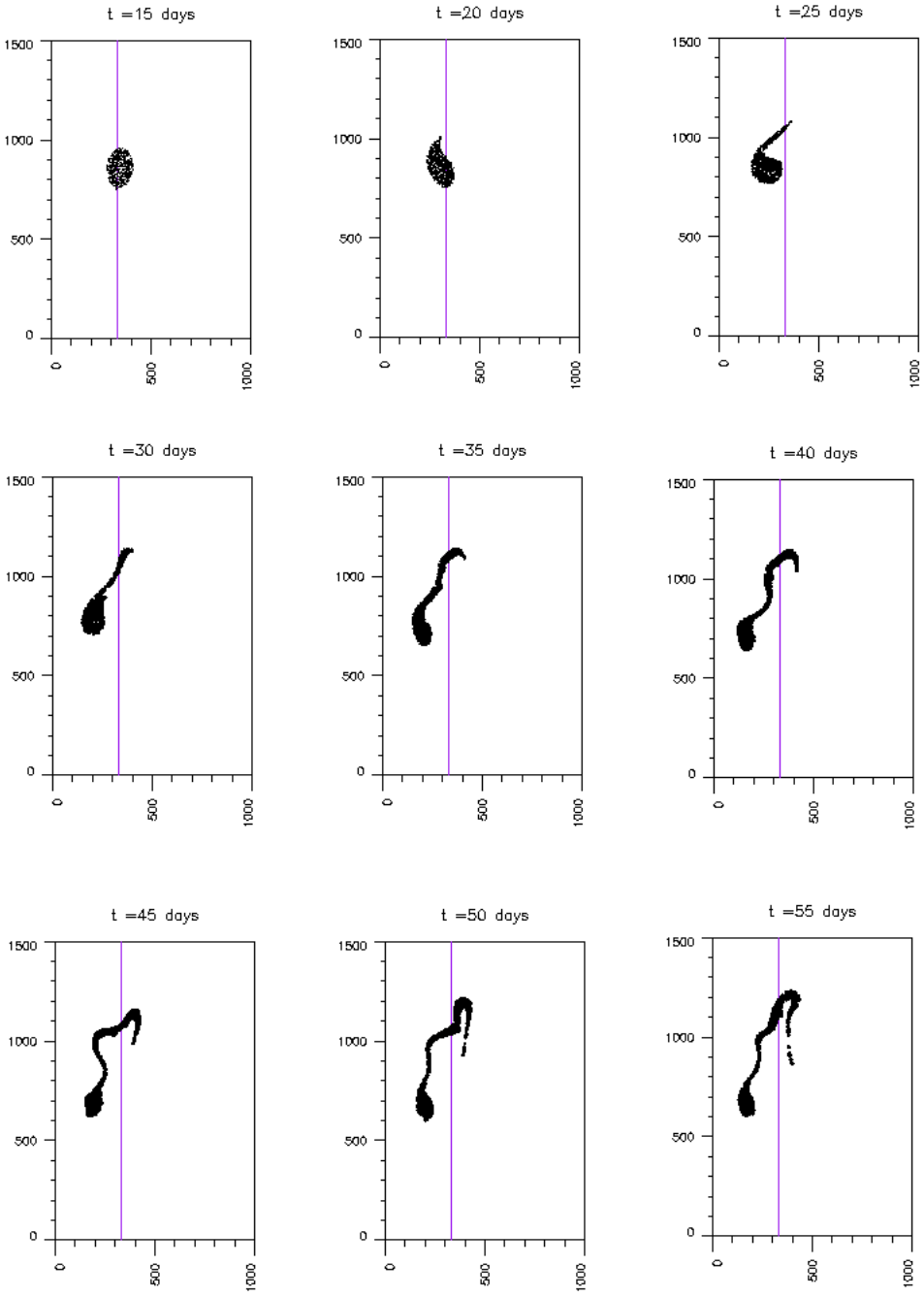

Figure 4.19: Tracer evolution from an oceanic cyclonic vortex-topography interaction as computed by the present code

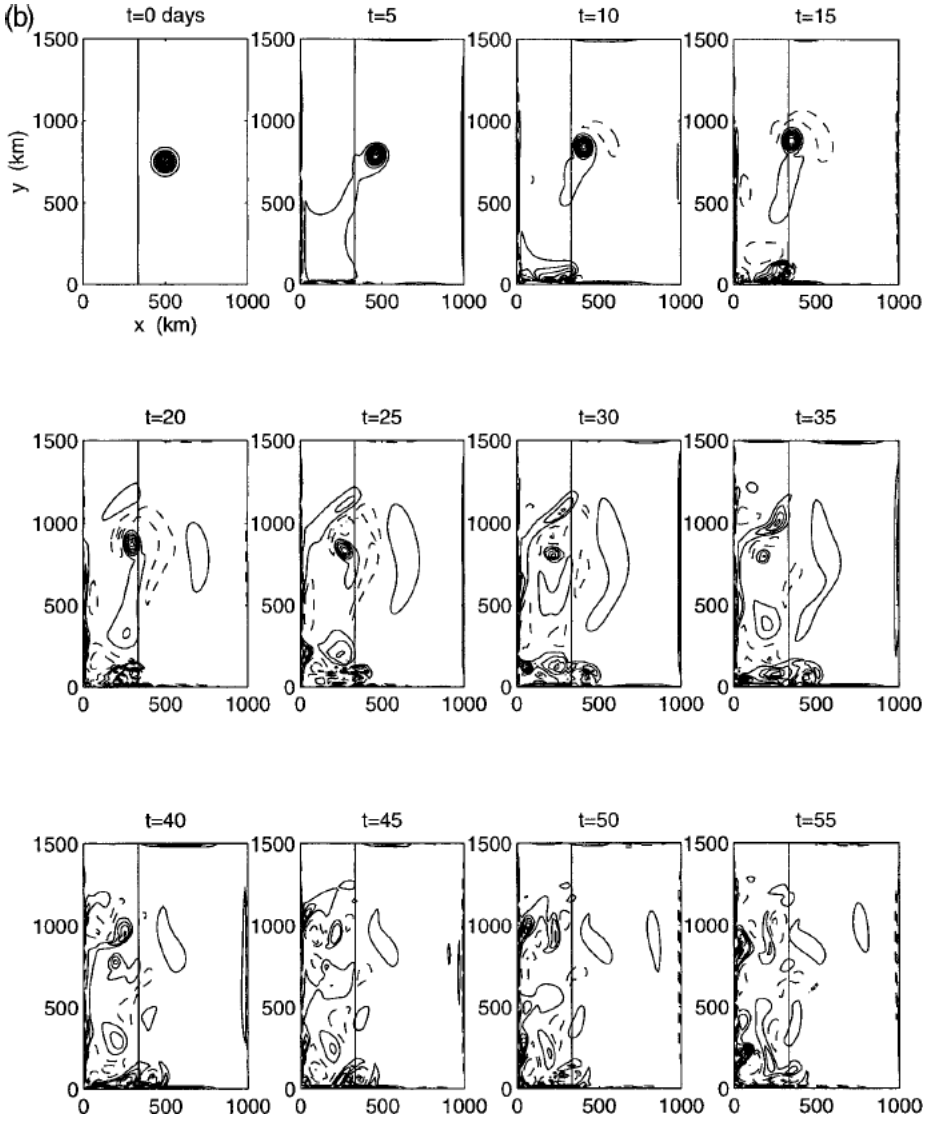

Figure 4.20: Vorticity contours from an oceanic cyclonic vortex-topography interaction as computed by [55]. Solid lines are positive contours, dashed lines are negative contours. Interval $\Delta\omega = 4\text{x}10^{-6}.\text{s}^{-1}$ in the range $[-8\text{x}10^{-6}, 12\text{x}10^{-6}]\text{s}^{-1}$. Courtesy of Dr Zavala-Sansón

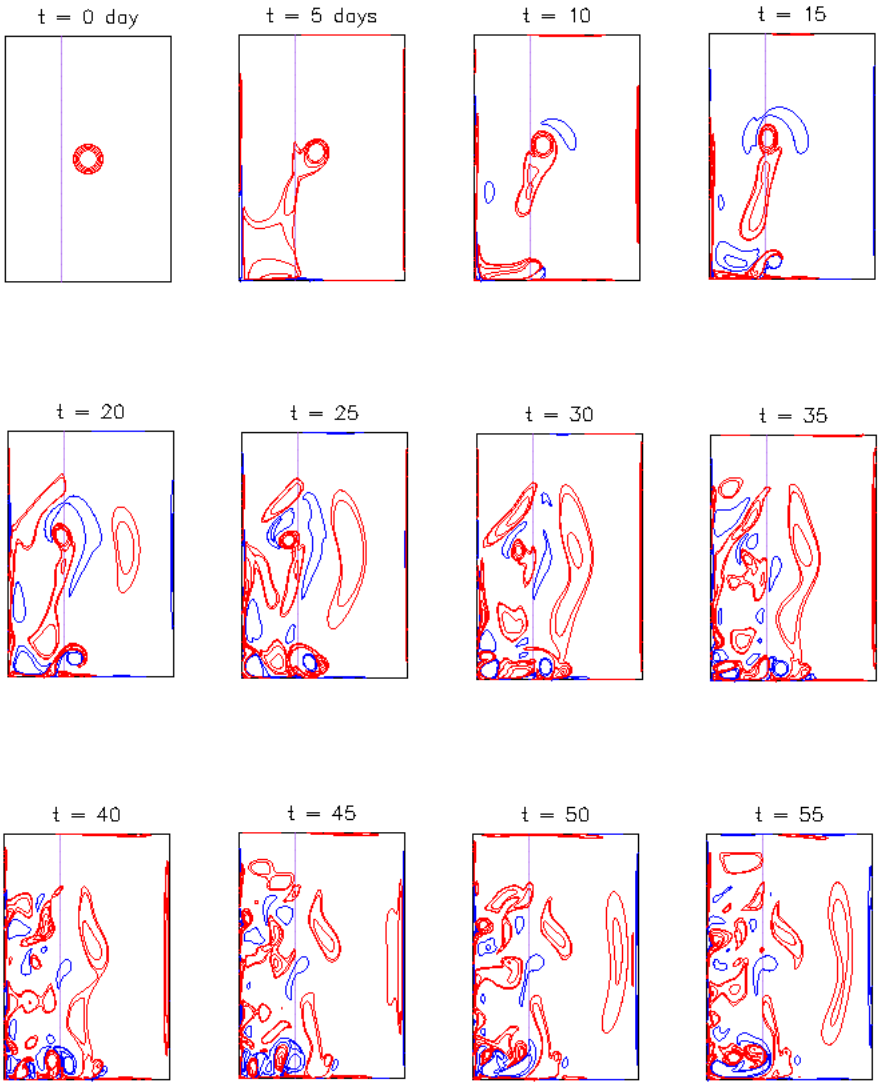

Figure 4.21: Vorticity contours from an oceanic cyclonic vortex-topography interaction as computed by the present code. Red lines are positive contours, blue lines are negative contours.Interval $\Delta\omega = 4\text{x}10^{-6}.\text{s}^{-1}$ in the range $[-8\text{x}10^{-6}, 12\text{x}10^{-6}]\text{s}^{-1}$.

Chapter 5

Numerical Simulations of Oil Spills Accidents

In this chapter two cases of oil spills are studied with the numerical simulation tool developed here.

The first one is a hypothetical accidental spill in the area of Tarragona harbour, a zone of intense traffic of oil carriers. This case was studied before with the previous version of SIMOIL, so it is possible compare the new numerical results with the ones of Cuesta et al. [11]

The second case is a real oil spill, consequence of the military conflict between Lebanon and Israel that occurred during the summer of 2006. This spill is specially interesting because many satellite pictures and numerical simulations have been used to monitor the spill during the event. The available data allows to show the capacity of SIMOIL to predict the spill behavior. The results demonstrate the improvement of the quality and accuracy of SIMOIL when associated to depth averaged flow predictions instead of a potential flow approximation.

5.1 A hypothetical oil spill off Tarragona harbour

5.1.1 The coastline of Tarragona

The port of Tarragona is located on the western coast of the Mediterranean Sea at $41^o05'$N of latitude and $1^o14'$E of longitude. According to previous studies of the circulation of the Catalan and Balearic Sea by Font et al. [56], the continental shelf

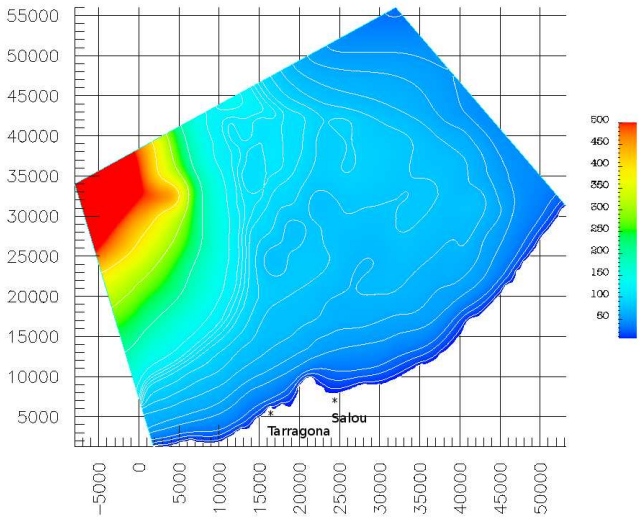

Figure 5.1: Marine domain and interpolated bathymetry along the coast of Tarragona.

is narrow in the area of Tarragona, approximately 15 to 25 km. It becomes wider, around 40 km, from cape Salou until the Ebro delta, and reach 60-80km in the gulf of Valencia. Figure 5.1 shows the area of computation. The bathymetry was extracted from the marine chart 486 "*DEL PUERTO DEL FANGAL AL PUERTO DE TORREDEMBARRA*" edited by the *Instituto Hidrografico de la Marina*. The general circulation is dominated by a permanent southwestern current flowing parallel to the coast until the Ebro delta where the circulation becomes more complex due to strong interaction between the permanent current and freshwater masses coming from the river outlet.

The city of Tarragona hosts one of the largest petrochemical industry site of Spain. According to the Tarragona port authority in the 2010 annual report [57], almost 33 million of tons of goods were exchanged (loaded or unloaded) through the port of Tarragona. Among this quantity around 17 million of tons of petroleum products (including crude oil, petrol, gas-oil, asphalt and other petroleum products) transited through the port of Tarragona in more than 1000 tankers during the year 2010. Besides that, the area of Salou, located at less than 10 km south of the port of Tarragona, is the most popular tourist resort of Costa Daurada, famous for its

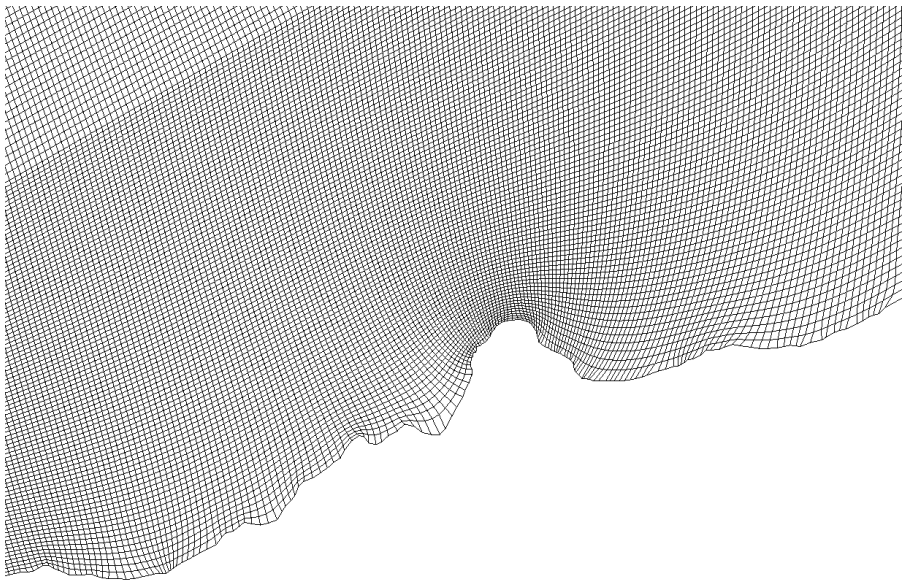

Figure 5.2: Detail of the curvilinear mesh around cape Salou.

tourism facilities and sandy beaches. Prevention and response actions has to be carefully planned in such areas to minimize the consequences of any accidental spill.

5.1.2 Parameters of the oil spill

In order to prepare for emergency situations, several numerical simulations of accidental oil spills have been conducted in the past by Cuesta et al. [38, 11]. They considered both instantaneous and continuous massive releases of crude oil in the vicinity of the port of Tarragona under different wind conditions. The case of a NE to SW wind of 3.33 $m.s^{-1}$ is studied here. It is a typical autumn wind along Tarragona coast, locally known as "vent gregal". As a first approximation for Cuesta et al. simulations [38, 11], the currents were supposed to be uniform following the potential streamlines parallel to the coast, with an intensity of 0.15 $m.s^{-1}$, in agreement with the measurements of Font et al. [56].
An 8 hours continuous release of 150,000 m^3 of crude oil of density 870 kg/m^3 is considered. Cuesta et al. simulation accounts for the oil evaporation, unfortunately these parameters were not published. The oil is supposed to leak from the Repsol

floating dock (a massive buoy used for unloading vessels outside of the port) located at 41°04'2,29"N et 1°13'13,82"E.

With the present code, a new velocity field is computed in agreement with the observations that takes into account the average velocity of 0.15 m.s^{-1}, a maximum inlet velocity of 0.25 m.s^{-1}, open boundary conditions at south and west sides (top and right sides of the figure 5.1 representing the domain), a bottom friction coefficient $C_D^{bottom} = 0.0025$ (typical value for coastal models [22]), the Coriolis parameter is calculated at every point of the domain according to equation (2.1.2).
The resulting flow is not potential: recirculations, circled in red in figure 5.3, appear in the lee of several headlands. These recirculations are weak as their current intensity is of the order of 0.001 m.s^{-1}, while the area in green in figure 5.3 has a current intensity of 0.15 m.s^{-1}. It can also be noticed that a coastal boundary layer is created where the intensity of the current significantly drop as it comes close to the coastline. It is due to the friction with the coast and the sea bottom the first 3 to 5 km off the coast are very shallow seas.
The same 8 hours oil leakage from the Repsol floating dock is studied. In the absence of data the model was run without evaporation as it does not affect the general trajectory of the oil.

5.1.3 Comparison of numerical simulations of the accident

The results of the simulation of the evolution of the oil using potential flow SIMOIL and depth-averaged flow SIMOIL are given in figures 5.4 and 5.5 respectively. 3, 6, 9 and 12 hours after the beginning of the spill.

In figure 5.4, it can be seen that after 12 hours, the isoline representing the limit of the area where oil thickness is greater than 5mm disappeared. This is due to both spreading and evaporation of the oil with time.
More importantly, the simulation shows that the slick would elongate driven by the action of wind and currents in the southwest direction overtaking the cape Salou 6 hours after the beginning of the spill. Then part of the oil slick would accumulate along cape Salou coastline while the rest would follow the contours of the coast.

In figure 5.5, the simulation shows a similar behavior of the oil slick. The significant differences are:

1. As the evaporation was not considered, the slick is thicker than in Cuesta et al. study. The area where oil thickness is greater than 5mm does remain and

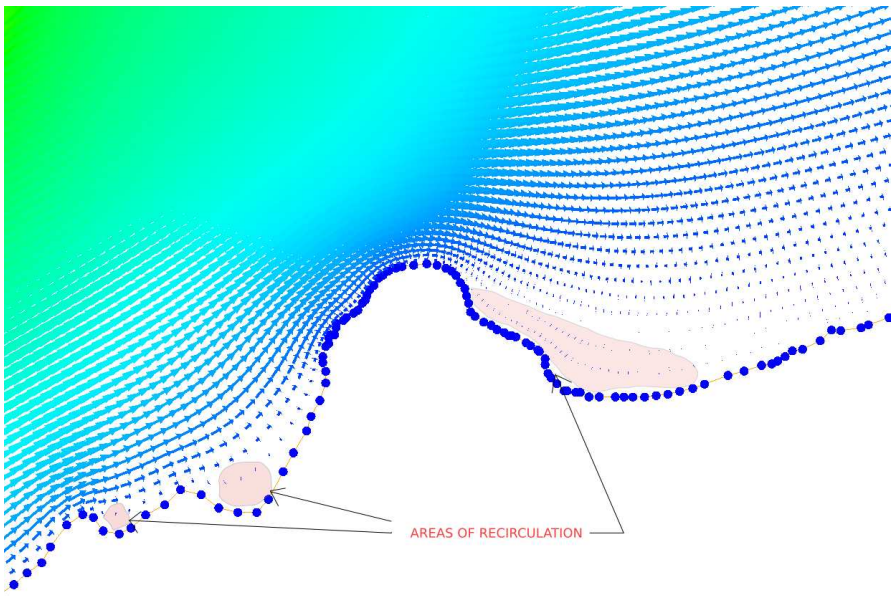

Figure 5.3: Detail of the sea currents around cape Salou.

extend during the first 12 hours.

2. The oil spill would not reach the coastline at cape Salou or downstream (only a small quantity of oil would land in the port of Tarragona around the Repsol dock, that was not represented in Cuesta et al. domain). This is due to the different hydraulic model used: in Cuesta et al. model, the currents intensity close to the coast are overvalued compared to the depth averaged currents model. As a result, with the depth averaged model, the currents have less influence on the oil spill drift than the wind has. So the oil slick travels less along the coast and extend more in the southwest direction of the wind.

As a conclusion, this case is an example of the importance of resolving correctly the coastal currents and evaluating the evaporation loss for oil spill modelling. The quantity of oil remaining at sea, specially the thickness of the slick, is a critical information to prepare the response actions like the mechanical recovery of the oil at sea. This quantity cannot be approximated properly without accounting for the evaporation of the oil. Coastal currents are boundary layer flows characterised by a strong gradient of velocity in the direction orthogonal to the coast. For strong winds ($>$ 6 to 9 m.s^{-1}), the results of both potential and depth averaged flow models will

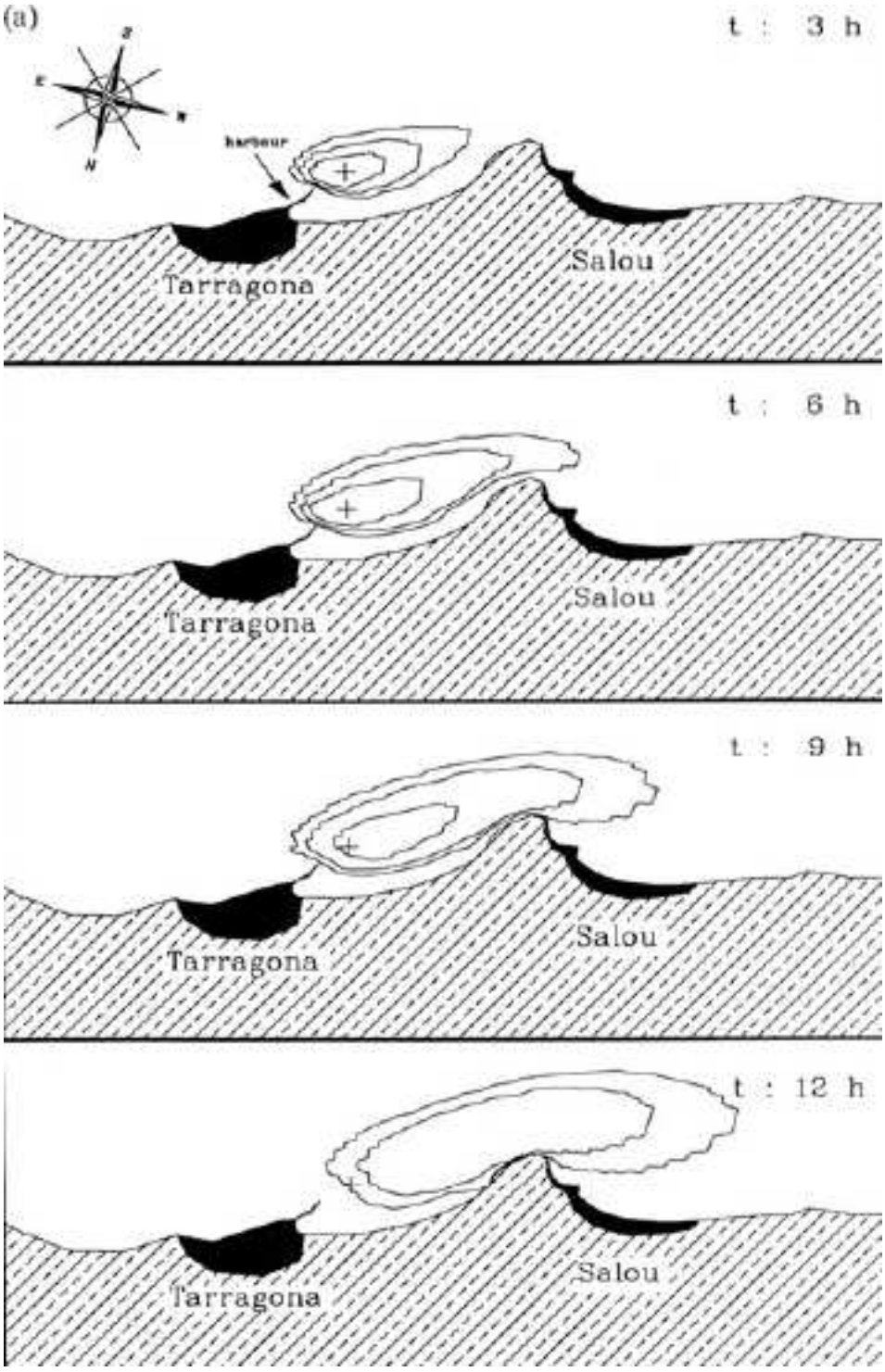

Figure 5.4: SIMOIL-Potential flow. Evolution of the oil spill 3h, 6h, 9h, 12h after the beginning of the 8 hours oil leakage at the floating dock. 3 Isolines of the oil thickness are plotted: 10^{-6}m, 10^{-3}m, 5.10^{-3}m. Image courtesy of Cuesta et al. [11]

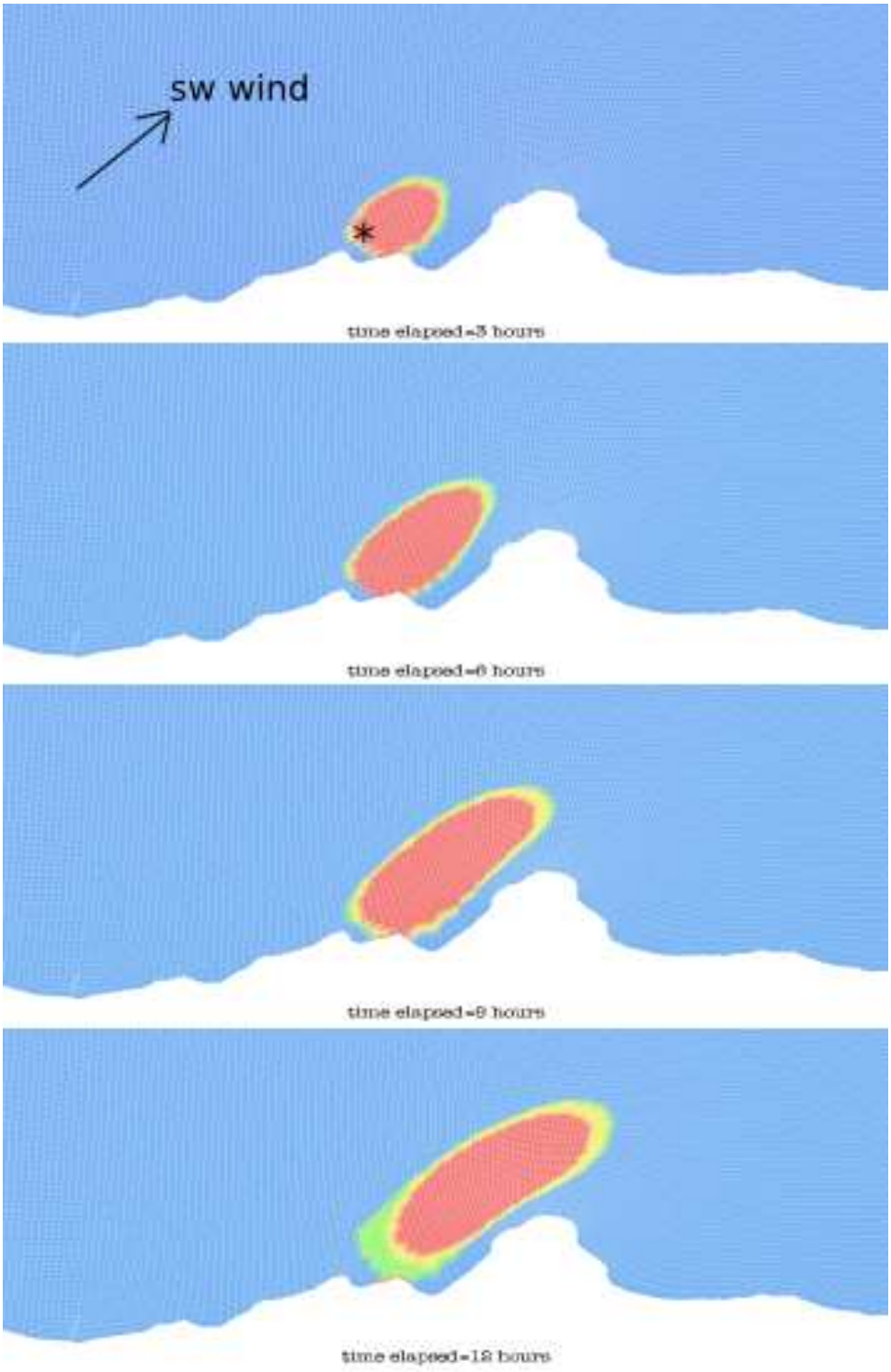

Figure 5.5: SIMOIL-Depth-averaged flow. Evolution of the oil spill 3h, 6h, 9h, 12h after the beginning of the 8 hours oil leakage at the floating dock. Oil thickness h colors: red for $h > 5.10^{-3}$m, yellow for $10^{-3}\text{m} < h < 5.10^{-3}$m, green for $h < 10^{-3}$m

be similar, as the contribution of currents to the trajectory of the slick will be very weak compared to the wind contribution. For moderate winds, the depth averaged currents modelling is a better option to predict realistically the transport of oil spill in coastal areas.

5.2 Massive oil spill on the coast of Lebanon

5.2.1 The coastline of Lebanon

Lebanon is located between latitudes 33^o and 35^o N and longitudes 35^o and 37^o E. It is bordered by Syria at North and East, by Israel at South, and by the Mediterranean Sea at West. The UNEP[1] report on the Lebanon war environmental consequences [58] states that the 225 km of coastline of Lebanon are very urbanized and densely populated, attracting most of the industrial plants directly on the shore (such as power plants, chemical companies and refineries). The coastline is made of sand beaches (20%) and rocky or gravel shorelines.

The bathymetry is characterised by a sharp transition separating a narrow and shallow continental shelf from the deep Levant basin offshore. The currents system is dominated by a large scale counterclockwise Mediterranean current that transports water towards the North up the Lebanese coast. During summer, the seawater uses to remain at high temperature around 30^oC and its salinity is higher than the western sea, given that the evaporation exceeds the precipitation and rivers run-off.

5.2.2 The oil spill

According to the Green Line association[2] oil spill report [59], the 2006 Lebanon war opposing Israel to Hezbollah started on July 12^{th} 2006. The conflict lasted 34 days until a ceasefire was brokered by the United Nations. On July 13^{th} and 15^{th} of 2006, the Israeli Air Force bombed the storage fuel tanks of Jiyeh power plant, located on the seashore at 30 kilometers South of Beirut, causing 75,000 tons of heavy fuel oil to burn or leak into the sea during the following weeks. The exact amount of oil spilled into the sea remains unknown though it has been often

[1] United Nation Environment Program

[2] Green Line is a Lebanese non-governmental association promoting environmental awareness and documenting environmental threat in Lebanon.

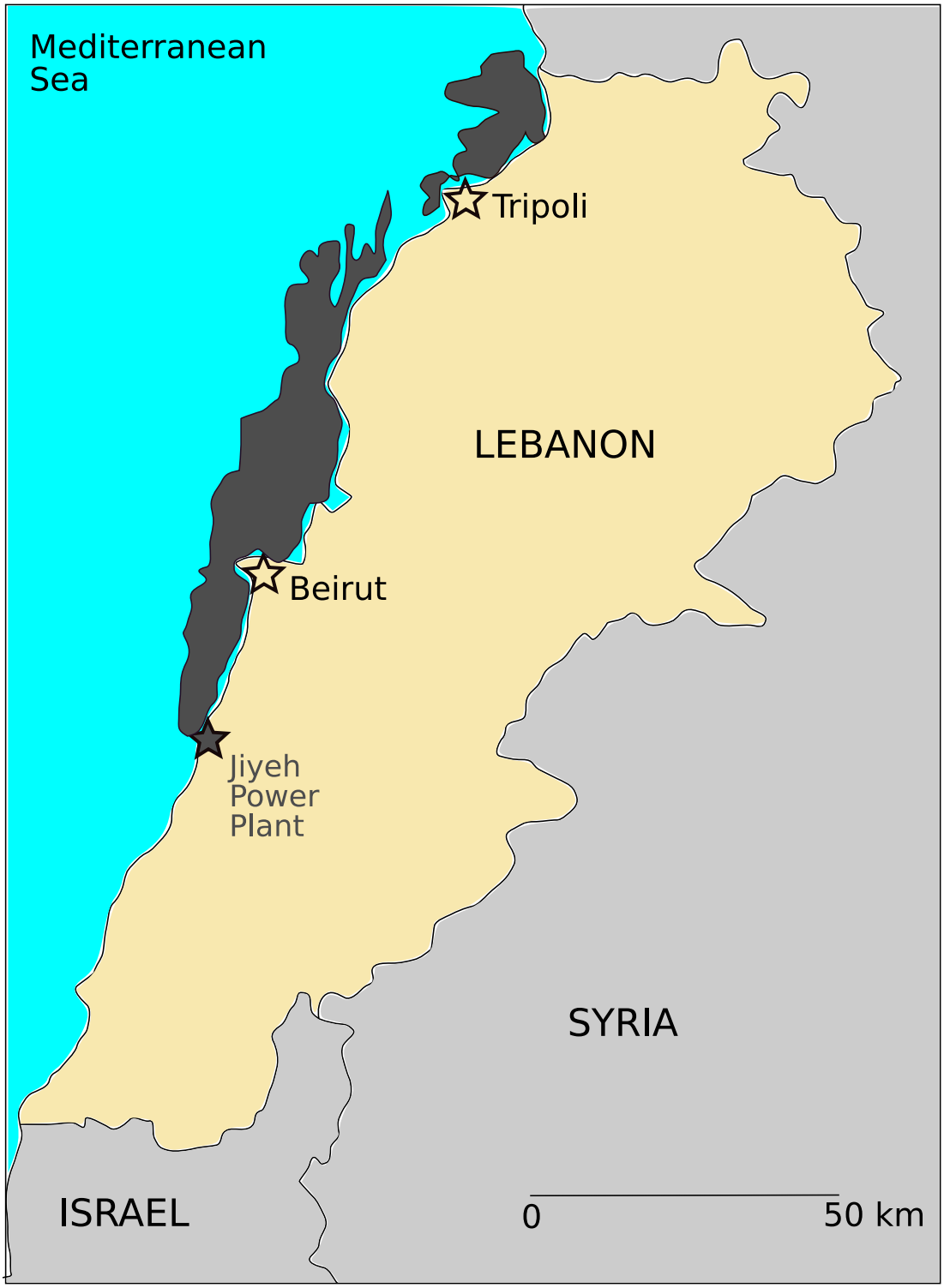

Figure 5.6: Maximum extent of the Lebanon oil spill in dark grey color as monitored by satellite. Sources to draw the map include [58, 59, 60]

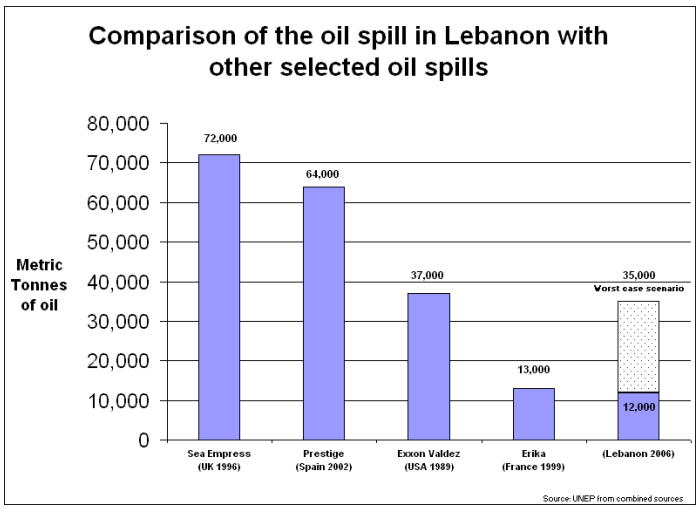

Figure 5.7: Comparison of the oil spill in Lebanon with other oil spills accidents. Courtesy of [58]

estimated that 15,000 tons of oil (see figure 5.7) were released into the sea mainly during the first week. The remaining 60,000 tons were still burning 2 weeks after the strikes. The consultant sent by IUCN[3] on August 14^{th} found this estimation reasonable, and noticed that fresh oil was still trapped in cracks and may be leaking slowly out on the shoreline near Jiyeh fuel tanks farm [59].

The oil contained in the tank was reported to be heavy fuel oil [58] of the type IFP 6. According to Irwin et al. [61], fuel oil #6 is a residual oil manufactured from residues from refinery processing. Its composition is complex and variable depending on the source , refinery design and product requirement. This fuel oil is known to have few evaporation or dissolution potential, and as such may be highly persistent. Among the fuel oils, number 6 is the heaviest, with a density slightly lower than sea water about 920–1000 kg/m3 which may cause it to sink easily. The viscosity is high, making it to spread slowly, and it weathers also very slowly and tends to form stable emulsions as tar balls or ”pancakes”.

Green Line observers network reported that the oil that did not burn, or sink, was caught in the northbound current and transported up the Lebanese coast toward Syria [59]. The dominant winds, blowing mainly to the northeast during that summer, prevented the oil from spreading offshore and pushed it against the coastline and northward. Generally, portions of coast facing west and southwest were more

[3]International Union for Conservation of Nature

Figure 5.8: Impact of the oil spill in Byblos bay august 2006. Credits [59]

contaminated than the one facing north, with the exceptions of harbours and bays where the oil got trapped in. About 150 km of coastline were directly and severely damaged by the oil spill. Impacted locations included the Marine Protected Area of Palms Islands near Tripoli, the archaeological sites in Byblos as can be seen in figure 5.8, and most of the fishing harbours at the north of Jiyeh.

5.2.3 Oil spill simulation setup

5.2.3.1 Objective and interest

This hindcast simulation (prediction made a posteriori) pursues two objectives. Firstly, the objective is to illustrate how the prediction of the dispersion of the oil can change if it is driven by a hydraulic model based on the solution of a potential flow, as in the old version of SIMOIL, or by depth averaged coastal currents, as in the version developed here. Secondly, it is aimed to validate this new model by comparing to satellite images, field observations and the numerical model of reference for the Eastern Mediterranean Sea : MEDSLIK-CYCOFOS.

To achieve this purpose, a mesh is built over the coastal area of Lebanon and Syria, integrating environmental data such as the bathymetry and sea temperature and average current direction, to run the hydrodynamic model presented in the chapters 2 and 3. A summary of the running conditions of the three models is given at the end of this section.

Figure 5.9: Area of simulation

5.2.3.2 Parameters and hydrodynamics

Area of simulation

The domain defined to carry out the simulations (for both potential and depth averaged flow field) is almost a rectangle of about 220 km x 65 km. It covers the coast of Lebanon from Alinseniyah (33,43°N ; 35,27°E) to Jebleh (35,34°N ; 35,92°E) in Syria as shown in figure 5.9. The coastline is extracted from an ASCII file (1257 points) based on the World Vector Shoreline Database provided on-line[4] by the National Geophysical Data Center of the National Oceanic and Atmospheric Administration.

Every point on the coastline is located by his latitude and longitude. The longitude and latitude of reference are taken respectively as $\lambda_0 = 35,00N$ and $\varphi_0 = 34,50E$, at the center of the domain. The coordinates of any point $P(X,Y)$, in a Cartesian (metric) coordinates system centered in this point of reference, with X axis positive northward and Y axis positive westward, are given by:

$$X = M(\varphi)\frac{\Pi}{180}\Delta\varphi \tag{5.1}$$

$$Y = N(\varphi)\cos\varphi\frac{\Pi}{180}\Delta\lambda \tag{5.2}$$

where λ and φ are the longitude and latitude of P, and $\Delta\lambda = \lambda - \lambda_0$ and $\Delta\varphi = \varphi - \varphi_0$.

[4] http://www.ngdc.noaa.gov/mgg/coast/

$M(\varphi)$ and $N(\varphi)$ are respectively the radius of curvature in the meridian (north-south) and in the prime vertical (east-west) around the point of reference at latitude φ_0, which are defined geometrically in the World Geodetic System 1984 (WGS84) of reference [62] as:

$$M(\varphi) = \frac{a(1-e^2)}{(1-e^2\sin^2\varphi)^{\frac{3}{2}}} \tag{5.3}$$

$$N(\varphi) = \frac{a}{(1-e^2\sin^2\varphi)^{\frac{1}{2}}} \tag{5.4}$$

Where $a = 6378137m$ is the Earth equatorial radius and $e = 0.08181919084$ is the first eccentricity of the WGS84 ellipsoid [62]. Note that Jiyeh power plant latitude is 33,65030N and its longitude is 35,40827E. A curvilinear grid is then generated, consisting of 314 points along the shoreline and 92 points in the direction normal to the coast.

The bathymetric data is available on-line[5] from Smith [63] and provides 26499 measurements from satellite altimetry and ship depth soundings in the area of interest. The depth is interpolated on every mesh points using the bi-variate interpolation algorithm [41, 42]. The topography is then simplified to eliminate strong gradients of depth that could make the hydrodynamic solution unstable: the maximum depth is set to 1400 meters and the Palms Island, off the coast of Tripoli, are eliminated during the smoothing process as can be seen on figure 5.10.

Hydrodynamics

The coastal oceanic current model validated in the previous chapter is used to compute a steady depth averaged sea current velocity field over the domain. It is forced with a northerly plan flow parallel to the coast at the south face of the domain. The initial conditions are a potential flow with a velocity of 25 cm/s. With these conditions, the code is ran until the stationary state is achieved.

As shown in the figure 5.11, the coastal current is directed northward along the coasts of Lebanon and Syria. Separation flow appears in the lee of several capes, specially in the bays of Beirut and Tripoli, but also after smaller headlands. The anticyclonic eddies formed in the gulfs appear stable even for the weak ones.

Offshore and inshore, the flow field computed is consistent with the climatological flow regime known for this region and season. Additionally it gives important information about the currents in the many gulfs of Lebanon coast. For example,

[5] http://topex.ucsd.edu/cgi-bin/get_data.cgi

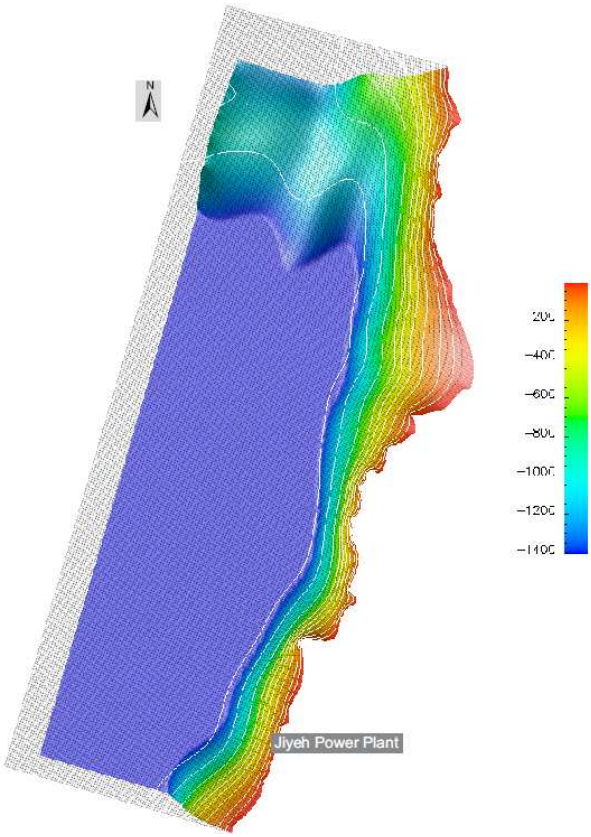

Figure 5.10: Computational mesh and bathymetry of the coast of Lebanon.

the recirculation that extends through the whole gulf of Tripoli is very weak. There is no doubt that, in the case of the depth average flow, in this area, the trajectory of the oil slick will be driven more by the wind than by the sea currents.

The direction and intensity of the wind for the month of July and August were extracted from the measurements at the meteorology stations of Beirut and Tripoli. There is an apparent variability between days and nights and some data are missing (probably due to the war events) in the file provided by MeteoArchive[6]. That is the reason why an averaging per period of 12 hours have been done between 10AM and 10PM. When whole days were missing an interpolation of the direction of the wind was made considering the direction of the smoke plume coming from the Jiyeh power plant in fire as it appears on satellite pictures, combined with the apparent drift of the oil slick. An example of the measurements of the daily evolution of the north-south and east-west component of the wind in Beirut can be seen in figure 5.12.

Oil properties

The density of the oil is set to $\rho_o = 930$ kg m^{-3}, slightly less than seawater density $\rho_w = 1030$ kg m^{-3}. The momentum transfer coefficient between oil and water is set to $k = 10^{-2}$kg m^{-2} s^{-1}. The temperature of the sea surface appeared to be constant and uniform at 30^{o}C.

The source is located at 300 meters offshore of Jiyeh power plant, and is modelled as a circular source of 250 meters of radius. It releases 20,000 cubic meters 6 days long (144 hours) starting on July 13th.

The model of evaporation follows the empirical equations established by Fingas [64] for Bunker C oil which reads :

$$\text{if} \quad t < 24 \text{ minutes, then} \quad \%Ev = (0.35 + 0.013T)\sqrt{t} \tag{5.5}$$

$$\text{if} \quad t \geq 24 \text{ minutes, then} \quad \%Ev = (-0.21 + 0.045T)\ln t \tag{5.6}$$

Where t is the time in minutes and T is the temperature of the oil at sea in Celsius degrees. Then $\%Ev$ is the percentage of the volume of oil spilled that has evaporated.

[6] http://int.meteoarchive.com/overview.html MeteoArchive provides historical weather data worldwide

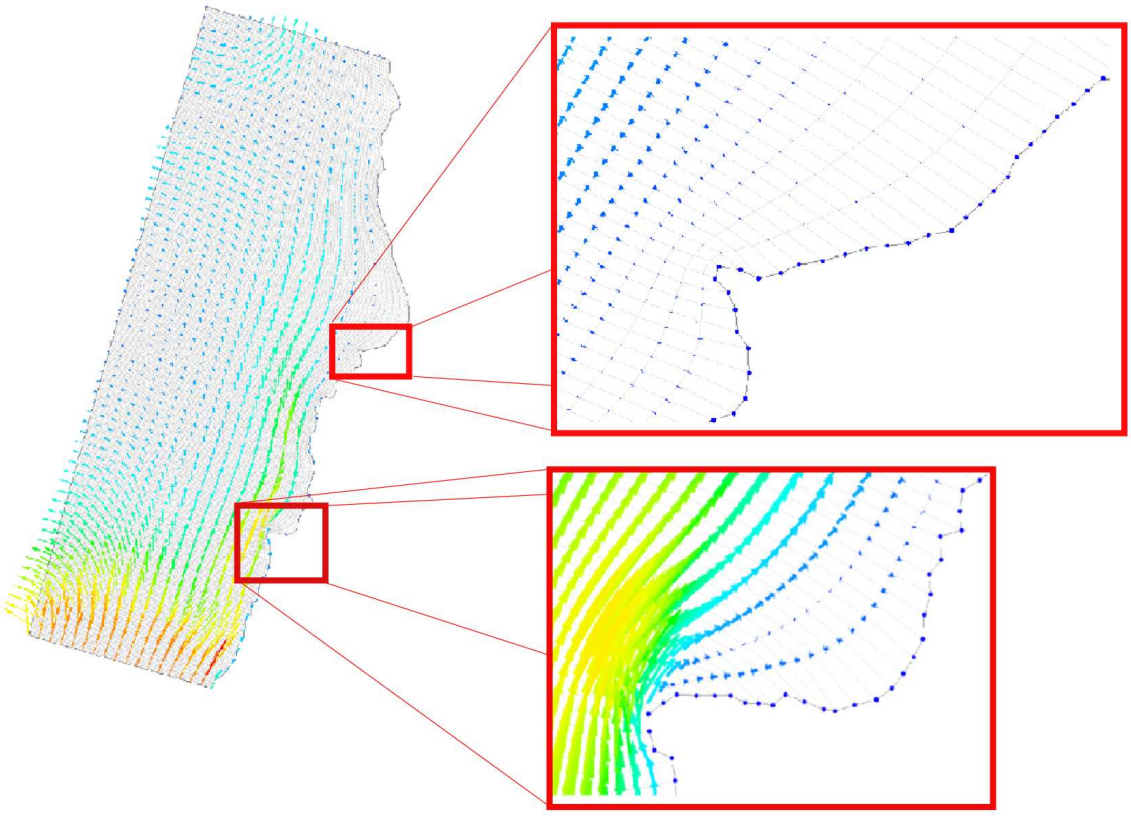

Figure 5.11: Depth averaged currents along the coast of Lebanon. Zoomed in: the recirculations in the bays of Beirut and Tripoli. The eddy in the gulf of Beirut shows intense currents compared to the eddy in the bay of Tripoli where the currents are very weak.

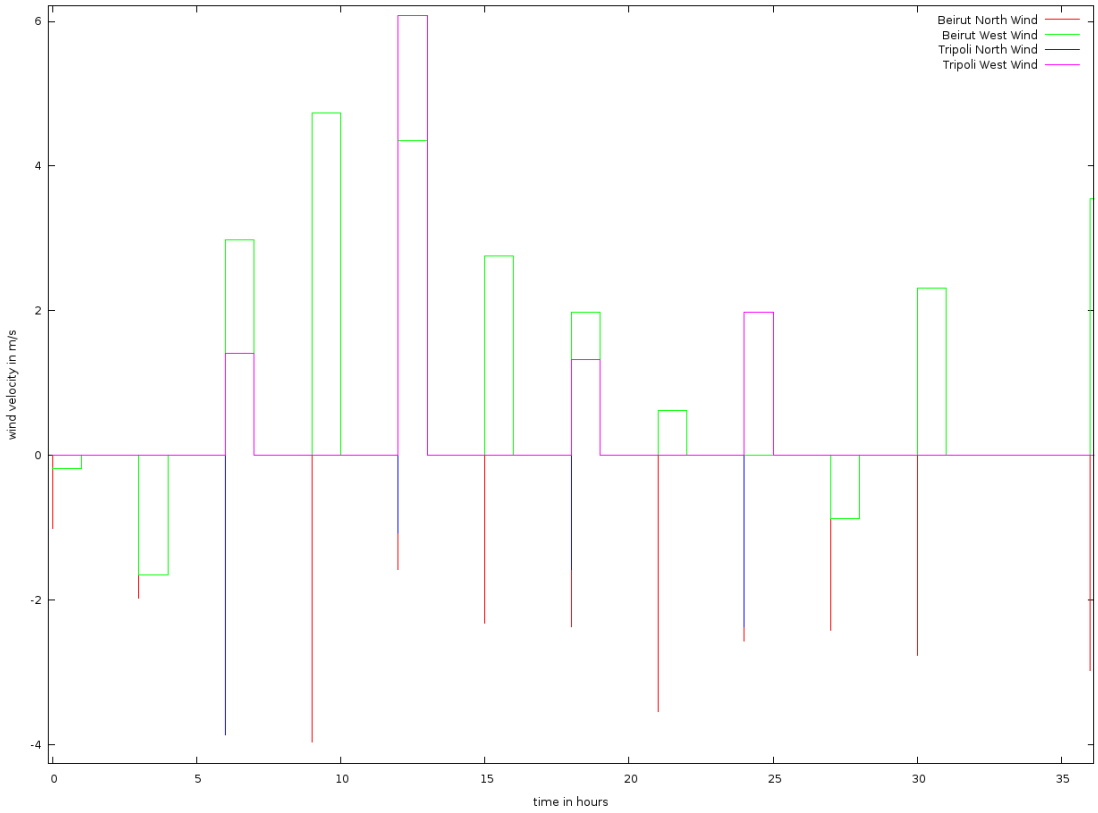

Figure 5.12: Wind direction and intensity during the first 36 hours of the spill in Beirut and Tripoli

5.2.3.3 Summary of the simulation cases

Two models are run and compared to satellite pictures and to the MEDSLIK-CYCOFOS model that was run in real time during the oil spill event in July 2006. The three numerical experiments are summarized in the table 5.1.

The first two numerical experiments are run over the 314 x 92 points generalised mesh described previously. The potential flow case corresponds to the old version of SIMOIL developed by Cuesta in [11, 38]. The depth averaged experiment corresponds to the model of this work. The comparison of both numerical models allows to see the improvement made between the two versions of SIMOIL.

The third simulation is described in details in [60]. In it, the hydrodynamics is calculated according to CYCOFOS predictions and the oil dispersion is computed by the MEDSLIK model for oil transport. It is the operational model of reference in the Eastern Mediterranean sea, and it is used to validate this work.
The Cyprus Coastal Ocean Forecasting and Observing System (CYCOFOS) is run to compute the sea currents along the Lebanese and Syrian coast. CYCOFOS has a horizontal spatial resolution of approximately 1.8 km with 284 x 206 grid points with a time step of 240 seconds. For the vertical discretization, 25 terrain-following sigma layers are used. CYCOFOS uses the atmospheric data provided by SKIRON wind forecasting system at 5 km x 5 km and 1 hour resolution. Initial and boundary conditions come from the ALERMO sub-regional model which is nested within the Mediterranean Forecasting System MFS. MFS is run with a 6km and 600 seconds time step with an atmospheric resolution actualised every 6 hours (European Medium Range Weather Forecast). MFS analyses and forecasts are continuously compared with remote and in-situ observations and assimilating data. Finally CYCOFOS provides 6-hourly mean forecasts for the next 4.5 days on a daily basis.
In the oil spill model MEDSLIK, the oil spill is represented as thousands of Lagrangian particles. The trajectory of the particles is determined by water currents, wind and turbulent diffusion processes. The particles are also subject to transformation processes such as emulsification or evaporation, that eventually modify their physical properties such as density and viscosity.

5.2.4 Results and discussion

Comparisons between the oil slick extent and position detected by satellite images (MODIS and ASAR) and predicted by the 3 experiments are presented in the

	Experiment 1	**Experiment 2**	**Experiment 3**
Current field	Potential flow	Stationary depth averaged	CYCOFOS 6 hourly forecast
Wind field	Meteo Archive Beirut and Tripoli	Meteo Archive Beirut and Tripoli	SKIRON
Spill position	33°39'1"N 35°24'29"E	33°39'1"N 35°24'29"E	33°40'N 35°24,75'E
Start spill date	13/07/2006 00:00	13/07/2006 00:00	13/07/2006 08:00
Total mass of spill	18,600 tons (20,000 m^3)	18,600 tons	18,770 tons
Type of oil	Bunker C oil $\rho_o = 930$ kg m^{-3}	Bunker C oil $\rho_o = 930$ kg m^{-3}	API=20
Wind correction factor	3%	3%	3%
Current depth	Surface	Depth averaged	30 m
Spreading	SIMOIL	SIMOIL	90,000 Lagrangian particles
Evaporation	No	Empirical equations [64]	Boundary layer model of Mackay

Table 5.1: Overview of the model runs for the Lebanon oil spill

figures 5.13–5.18. The images from the CYCOFOS model, extracted from [60], show in red the position of the particles representing the oil parcels and in green oil slick regions digitized from satellite pictures, so as to be more easily compared. The images from SIMOIL, for both potential and depth averaged flows, show the position, the extent and also the thickness of the oil slick, giving direct visual information about where the most important quantity of oil can be found at sea and on the coast.

The first available[7] satellite picture of the area, in figure 5.13(a), is from **16th of July**. The coastline is partially covered by clouds but the smoke plume rising from the power plant is visible and confirm the southwest direction of the wind.
The depth averaged model coupled to SIMOIL shows, in figure 5.13(b), that the oil is transported northward until the west of the entrance of the gulf of Beirut, but without reaching the coast yet. At this moment only the shoreline around Jiyeh is accumulating oil as the west component of the wind seems to push the oil offshore.
The potential flow model coupled to SIMOIL shows, in figure 5.13(c), a significantly different evolution of the oil slick already filling the gulf of Beirut up to the port of Jounieh at the north of Beirut. In this model, the absence of recirculation currents in the gulf increases the advection of the oil to the North and prevents the oil to detach from the coast due to the strengthening of the sea currents parallel to the coast in comparison with the other model.

In the following 3 days, the main direction of the wind switches to northeast. **On July 19th**, the MODIS AQUA image in figure 5.14(a) shows the oil slick as a strip elongated in the north direction. The oil has clearly reached the coast between Jiyeh and Beirut, and passing over the headland of Beirut, surrounds the gulf up to Byblos area. A black smoke plume is still rising from Jiyeh power plant, this time heading north.
SIMOIL, coupled to depth averaged currents, predicts a pattern of the oil slick extension very similar to the one in the satellite image until Byblos, as can be seen in figure 5.14(b). Specially the thickest portion of the slick is in very good agreement with the most visible oil in the satellite image. Though this model predicts the extension of the oil slick up to Enfeh latitude. This offshore oil, between Batroun and Enfeh, does not appear clearly in the satellite picture.
In figure 5.14(c), the SIMOIL version coupled to potential flow currents shows that

[7] http://www.disasterscharter.org/web/charter/activation_details?p_r_p_1415474252_assetId=ACT-126 and http://www.zki.dlr.de/article/865

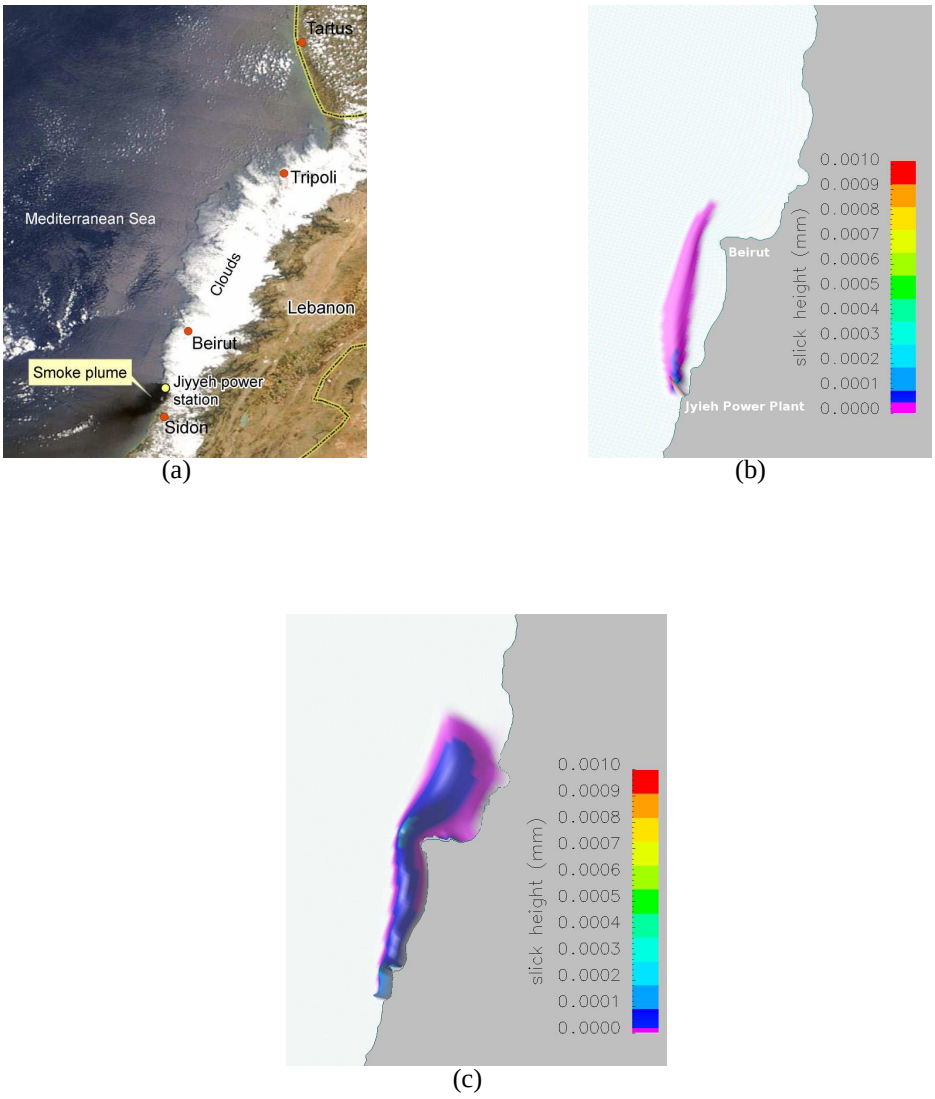

Figure 5.13: Oil slick extent on **July 16**th: covered by clouds as shown by MODIS AQUA satellite in figure 5.13(a). Figure 5.13(b) shows the oil slick at the height of the cape of Beirut as predicted by SIMOIL coupled to the depth averaged currents model. Figure 5.13(c) shows the oil slick filling up the gulf of Beirut as predicted by SIMOIL coupled to the potential flow currents model.

the oil continues spreading north and already reaches Syrian coast after having filled the gulf of Beirut and the gulf of Tripoli and impacted heavily the beaches between Jiyeh and Beirut first. Every beach facing southwest, from Jounieh to Syria would be polluted by the oil spill.
The MEDSLIK-CYCOFOS prediction in figure 5.14(d), is somehow in between the last two predictions about the extension of the slick. The forecast report (not shown here) says that 80% of the oil has landed, mainly between Jiyeh and Beirut and between Jounieh and Chekka. This result agrees well with satellite observations and the depth averaged currents version of SIMOIL. The oil that remains at sea would be located in the gulf of Tripoli, between Tripoli and Syria, in agreement with the potential flow version of SIMOIL.

On July 21st, 192 hours after the beginning of the oil spill, an ASAR image of the oil in the gulf of Beirut is provided in Coppini et al. [60] article. It is reproduced in figure 5.15(a).
The behaviour of the oil slick in the gulf of Beirut is very well reproduced by SIMOIL when coupled to depth averaged currents as the oil trapped at the south of Beirut headland slowly moves northward to land on the beaches from Jounieh to Enfeh. The model reports in figure 5.16 that about 45% of the volume of the spilt oil has landed there while around 10% has evaporated, and 45% is still in the sea off the coast of Tripoli.
The potential flow version of SIMOIL, shown in figure 5.15(c), contrasts with that description, as in this case most of the oil already left the region between Jiyeh and Tripoli. Some of the oil remained in the gulf of Tripoli, while the rest has soaked all the coast of Syria until the north boundary of the domain.
Again, the MEDSLIK-CYCOFOS forecast agrees well with the satellite picture and SIMOIL coupled to depth averaged currents for the extension of the oil up to Tripoli. It also predicts landing of oil in the gulf of Tripoli and up to Tartus on the Syrian coast.

On July 23rd, the satellite picture, in figure 5.17(a), shows a complex pattern of the extension of the oil slick. Ten days after the beginning of the leakage, the oil continues travelling northward pushed by the sea currents. A long strip has detached to the north of Tripoli and some oil appears to be encircling Palm Islands and starts invading the bay of Tripoli. At the same time, oil that previously landed on the coast between Jounieh and Chekka, is remobilized by westward winds and enters again the north current.

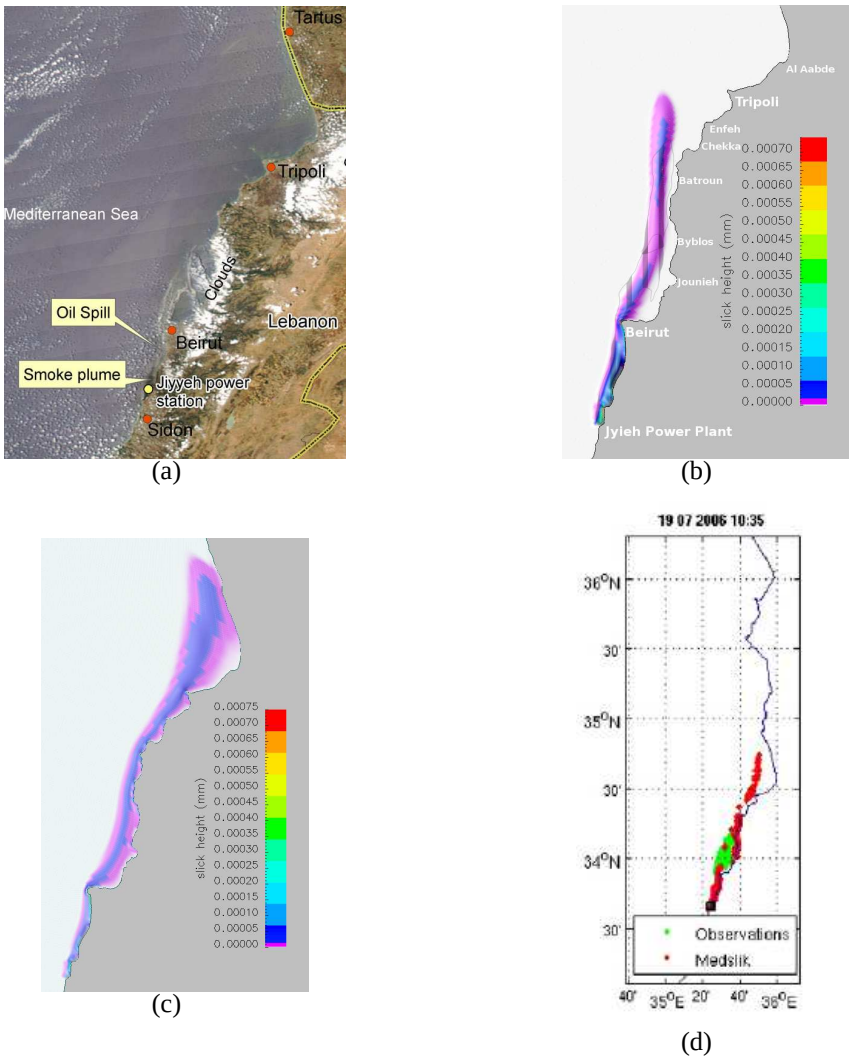

Figure 5.14: Oil slick extent on **July 19**th: as shown by MODIS AQUA satellite in figure 5.14(a). Figure 5.14(b) shows the oil slick front at the height of Enfeh as predicted by SIMOIL coupled to the depth averaged currents model. Grey stripes represent the oil observed by satellite. Figure 5.14(c) shows the oil slick filling up the gulf od Tripoli as predicted by SIMOIL coupled to the potential flow currents model. Figure 5.14(d) shows the oil parcels distribution front in front of the gulf of Tripoli as predicted in real time by MEDSLIK-CYCOFOS model.

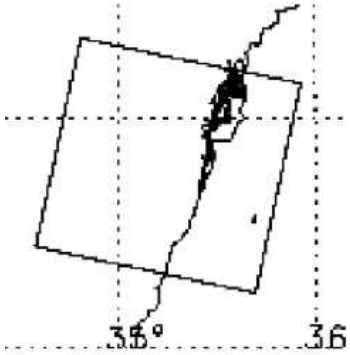

(a)

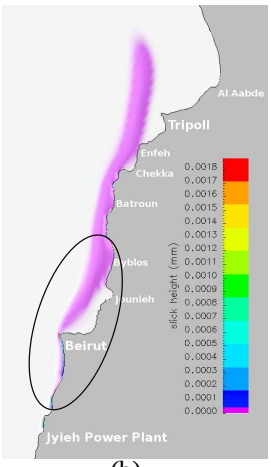

(b)

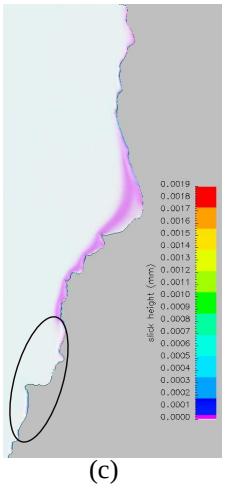

(c)

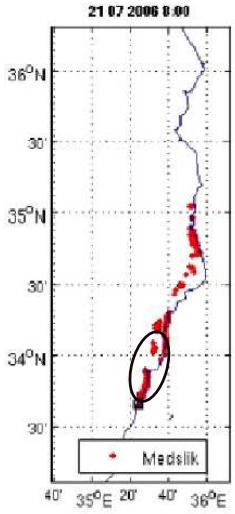

(d)

Figure 5.15: Oil slick extent on **July 21**st: inside the gulf of Beirut as shown by ASAT ENVISAT satellite in figure 5.15(a). Figure 5.15(b) shows similarly the oil slick inside the gulf of Beirut as predicted by SIMOIL coupled to the depth averaged currents model. Figure 5.15(c) shows that the oil slick has left the gulf of Beirut as predicted by SIMOIL coupled to the potential flow currents model. Figure 5.15(d) shows the oil parcels distribution predicted in real time by MEDSLIK-CYCOFOS model.

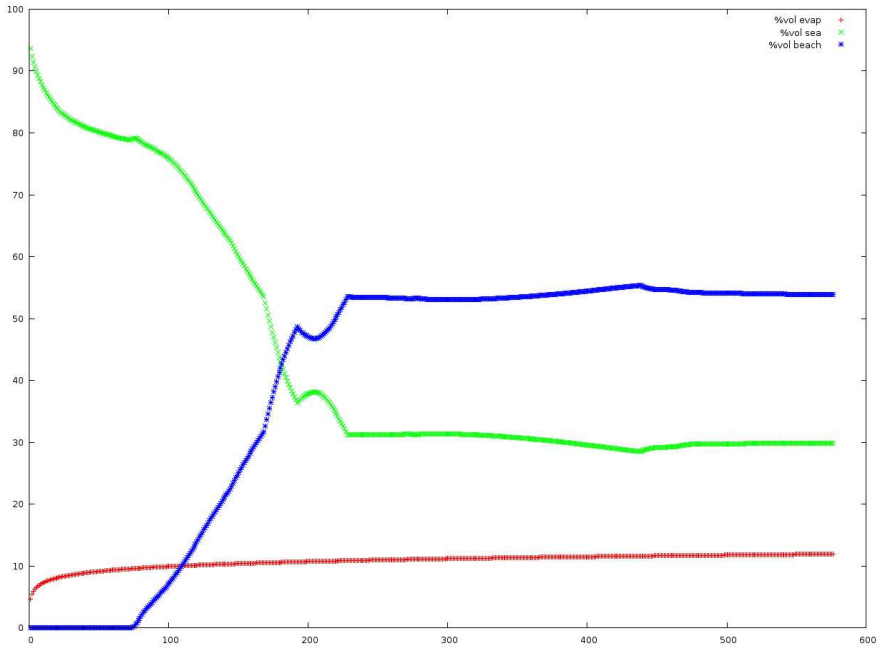

Figure 5.16: Evolution of the percentage of volumes of oil evaporated, at sea and accumulated on the beaches, as simulated by SIMOIL coupled to depth averaged currents model between 13 of July and 06 of August 2006. (Timeline in hours)

SIMOIL coupled to depth averaged currents, reproduces well those features, as can be seen in figure 5.17(b), with the exception of the oil entering the gulf of Tripoli. Even if the extension of the oil slick northward up to Syrian coastal water agrees with the observations. The sea surface covered by oil is best estimated with this model than with any of the other ones.
In the version of SIMOIL coupled to the potential flow model in figure 5.17(c), there is no more oil at sea in the domain as or the oil has landed on most of the Lebanon and Syria coasts, or it has left the domain through the north boundary. After ten days the model overestimates strongly the northward extent of the slick.
MEDSLIK-CYCOFOS results appearing in figure 5.17(d), seems to underestimate the offshore extent of the slick and the quantity of oil remaining at sea. It shows oil landing north up to the Syrian beaches of Tartus, that can not be confirmed by the satellite observations due to the presence of clouds.

Syrian authorities reported a first wave of oil reaching their coast on 26^{th} of July and a second one on 2^{nd} of August. It is not possible to confirm it in MODIS AQUA image of **1^{st} of August** because of the clouds covering Syria, as shown in figure 5.18(a). However, on the Lebanese coast, it can be observed that landed oil is being remobilized by the wind and transported offshore at every headland located between Jiyeh and Tripoli.
The SIMOIL version, with depth averaged currents, in figure 5.18(b), cannot simulate the remobilization of beached oil, but confirms the north and west extension of the oil slick. Not shown in this figure, SIMOIL did forecast the arrival of oil in Tartus between 24 and 25 of July. The image also shows that the oil is broken into two very thin slicks. The smaller one, around 10^{-6} m thin, is transported westward by the winds and currents of the area. The main oil slick is now leaving the coast between Batroun and Tripoli, and pushed northward and westward, offshore the coast of Syria. The slick is very thin now. Its maximum height being around 10^{-5}m makes it difficult to be detected by eye or satellite observation. According to SIMOIL report (see figure 5.16), around 55% of the oil has landed, 30% remains at sea and 12% has evaporated (the error in percentage of volume is due to the evaluation of the surface covered by oil).
The MEDSLIK-CYCOFOS forecast shown in figure 5.18(c) corresponds to 2^{nd} of August. It is not very different than the picture of 10 days before. This is probably due to the fact that, according to MEDSLIK, almost all the oil (80%) landed in the first 200 hours following the bombing, 20% evaporated and then, less than 1% re-

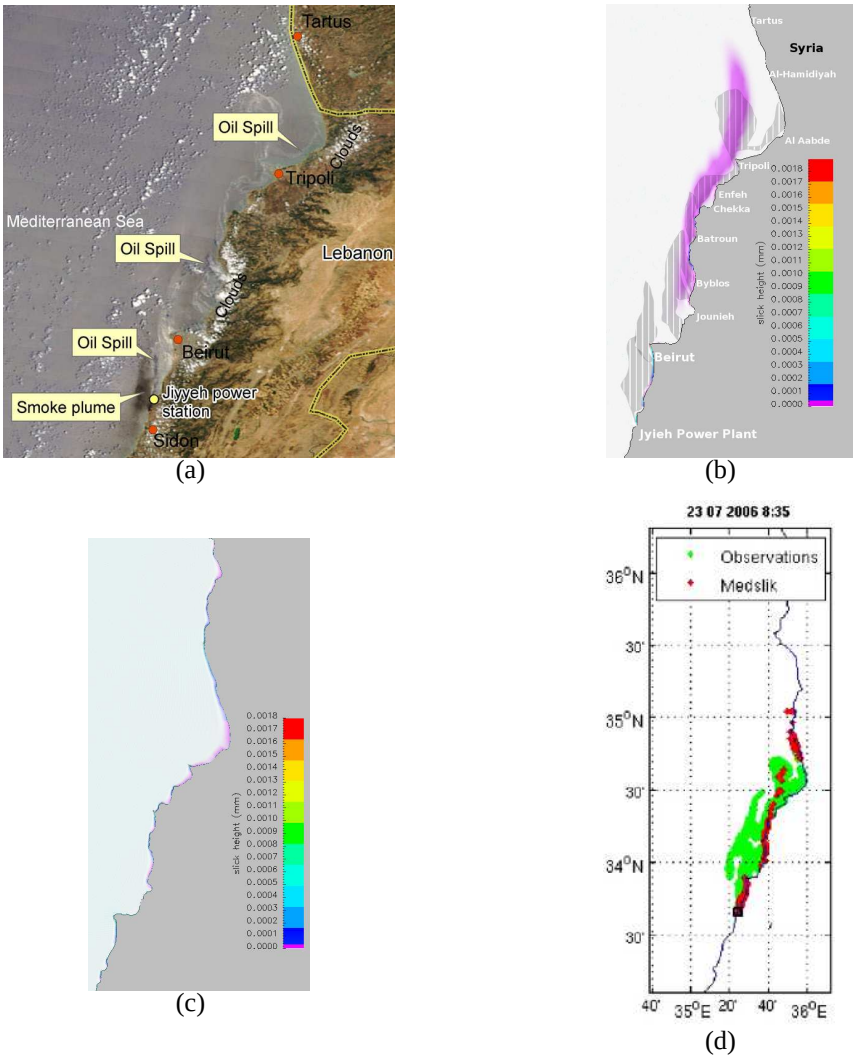

Figure 5.17: Oil slick extent on **July 23**rd: as shown by MODIS AQUA satellite in figure 5.17(a). Figure 5.17(b) shows that the oil slick (in purple) is very close to the coast between Byblos and Tripoli, and in the gulf of Tripoli, as predicted by SIMOIL coupled to the depth averaged currents model. The observed oil is painted in grey stripes. Figure 5.17(c) shows the oil slick has left the domain as predicted by SIMOIL coupled to the potential flow currents model. Figure 5.17(d) shows the oil parcels distribution reaching the Syrian coast as predicted in real time by MEDSLIK-CYCOFOS model.

mained at sea. In agreement with the observations, the oil reached Tartus on 2^{nd} of August, but the extension of the slick offshore is underestimated by this model all along the coast.

It is possible to compare the assessment map published by the Greenline Association [59], drawn after on the ground observations made before 10^{th} of August. This map is shown in figure 5.19(a). The next picture, in figure 5.19(b), shows the computational domain, with in the vertical dimension, the quantity of oil accumulated on the coast until 2^{nd} of August, as predicted by SIMOIL coupled to the depth averaged currents. This result is in very good agreement with the observations reported in figure 5.19(a): the biggest quantity of oil is found on he beach close to Jiyeh and on the south coast of Beirut headland. The next area presenting more oil on the coast would be located between Jounieh and Jbeil and in Batroun. Finally oil has landed also in the bay of Chekka, along the headland of Enfeh and on the shore of Tripoli. As seen before, the portion of coast situated in the gulf of Tripoli from El Abdeh to the Syrian border does not appear oiled in the simulation. This is probably due to the to the low resolution of wind data and to the simplification of the bathymetry in this area (forced by the presence of the Palm Islands).

Some partial conclusions can be drawn from these simulations:

- The potential flow model, coupled to SIMOIL, gives a good approximation of the trajectory of the oil slick for short term forecasts (less than 1 week). This feature is specially interesting in the cases that there is no information about bathymetry. For long term forecasts and/or complex coastlines, where the recirculation currents inside the bays are intense (in comparison to the wind intensity), then this model fails to predict correctly the landing of the oil. The depth averaged currents model developed in this work resolves this issue and constitutes the major improvement added to SIMOIL.
- Coupled to the depth averaged currents model, SIMOIL provides very accurate information about the extension of the slick, both along the coast and offshore, and about the oil deposition on the coast. It has proved to be in very good agreement with the observational data collected during the Lebanon oil spill. Compared to the reference high resolution simulation system MEDSLIK-CYCOFOS, it appears that the Eulerian modelling of the oil slick gives a description of the horizontal dispersion of the oil better than the turbulent diffusion of Lagrangian particles. This is probably due to the

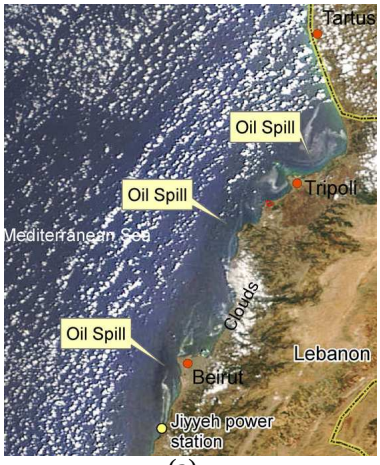

(a)

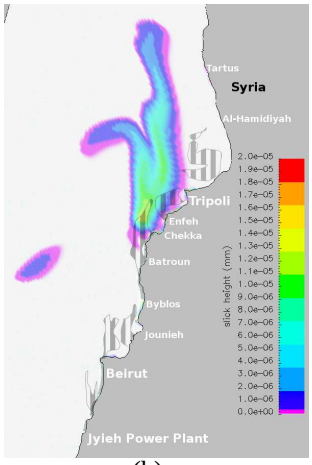

(b)

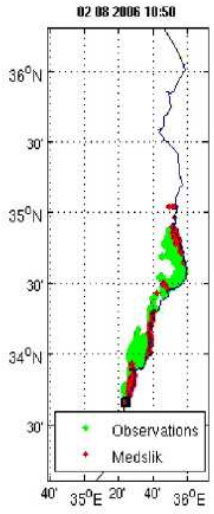

(c)

Figure 5.18: Oil slick extent on **August 1**st: as shown by MODIS AQUA satellite in figure 5.18(a). Figure 5.18(b) shows the oil slick (in colors) as predicted by SIMOIL coupled to the depth averaged currents model compared to the satellite observations in grey stripes. Figure 5.18(c) shows the oil parcels distribution predicted in real time by MEDSLIK-CYCOFOS model.

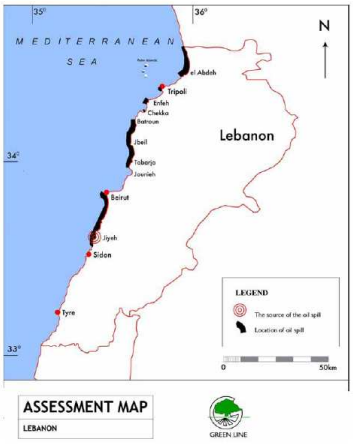

(a)

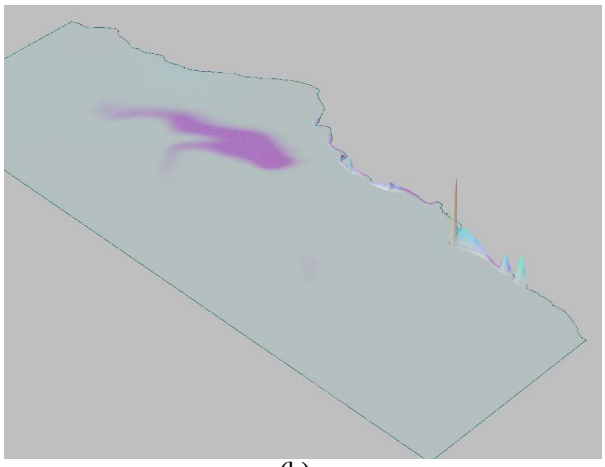

(b)

Figure 5.19: 5.19(a)Greenline Assessment Map 10 of august. 5.19(b) 3-dimensional visualisation of the accumulation of oil on the coastline of Lebanon predicted by SIMOIL. The biggest quantity is found between Jiyeh and Beirut, but significant quantity is also found between Jounieh and Batroun, the bay of Chekka and the headlands of Enfeh and Tripoli

difficulty to estimate proper turbulent diffusion coefficients, but also to that the physic of the oil slick spreading at the sea surface under gravity-viscosity regime is much better represented by the Eulerian slick thickness model of SIMOIL, than by the dispersion of a bunch of oil parcels released randomly at sea.

- The low quality prediction of oil deposition in the bay of Tripoli, suggests that a high spatial and temporal resolution of environmental data is critical close to the coast, specially concerning the bathymetry and the wind vector data. This is necessary to solve correctly the currents flow field and the oil slick movement. This can be achieved nesting a local boundary fitted coordinates model within regional and mesoscale atmospheric and oceanic models. It also has to be noticed that this depth averaged model does not resolve the Ekman transport and so, the coastal upwelling which can be a major component of coastal circulation under certain circumstances.
- The additional information of the thickness of the oil slick given by SIMOIL, could be useful for remote oil spill detection missions (by satellite or plane). It allows also to estimate better the volume of oil at sea and on the shore to take decision about the right response actions to implement.

Chapter 6

Conclusions and Future Work

6.1 Conclusions

In this work, a computational tool for the simulation of accidental oil spills has been developed. Basically this numerical tool is made of two parts. The first part consists of a hydrodynamic model based on shallow water equations that resolves the depth averaged coastal currents. The second part solves the transport and evaporation of the oil slick with greater accuracy than the previous version of SIMOIL. Those models are written in generalised coordinates so are able to run easily in naturally complex coastal topographies.

The model integrates vertically the ocean primitive equations under the rigid-lid approximation. Consequently, a system of equations is obtained describing a shallow and rotating layer of fluid where Coriolis force and seabed friction can be important. The shallow water model with the rigid-lid approximation is formulated in function of the vorticity and stream function variables in order to reduce the number of equations to be solved.

The equations for the depth averaged currents are discretized, spatially and temporally, using finite differences of second order of accuracy. The implemented boundary conditions are suitable for the study of coastal flow. They were specially designed to deal with complex shoreline geometry and possibly complex inflow and outflow at the open boundaries of coastal domains.

The accuracy of the numerical schemes relative to the oil model is upgraded from second order to fourth order in time, and from first order to second order in space. Boundary conditions for accumulation are used on the coast and convective

conditions are set up at the outlet. One of the major improvement concerns the evaporation model. In recent studies [14, 12, 64], Fingas demonstrated that the model of Mackay, based on the hypothesis of boundary layer regulated evaporation of the oil, although it is used by most of the current oil models, is not totally adequate to oil-at-sea evaporation process. Equations derived from widely available measurements of crude oil distillation properties are now employed, enabling simpler and appropriate calculations of the evaporation rate for all kind of oils.

During the development of the computer code, several modules were added to the code to enhance his performance and versatility:

- To face the requirements of high resolution calculations, parallelisation techniques are used that allow to run the numerical simulations either on shared memory computers or on classical sequential architecture. The parallelisation was implemented using Open MP commands embedded into the code.

- Sparse environmental data can be assimilated easily thanks to a bi-variate interpolation routine integrated into the code.

- The study of the dispersion of objects different than oil slick is made possible thanks to a particle tracking technique initially made for passive tracers diffusion studies but easily adaptable to other cases.

Initially, the model and the code for hydrodynamics were verified against many test-cases well documented in the literature, paying special attention to mesh deformation and open boundary conditions. Then, the code was successfully tested and validated in oceanic conditions against experimental and numerical data.

Finally, the complete system of prediction, coupling the depth averaged currents forecasts and the oil transport model, has been successfully run for two cases of oil spill accidents. The first study can be used to plan response actions in the port of Tarragona in case of a massive oil leakage at the Repsol floating dock. The simulation is compared to the previous version of SIMOIL which advection currents where based on a potential flow approximation. The results show the importance of the evaporation process and that the proper resolution of coastal currents is critical for an accurate prediction of the oil slick movement close to the shoreline. In the second case study, the code predictions are compared to other numerical simulations and observations collected during a real oil spill accident: the 2006 Lebanon

oil spill. Not only the quality of the prediction was validated by observations, but the results shown an expected improvement in accuracy over the precedent version of SIMOIL based on potential flow advection of the oil slick. Additionally, the results shown to be in very good agreement with the Mediterranean operational ocean network simulations of reference.
This original engineering work, by integrating multidisciplinary techniques, shown its validity and reached its objective to simulate numerically oil spills fate and trajectory. It is a fundamental improvement of SIMOIL and can be considered a suitable and valuable assessment tool for contingency planning of oil spill in coastal areas.

6.2 Future work

This work was carried out to improve the time and space evolution of oil spills. It would be useful to go further and extend the range of application of the code for example to study the fate of the oil droplets dispersed in the water column, or to determine the drift of any object lost at sea such as persons, containers or ships.

The numerical model presented here is a good tool in that direction. Some important tracks are given here for further possible improvements:

- First, automatize the generation of the boundary-fitted mesh. Currently, it is the step of the simulation that is more time consuming as data from different sources and formats have to be combined (node locations, bathymetry, bottom friction coefficient, Coriolis coefficient) and sometimes, for complex regions, assembled one node at a time.
- Second, add a data-assimilation system capable of collecting in real time in-situ data, and integrating numerical data from coarser regional and meso-scale oceanic and atmospheric models. The more information in the system, the more accurate will be the simulation. It should allow to update the forecasts continuously, adapting the simulation to any change occurring in the field during the calculations.
- Third, adapt the code to distributed memory computers, typically to large computer clusters. The Open MP parallel programming already implemented has advantages in terms of simplicity of programming but lacks the flexibility and scalability of message passing interface (MPI) framework. More computational resources will be needed to assimilate more environmental data

and actualise the predictions, so the introduction of MPI programming could tackle these issues.

- Fourth, develop a three dimensional oceanic flow model to resolve the heat and mass transfer in the vertical direction. It could be associated to a three dimensional model for the transport of oil parcels. This would allow to study the oil dispersion in areas such as iced sea, upwelling zones, river estuaries or deep seas (like in the case of the Prestige oil spill). Planning response actions to sub-sea extraction well blowouts, such as the Deepwater Horizon oil spill, is necessary and need to be developed more [7, 65, 66]. Numerical simulation is a safe and inexpensive way to prepare properly for such situations.

Improving the code by implementing gradually such modules would allow to broaden its capacity and adaptability, to integrate the prediction system within operational forecast networks and to get prepared for future challenges in the prediction of the transport of pollution.

Bibliography

[1] Committee on Oil in the Sea National Research Council. *Oil in the Sea III : Inputs, Fates, and Effects*. National Academy Press, 2003.

[2] Oceana commitee on oil pollution. The dumping of hydrocarbons from ships into the seas and oceans of europe the other side of oil slicks. Technical report, OCEANA, 2003.

[3] ITOPF. Handbook 2010/11. Technical report, The Iternational Tanker Owners Pollution Federation Limited, 2010.

[4] G. Novelli, A. Fabregat, I. Cuesta, and F.X. Grau. Solving shallow water equations in generalized domains, a tool for predicting the drift of oil spils in coastal zone. In *Symposiun on marine accidental oil spills VERTIMAR-2007*, 2007.

[5] P.J. Brandvik, D. Rasmussen, K. Gustavson, F. Stuer-Lauridsen, and H. Skov. State of the art report : Real time oil spill modelling of marine oil spills. Technical report, Spill Response Experience, 2006.

[6] Malcom L. Spaulding. A state-of-the-art review of oil spill trajectory and fate modeling. *Oil & Chemical Pollution*, 4:39–55, 1988.

[7] M. Reed, O. Johansen, P.J. Brandvik, P. Daling, A. Lewis, R. Fiocco, D. Mackay, and R. Prentki. Oil spill modeling towards the close of 20th century : Overview of the state of the art. *Spill Science & Technology Bulletin*, 5(1):3–16, 1999.

[8] I.D. James. Modelling pollution dispersion, the ecosystem and water quality in coastal waters : a review. *Environmental Modelling & Software*, 17:363–385, 2002.

[9] J.P Benqué, A. Haugel, and P. Viollet. *Engineering application of Computational Hydraulics*. Pitman Advanced Publishing Program, 1982.

[10] Pavel Tkalich. A cfd solution of oil spill problems. *Environmental Modelling & Software*, 21(21):271–282, 2004.

[11] I. Cuesta, F.X. Grau, and F. Giralt. Numerical simulation of oil spills in a generalized domain. *Oil & Chemical Pollution*, 7:143–159, 1990.

[12] M. Fingas. *The Basics of Oil Spill Cleanup*. CRC Press, 2000.

[13] P. Jokuty, S. Whiticar, Z. Wang, M. Fingas, B. Fieldhouse, P. Lambert, and J. Mullin. Properties of crude oils and oil products, internet version october 2000, accessed via http://www.etcentre.org/spills. Technical report, Environment Canada, 2000.

[14] M. Fingas. A literature review of the physics and predictive modelling of oil spill evaporation. *Journal of Hazardous Materials*, 42:157–175, 1995.

[15] H. Xie, P.D. Yapa, and K. Nakata. Modeling emulsification after an oil spill in the sea. *Journal of Marine Systems*, 68:489–506, 2007.

[16] P. Tkalich and E.S. Chan. Vertical mixing of oil droplets by breaking waves. *Marine Pollution Bulletin*, 44:1219–1229, 2002.

[17] B. Ornitz and M. Champ. *Oil Spills First Principles: Prevention and Best Response*. Elsevier Science, 2002.

[18] F.X. Merlin. Traitement aux dispersants des nappes de pétrole en mer traitement par voie aérienne et par bateau guide opérationnel. Technical report, CEDRE, 2005.

[19] X. Liu and K. W. Wirtz. The economy of oil spills: Direct and indirect costs as a function of spill size. *Journal of Hazardous Materials*, 171:471–477, 2009.

[20] P.D. Bates, S.N. Lane, and Robert I. Ferguson. *Computational Fluid Dynamics Applications in Environmental Hydraulics*. John Wiley & Sons, Ltd, 2005.

[21] Robert H. Stewart. *Introduction to Physical Oceanography*. Internet edition of september 2004, 2004.

[22] S.A. Thorpe. *An Introduction to Ocean Turbulence*. Cambridge University Press, 2007.

[23] L.H. Kantha and C.A. Clayson. *Numerical Models of Oceans and Oceanic Processes*, volume 66 of *International geophysics series*. Academic Press, 2000.

[24] G. K. Vallis. *Atmospheric and Oceanic Fluid Dynamics*. Cambridge University Press, 2006.

[25] G. J. F. van Heijst and H. J. H. Clercx. Laboratory modeling of geophysical vortices. *Annual Review of Fluid Mechanics*, 41:143–164, 2009.

[26] Joseph Pedlosky. *Geophysical Fluid Dynamics*. Springer, second edition edition, 1992.

[27] K. Bryan. A numerical method for the study of the circulation of the world ocean. *Journal of Computational Physics*, 4:347–376, 1969.

[28] Joel H. Ferziger and Milovan Perić. *Computational methods for fluid dynamics*. Springer, third, rev. edition edition, 2002.

[29] H Burchard, P.D Craig, J.R. Gemmrich, H. van Haren, P.P. Mathieu, H.E. Markus Meier, W.A.M Nimmo Smith, H. Prandke, T.P. RIppeth, E.R. Skyllingstad, W.D. Smyth, D.J.S. Welsh, and H.W. Wijesekera. Observational and numerical modeling methods for quantifying coastal ocean turbulence and mixing. *Progress in Oceanography*, 76:399–442, 2008.

[30] D.A. Greenberg, F. Dupont, F.H. Lyard, D.R Lynch, and F.E. Werner. Resolution issues in numerical models of oceanic and coastal circulation. *Continental Shelf Research*, 27:1317–1343, 2007.

[31] E. Blayo and L. Debreu. Revisiting open boundary conditions from the point of view of characteristic variables. *Ocean Modelling*, 9:231–252, 2005.

[32] F.X. Grau and F. Giralt. A comparative study of formulations for bidimensional generalized transport equations. *Anales de Quimica*, 85:128–134, 1987.

[33] F.X. Grau and F. Giralt. Computing the flow and transfer processes around submerged bodies using orthogonal grids. *Anales de Quimica*, 91:502–511, 1995.

[34] P.R. Kanna and M. K. Das. A short note on the entrainment and exit boundary conditions. *International Journal for Numerical Methods in Fluids*, 50:973–985, 2006.

[35] F.X. Grau. *Fenòmens de Transport en Fluxos Complexos Evolutius: Simulació Numèrica d'Esteles de Cilines*. PhD thesis, University of Barcelona, 1986.

[36] Hung Le. *Direct numerical simulation of turbulent flow over a backward-facing step*. PhD thesis, Department of Mechanical Engineering of Stanford University, 1995.

[37] S. Piñol and F.X. Grau. Influence of he no-slip boundary condition on the prediction of drag, lift, and heat transfer coefficients in the flow past a 2-d cylinder. *Numerical Heat Transfer, part A*, 34:313–330, 1998.

[38] I. Cuesta. Simulacio numerica d'un vessament de cru en medi maritim. Master's thesis, Universitat de Barcelona, 1988.

[39] Rutherford Aris. *Vectors, tensors, and the basic equations of fluid mechanics*. Dover, 1989.

[40] J.F. Thompson, Z.U.A. Warsi, and C.W. Mastin. *Numerical grid generation Foundations and applications*. 1985.

[41] H. Akima. Algorithm 526: A method of bivariate interpolation and smooth surface fitting for values given at irregularly distributed points. *ACM Transactions on Mathematical Software*, 4(2):160–164, june 1978.

[42] H. Akima. On estimating partial derivatives for bivariate interpolation of scattered data. *Rocky Mountains Journal of Mathematics*, 14(1):41–51, 1984.

[43] B. Lin and S.N. Chandler-Wide. A depth-integrated 2d coastal and estuarine model with conformal boundary-fitted mesh generation. *International Journal for Numerical Methods in Fluids*, 23:819–846, 1996.

[44] C. Hirsch. *Numerical computation of internal & external flows*, volume 1: fundamentals of numerical discretization. Wiley-Interscience, 1992.

[45] J.D. Hoffman. *Numerical methods for engineers and scientists*. McGraw-Hill, 2001.

[46] Erkan Erturk and Bahtiyar Dursun. Numerical solutions of 2-d steady incompressible flow in a driven skewed cavity. *ZAMM-Journal of Applied Mathematics and Mechanics*, 87(5):377–392, 2007.

[47] U. Ghia, K.N. Ghia, and C.T. Shin. High-re solutions for incompressible flow using the navier-stokes equations and multigrid method. *Journal of Computational Physics*, 48:387–411, 1982.

[48] L. Fuchs and N. Tillmark. Numerical and experimental study of driven flow in a polar cavity. *International journal for numerical methods in fluids*, 5:311–329, 1985.

[49] P. R. Kanna and M. K. Das. A short note on the reattachment length for bfs problem. *International Journal for Numerical Methods in Fluids*, 50:683–692, 2006.

[50] A.G.L. Borthwick and E.T. Kaar. Shallow flow modelling using curvilinear depth-averaged stream function and vorticity transport equations. *International Journal for Numerical Methods in Fluids*, 17:417–445, 1993.

[51] B.F. Armaly, F. Durst, J.C.F. Pereira, and B. Schonung. Experimental and theoretical investigation of backward-facing step flow. *Journal of Fluid Mechanics*, 127:473–496, 1983.

[52] I.E. Barton. The entrance effect of laminar flow over a backward-facing step geometry. *International Journal for Numerical Methods in Fluids*, 25:633–644, 1997.

[53] D.K. Gartling. A test problem for outflow boundary conditions–flow over a backward-facing step. *International Journal for Numerical Methods in Fluids*, 11:953–967, 1990.

[54] D.L. Quintana, M. Amitay, A. Ortega, and I.J. Wygnanski. Heat transfer in the forced laminar wall jet. *Journal of Heat Transfer*, 119:451–459, 1997.

[55] L. Zavala Sansón and G. J. F. van Heijst. Interaction of barotropic vortices with coastal topography : Laboratory experiments and numerical simulations. *Journal of Physical Oceanography*, 30:2141–2162, 2000.

[56] J. Font, A. Julia, J. Rovira, J. Salat, and J. Sanchez-Pardo. Circulacion marina en la plataforma continental del ebro determinada a partir de la distribucion de masas de agua y los microcontaminantes organicos en el sedimento. *Acta Geologica Hispanica*, 21–22:483–489, 1986–1987.

[57] Tarragona Port Authority. 2010 annual report. Technical report, Port de Tarragona, 2010.

[58] UNEP Lebanon Assessment Team. Lebanon post-conflict environmental assessment. Technical report, UNEP, 2007.

[59] Green Line Association. Lebanon oil spill july 2006- july 2007. Technical report, Green Line Association, 2007.

[60] G. Coppini, M. De Dominicis, G. Zodiatis, R. Lardner, N. Pinardi, R. Santoleri, S. Colella, F. Bignami, D.R. Hayes, D. Soloviev, G. Georgiou, and G. Kallos. Hindcast of oil-spill pollution during the lebanon crisis in the eastern mediterranean, july–august 2006. *Marine Pollution Bulletin*, 62:140–153, 2011.

[61] R.J. Irwin, M. VanMouwerik, L. Stevens, M.D. Seese, and W. Basham. Environmental contaminants encyclopedia, 1997.

[62] National Imagery and Mapping Agency. Nima technical report tr8350.2, department of defense world geodetic system 1984, its definition and relationships with local geodetic systems. Technical report, National Imagery and Mapping Agency, 2004.

[63] W. H. F. Smith and D.T. Sandwell. Global seafloor topography from satellite altimetry and ship depth soundings. *Science*, 277:1957–1962, Sept. 1997.

[64] Merv P. Fingas. Modeling evaporation using models that are not boundary-layer regulated. *Journal of Hazardous Materials*, 107:27–36, 2004.

[65] Arne Jernelov. How to defend against future oil spills. *Nature*, 466:182–183, 2010.

[66] Richard Camilli, Christopher M. Reddy, Dana R. Yoerger, Benjamin A. S. Van Mooy, Michael V. Jakuba, James C. Kinsey, Cameron P. McIntyre, Sean P.

Sylva, and James V. Maloney. Tracking hydrocarbon plume transport and biodegradation at deepwater horizon. *Science*, 330:201–204, 2010.